High-Temperature Oxidation, Fluoride-Ion Cleaning, and Activated Diffusion Brazing of Nickel-Based Superalloy GTD111

by

Jesse Brenneman

A thesis

presented to the University of Waterloo

in fulfillment of the

thesis requirement for the degree of

Master of Applied Science

in

Mechanical Engineering

Waterloo, Ontario, Canada, 2011

Author's Declaration

I hereby declare that I am the sole author of this thesis. This is a true copy of the thesis, including any required final revisions, as accepted by my examiners.

I understand that my thesis may be made electronically available to the public.

Abstract

The need for industrial gas turbines to operate at higher temperatures and/or speeds has resulted in the continual modification of nickel-based superalloys to provide better high-temperature strength and corrosion resistance for components such as hot-section turbine blades. Thermal-Mechanical Fatigue (TMF) cracking, accelerated by the oxidation that forms as a result of the exposure of bare metal during the crack-opening stages, is one of the most common forms of damage experienced by service-run turbine blades.

Due to the high costs associated with manufacturing nickel-based superalloy components, damaged turbine blades must be repaired to restore their original mechanical properties. One such method, Activated Diffusion Brazing (ADB), is under development for this purpose, and involves melting a two-part powder mixture into a damaged region. However, the tenacious oxides formed on nickel-based superalloy components provide an obstacle for the repair process, and must be removed. Fluoride-Ion Cleaning (FIC) uses flowing hydrogen and HF gas to remove tenacious oxide scales through a set of chemical reactions, leaving cleaned components free of oxide compounds and depleted of the strong oxide-formers of Al and Ti.

GTD111 is a nickel-based superalloy containing the strong oxidizing elements of Al, Ti, and Cr, and is similar in composition to other nickel-based superalloys such as DD8 and Rene95. Literature concerning the oxidation, cleaning, and brazing of this particular alloy is limited, and as such this thesis serves as a comprehensive overview of the chemical effects of each above process on GTD111.

The objectives of this project are to determine, through SEM-EDX and element mapping analysis, the oxidation behavior of nickel-based superalloy GTD111, the effects of oxidation and FIC on the chemistry near the surface of this particular alloy, and the effects of mixing ratio and paste viscosity on the quality of repairs made by ADB.

Notches of 8 mm depth and 0.25 mm width were made in coupons of GTD111 via wire-EDM and samples were oxidized between 1 and 452 hours at 900°C. Samples oxidized between 96 and 452 hours were sectioned in half and one half of each sample was cleaned via the standard FIC process at Ti-Coating Inc. Notches of 8 mm depth and 1 mm width, also made via wire-EDM, were repaired by the ADB process with a bonding temperature of 1220°C and a holding time of 65 minutes.

Time-dependent multi-layer oxide growth was observed on all samples, consisting of an innermost discontinuous aluminum oxide region, followed by a thin continuous band of Ni-W-Ta oxide and a thicker, very dense chromium oxide layer. Some oxidation times exhibited the presence of weak, inconsistent oxide regions rich in Ni and/or Ti. Since the GTD111 alloy does not contain sufficient amount of Al to form a continuous layer – as 5-7% Al is required – oxidation resistance was provided mainly by the formation of the dense chromium oxide layer. A region heavily depleted of Al and Ti and therefore the strengthening gamma prime phase was observed below and surrounding the Al-rich oxide regions.

Chemical analysis of cleaned samples showed that the standard FIC process at Ti-Coating Inc. was able to remove all oxide compounds formed during oxidation at 900°C, and that the prior oxidation time had no effect on the chemistry within the surface of the cleaned samples; however, the depths of elemental and gamma prime phase depletion were affected. The elemental depletions of Al and Ti have been observed in past studies, but depletions of Ni and concentrations of Cr near the surfaces of cleaned components have not been previously observed.

Preliminary brazing trials made with varying paste viscosities demonstrated the importance of paste pre-placement and maintaining the molten filler metal within the notch, as better pre-placement resulted in higher densities in the braze-repaired region of the brazing trial samples. Although porosity was observed on all samples, the paste pre-placement was found to be more important in reducing porosity than the mixing ratio and paste viscosity, although using an appropriate paste viscosity allowed for better pre-placement.

Acknowledgements

To my wife, Brooke, who has seen me through the process of formulating this thesis, and all of the struggles that have come along with it

Table of Contents

List of Figures

List of Tables

Chapter 1 Introduction

1.1 Background

In order for the power generation industry to keep up with the trend of increasing efficiency, today's industrial gas turbines are continually being modified to run at greater temperatures and/or higher speeds [1]. As a result, the materials used for critical components such as first-stage hot-section turbine blades must undergo constant development to improve their high-temperature properties in this harsh environment of combustion and cyclic loading.

Nickel-based superalloys have found their niche in the power generation industry, as their blend of high-temperature strength and creep-resistance, coupled with a strong resistance to corrosion and oxidation, make them ideal for use as hot-section turbine blades. High-temperature strength comes from additions of Al, Ti, and Ta to form gamma prime precipitates in a gamma matrix, and additions of Mo, W, and Ta provide solid-solution strengthening [2]. Alloying elements such as Mo, Cr, and Co are added to prevent local hot corrosion [3], and high-temperature oxidation resistance is achieved by additions of Al and Cr, which preferentially oxidize to form dense, protective oxide films, which slow the overall oxidation process [4]. Such an excellent blend of properties does not come without its shortcomings, which include extremely expensive raw materials, casting methods, and machining processes [5].

The high cost of turbine blades and other components made from nickel-based superalloys becomes especially relevant when a component fails prematurely or is noticed upon inspection to be damaged enough to require removal from service. Damage generally seen on turbine blades includes Thermal-Mechanical Fatigue (TMF) cracks due to high-temperature cyclic loading, local hot-corrosion and surface erosion from harmful combustion products, and damage such as chips in the surface or on the edges of a component from foreign objects [5,6,7].

High-temperature oxidation, in all cases, results from the damaged area exposing bare metal to the oxygen-containing atmosphere, and in the case of TMF cracking, oxidation increases the rate at which cracks propagate through a component [8]. During the crack-opening segment of each loading cycle, fresh metal is exposed to the oxygen-containing atmosphere as the crack moves deeper into the substrate. This continual oxidation of the moving crack tip accelerates the crack's propagation through the component, resulting in a shorter service life. Oxidation is therefore a main cause, or at least a strong contributor, to the failure of hot-section turbine blades [9,10,11].

As a result of the high replacement cost of hot-section turbine blades, a repair process is required in which damaged blades can be returned to normal functionality, by restoring the damaged area to near-base metal microstructure and mechanical properties. The damage observed on service-run components can vary greatly in terms of where the damage is located – which may be easy or difficult to access – and the geometry of the damaged region. For example a micro-crack due to TMF at the root of the blade can be very deep and narrow, whereas an eroded region near the blade tip may be very wide and shallow. As a result of this large variation in geometry and location, a suitable repair process should be flexible in terms of the adaptability of its process parameters to repair different-sized defects in potentially difficult-to-access locations of a turbine blade.

Fusion welding and conventional brazing processes have been found unsatisfactory, as the high heating and cooling rates experienced during fusion welding and the harmful intermetallics inherent in the conventional brazing process cause Heat-Affected Zone (HAZ) cracking and decreased toughness due to stress concentrations, respectively [5,12]. In hopes of eliminating such problems, a low-temperature, diffusion-based repair process referred to as Activated Diffusion Brazing (ADB) is currently under development.

Repairs by the ADB process can result in nearly invisible joints with mechanical properties reaching those of the base metal. However, a major limitation to the diffusion brazing process is that it cannot be performed atop a pre-existing oxide, so the complex oxide scales formed on nickel-based superalloys must be removed from components prior to attempting a repair. Fluoride-ion cleaning is one of the available means of oxide removal, as it is capable of removing complex oxide scales from many materials, including nickel-based superalloys.

The proprietary General Electric nickel-based superalloy GTD111 is an alloy that contains Al, Ti, and Cr as major alloying elements, whereas many other superalloys contain only Al and Cr. The addition of Ti results in more complex oxide structures than have been observed on other alloys. The GTD111 superalloy has not been widely studied in the areas of oxidation, fluoride-ion cleaning, and activated diffusion brazing, making it an excellent candidate for further research.

1.2 Objectives

Each chapter of this thesis has its own specific objectives, but the central theme is the analysis of the effects of the processes of oxidation, Fluoride-Ion Cleaning, and Activated Diffusion Brazing on the chemistry of the affected regions of GTD111 coupons. *Therefore, the primary objective of this thesis work was to determine the oxidation behaviour of GTD111 after various oxidation times through SEM-EDX and element mapping analysis of coupon cross-sections, as well as XRD analysis of the oxidized surfaces*. The potential time-dependent oxidation behaviour of GTD111 has not been investigated in past studies.

A secondary objective, which has not previously been documented, *was to determine the effects of oxidation time on the chemistry near the surface of samples processed via FIC*. Finally, the objective of the brazing trials was to evaluate how factors such as mixing ratio and paste viscosity affect the density, and how the prior chemistry of cleaned samples affects the final chemistry of repairs made by ADB.

1.3 Thesis Outline

This introductory chapter is followed by a literature review and an explanation of the experimental methods employed in the study. The remainder of this thesis is separated into three main chapters explaining the experimental results of the high-temperature oxidation, fluoride-ion cleaning, and activated diffusion brazing of GTD111. Chapter 4 will present the results of oxidation time on the chemistry and structure of the oxide scales formed on GTD111. In Chapter 5 the effects of prior oxidation time on the effectiveness and resulting chemistry of the fluoride-ion cleaning process will be analyzed. Chapter 6 will show the results of three preliminary brazing trials, and how the chemistry of a braze-repaired sample depends on the resultant chemistry of after the fluoride-ion cleaning process. The major conclusions will be summarized and future work will be presented in Chapter 7.

Chapter 2 Literature Review

2.1 Principles of Oxidation Resistance

High-temperature oxidation is a key concern for superalloy development, as oxide films formed inside growing TMF cracks increase the rate of crack propagation and ultimately decrease the service lives of damaged components [9,10,11]. To counteract the harmful effects of oxidation, nickel-based superalloys are continually being modified to achieve better oxidation resistance, which generally comes in the form of dense, adherent oxide films such as chromia and/or alumina [3,4,10,11]. Such oxide films, formed by the fast-acting selective oxidation of Al and Cr [10,11] appear as continuous layers through which the diffusion of oxygen and base metal ions is slowed dramatically [10]. Since the diffusion of oxygen and base metal ions is the driving force for oxidation, the presence of protective oxide films such as chromia and alumina reduce the rate of oxidation experienced by superalloy components. The oxidation resistance of superalloy components can be increased by adding strong oxide formers such as Cr, Al, and Ti or adding active elements such as Y, Ha, Ta to an alloy [13].

2.1.1 Adding Strong Oxide Formers

Strong oxide formers such as Cr, Al, and Ti have a high affinity for Oxygen, and as such, are preferentially oxidized when added to a base metal such as Ni since they are more thermodynamically stable in the presence of oxygen. The Ellingham diagram in Figure 2.1 shows the thermodynamic stability of different elements when associated with oxygen. Elements nearer the bottom of the figure have a higher affinity for oxygen and will be preferentially oxidized. When a superalloy component is exposed to an oxygen-containing atmosphere, oxygen atoms will react with the Al, Cr, and Ti atoms in the material more readily than with Ni. Also, due to the lower free energy of formation of elements such as Ti, Al, and Cr, the presence of these elements will cause the reduction of NiO. This selective oxidation becomes increasingly important at higher temperatures, because the driving force for oxidation is much stronger and therefore occurs much more rapidly [13].

2.1.2 Adding Active Elements

Even small additions of active elements such as Y, Ha, and Ta can substantially improve the adherence of protective oxide films to the base metal, since the use of such elements allows for smaller amounts of strong oxide formers such as Cr and Al to be used [14]. Active elements present at the alloy surface serve as nucleation sites for oxide compounds [15]. Increasing the number of nucleation sites decreases the spacing between adjacent newly-formed oxide particles, and speeds lateral oxide growth, leading to a more quickly-forming protective oxide film.

10^{-8} 10^{-7} 10^{-6} 10^{-5} 10^{-4}

CO/CO$_2$ RATIO 10^{-14} 10^{-12} 10^{-10} 10^{-8} 10^{-7} 10^{-6} 10^{-5} 10^{-4} 10^{-3} 10^{-3}

O

$6FeO + O_2 = 2FeO_3O_4$

$4Cu + O_2 = 2Cu_2O$

$2Ni + O_2 = 2NiO$

$4Fe_3O_4 + O_2 = 6Fe_2O_3$

$2Co + O_2 = 2CoO$

$2CO + O_2 = 2CO_2$

$2H_2 + O_2 = 2H_2O$

$2Fe + O_2 = 2FeO$

$C + O_2 = CO_2$

$2C + O_2 = 2CO$

H

C

$\Delta G° = RT \ln p_{O_2}$ (kilojoules)

$\frac{4}{3}Cr + O_2 = \frac{2}{3}Cr_2O_3$

$2Mn + O_2 = 2MnO$

$Si + O_2 = SiO_2$

$Ti + O_2 = TiO_2$

$\frac{4}{3}Al + O_2 = \frac{2}{3}Al_2O_3$

M melting point
B boiling point
M melting point of oxide

$2Mg + O_2 = 2MgO$

$2Ca + O_2 = 2CaO$

TEMPERATURE (°C)

p_{O_2} (atm)

CO/CO$_2$ RATIO 10^{-100} 10^{-80} 10^{-60} 10^{-50} 10^{-42} 10^{-38} 10^{-34}

H$_2$/H$_2$O RATIO 10^{14}

Figure 2.1: Ellingham diagram showing the relative free-energy of formation of different elements with oxygen [13].

5

2.1.3 Oxidation Resistance in Ni-Based Superalloys

Liu *et al.* [2] performed oxidation on a single-crystal DD32 nickel-based superalloy for 100 and 500 hours at temperatures of 900 and 1000°C. Mass gain measurements taken over the range of oxidation times showed that the first 100 hours resulted in very fast oxide growth, attributed to the formation of an external NiO scale. Beyond 100 hours, the alloy experienced very slow oxide growth, due to the formation and presence of a continuous, protective layer of Al_2O_3 between the base metal and the external oxide scales. Oxidation resistance in this alloy was, therefore, achieved by the prevention of Ni ion diffusion through the continuous alumina layer.

Sato *et al.* [10] oxidized prototype single-crystal nickel-based superalloys of varying silicon content at 900°C for 100 hours. The study indicated that Al_2O_3 is generally an internally-forming oxide, and that Al additions of 5-7% are required for the formation of a continuous, protective alumina scale. Also, additions of W, Ta, Ti, and Mo were all found to be detrimental to the formation of a continuous alumina scale, and that reductions of such elements should be made if a continuous alumina scale is desired.

Liu *et al.* [16] oxidized the DD8 nickel-based superalloy in single-crystal, poly-crystalline, and nano-crystalline forms for 50 hours at 1000 °C in an environment containing oxygen and water vapour. An important observation made from this study was that materials that did not form a continuous layer of alumina resulted in faster rates of mass gain and, therefore, decreased resistance to oxidation, even though continuous chromia layers were formed. This was an indication of the importance of the continuous alumina layer for optimal oxidation resistance.

The Pilling-Bedworth (P.B) ratio is the ratio of the volume of oxide to the volume of the parent metal of that oxide [13], and can be roughly used to determine the protectiveness of an oxide scale. Since oxide scales are more protective in compression than in tension, oxides that form at the metal/oxide interface and that have a P.B. ratio of greater than 1.0 will experience a slightly compressive stress and will be considered protective. Table 2.1 summarizes the P.B. ratio for the main oxidizing elements in GTD111 and whether or not they are considered protective by this method. It should be noted that nickel oxides are found to be protective in nature due to their P.B. ratio. However, the P.B. ratio is not as accurate for oxides that form at the oxide/gas interface as nickel oxides do. Therefore, the protectiveness of a nickel oxide scale depends on more than just the P.B. ratio, such as the difference in coefficient of thermal expansion (CTE) between different oxide scales [13].

Table 2.1: Pilling-Bedworth ratios of the major elements present in GTD111.

Metal	P.B. Ratio	Protective?
Ni	1.7	YES
Al	1.3	YES
Ti	1.8	NO
Cr	2.0	YES

2.2 Oxidation Mechanisms on a Metal Surface

Figure 2.2 shows a schematic of the formation of oxidation on a metallic surface. When a metal such as Nickel is placed in an oxygen-containing environment at high temperature, the adsorption of oxygen anions by metal cations results in the formation of a metal oxide compound at the surface of the component.
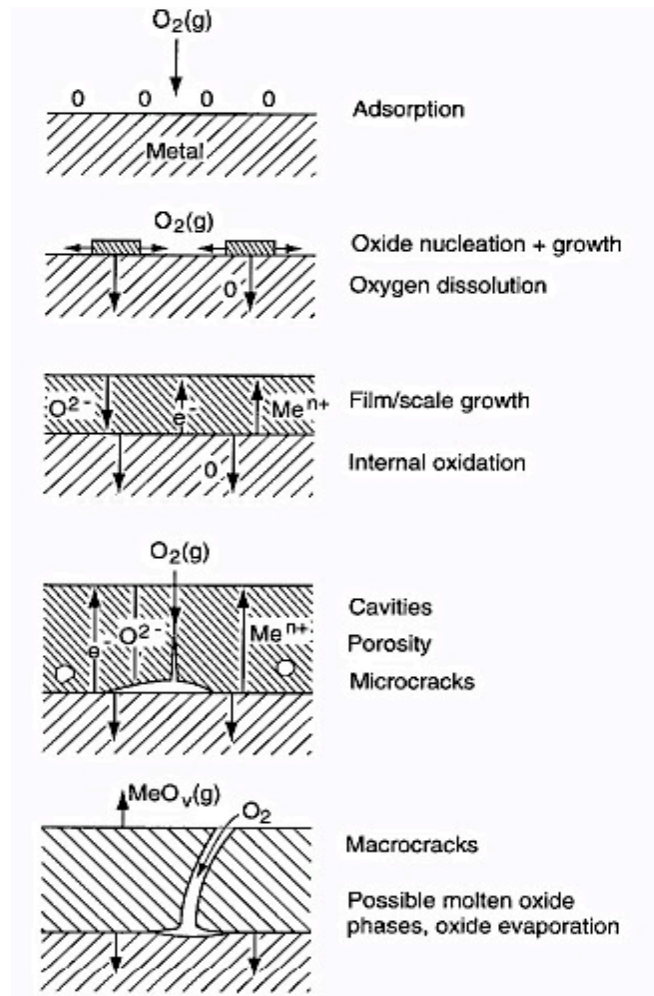
Figure 2.2: Schematic of the oxidation process on a metal surface [13].

Figure 2.2 shows that surface oxide particles nucleate at oxide-former sites, and grow laterally toward one another. Strong oxide formers allow the oxide particles to quickly grow and coalesce to form a stable, continuous film, protecting the underlying metal from further oxidation. However, the oxide at the surface acts as a solid-state electrolyte, which, like water on the surface of steel, continues to conduct electrons, causing further oxidation. Over time, the oxide film grows outward from the surface of the metal, and can thicken into a non-protective scale with defects such as voids and cracks.

The mechanics of oxide growth depend heavily on the chemistry of the oxidizing material, since some elements such as Cr and Al tend to form dense, adherent oxides and others tend to form porous, non-protective oxide scales [17], such as those rich in Ni.

2.3 General Structure of a Nickel Oxide

Figure 2.3 shows a general metal oxide lattice that forms during high-temperature oxidation on a pure metal such as nickel. Such oxides are rarely formed in a perfectly stoichiometric ratio of positive to negative charges [13]. That is, there is always either an excess or deficit of metal (or a deficit or excess of oxygen, respectively) ions in the oxide. The resultant relative charge difference in the oxide becomes the driving force for oxidation, and controls the kinetics of the oxidation process. If the oxide contains more oxygen than it does metal, it is considered a "metal-deficit," or "p-type" oxide, which grows outward from the surface of the component by the outward diffusion of metal ions to react with oxygen at the oxide/gas interface. On the other hand, if the oxide contains more metal than it does oxygen, then it is considered a "metal-excess," or "n-type" oxide, which grows inward from the surface by the diffusion of oxygen ions to react with metal ions at the oxide/metal interface [13]. For the remainder of this section, the growth mechanics of a p-type oxide will be explained, as this is the type of oxide that nickel forms, and relevant comparisons to an n-type oxide will be made when necessary.
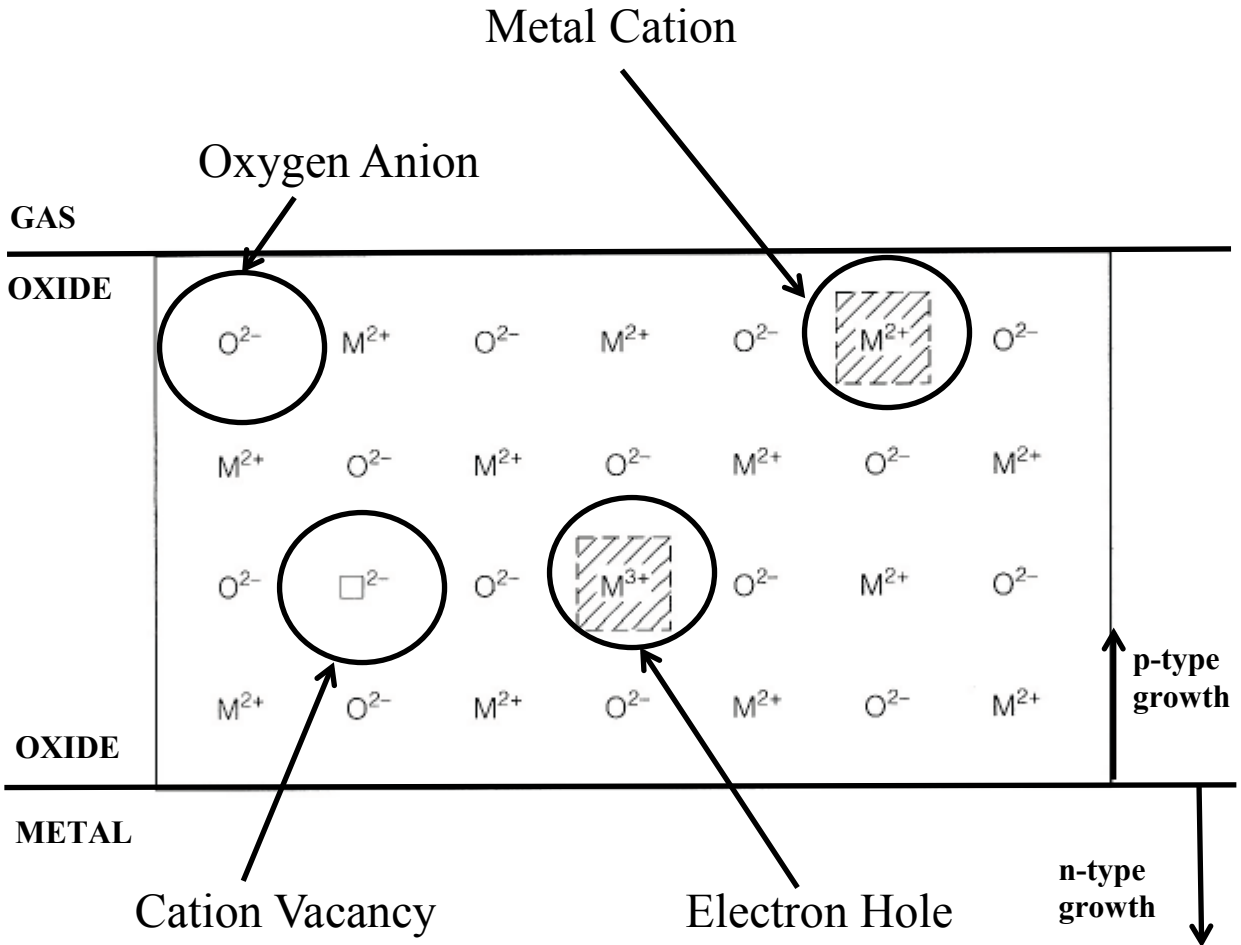
Figure 2.3: Structure of a p-type oxide, such as NiO, which forms atop the surface of a component in an oxygen-containing atmosphere [13].

The oxide lattice is made up of metal cations (M^{2+}), oxygen anions (O^{2-}), cation vacancies ($\square^{2+}$), and electron holes (M^{3+}), as shown above in Figure 2.3. Oxygen anions and metal cations diffuse inward through electron holes and outward through cation vacancies, respectively. This section serves to explain the reactions that take place involving the movement of metal and oxygen ions to form oxide compounds.

Firstly, metal atoms lose electrons to provide metal cations at the metal/oxide interface by [13]:

$$M \rightarrow M^{2+} + 2e^- \tag{2.1}$$

The absence of a metal cation leaves behind a cation vacancy of relative charge (-2) in the oxide lattice. Cation vacancies cause further oxidation, as they serve as spaces through which metal cations migrate to the oxide/gas interface to form oxide compounds. The exchange of metal cations and cation vacancies within the oxide lattice is represented by [13]:

$$M_{ox} \rightarrow M^{2+} + \square_M^{2-} \tag{2.2}$$

Once the metal cations reach the oxide/gas interface via diffusion of metal cations through cation vacancies in the oxide lattice, metal cations at the interface form oxide compounds by [13]:

$$O^{2-} + M^{2+} \rightarrow M_{ox} + O_{ox} \tag{2.3}$$
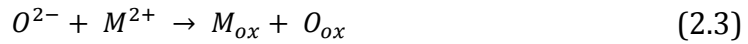
Since electrical neutrality is always desired, the metal oxide wants to create a stoichiometric balance between positively- and negatively-charged ions. Since the metal cations (by losing electrons) have left behind a negatively-charged cation vacancy of relative charge (-2), each cation vacancy must be neutralized electrically by a pair of electron holes of relative charge (+1) each [13]:

$$M^{2+} \rightarrow M^{3+} + e^- \tag{2.4}$$

Electron holes carry current by exchanging electrons with neighbouring normally-charged metal cations. Electron holes migrate from the oxide/gas interface to the oxide/metal interface (inwards from the surface of the oxide to the surface of the metal) by exchanging electrons with neighbouring metal cations [13]. Upon reaching the oxide/metal interface, electron holes are converted to metal cations by accepting electrons from metal atoms within the substrate [13]:

$$M^{3+} + e^- \rightarrow M^{2+} \tag{2.5}$$

The process has come back full-circle to where it began, with the creation of a metal cation. The oxidation process is shown in the schematic of Figure 2.4. The inward diffusion of electron holes by exchanging electrons with metal cations is highlighted in blue and the outward diffusion of metal cations through cation vacancies is highlighted in red. Note that in an n-type oxide, the inward diffusion of oxygen anions to react with metal cations at the metal/oxide interface is the mechanism for the internal oxide formation.
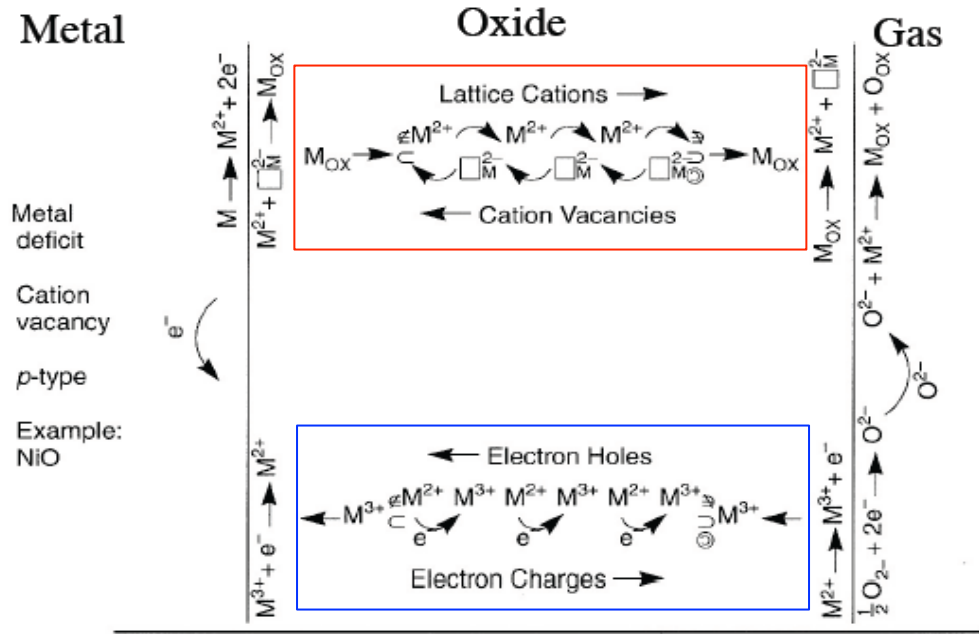
Figure 2.4: The transfer of cations, cation vacancies, electrons, and electron holes within the oxide lattice during oxidation. Metal cations travel to the oxide/gas interface through cation vacancies, and electron holes move inward to the metal/oxide interface by exchange with electrons [13].

In essence, metal cations are created when electron holes accept electrons from metal atoms at the metal/oxide interface. The formation of a metal cation leaves behind a cation vacancy, through which the metal cations diffuse to reach the oxide/gas interface. To balance the relative charge induced by the cation vacancies, electron holes are created, which diffuse inward from the oxide/gas interface to the metal/oxide interface. Once the electron holes reach the metal/oxide interface, they react with metal atoms to form metal cations, which again diffuse through the oxide toward the oxygen-containing atmosphere to cause further oxidation. The process of p-type oxidation is a cyclic process driven by the formation and diffusion of metal cations and electron holes.

11

2.4 Effects of Alloying on the Growth Rate of a Nickel Oxide

Alloying elements can have a strong effect on the mechanics and kinetics of a material's overall oxidation behaviour. This section will provide details on how other alloying elements can affect the oxidation of a nickel alloy.

2.4.1 Titanium

An extra titanium ion in the oxide lattice replaces a cation vacancy, thus reducing the number of cation vacancies present in the oxide lattice [13]. Since the number of cation vacancies is reduced, it is more difficult for metal cations to diffuse out of the metal oxide, and as a result, the rate of oxidation is reduced [18]. Titanium is therefore an element that reduces the oxide growth rate in a nickel alloy, not by forming a protective oxide layer, but by reducing the number of spaces through which metal and/or oxygen ions can diffuse.

2.4.2 Chromium and Aluminum

Chromium ions in the oxide lattice replace former metal cations, thereby introducing excess positive charges to the lattice, and as such, charge neutrality is maintained only by the creation of additional cation vacancies. Thus, the presence of Cr cations increases the number of cation vacancies present in the oxide lattice, which in turn increases the rate of diffusion of metal cations and/or oxygen anions, and therefore the rate of oxidation.

Although the nature of chromium ion addition to the oxide lattice causes an increase in the growth rate of a nickel oxide, the oxidation rate of a nickel alloy containing Cr is dependent on the amount of Cr present [13].

Figure 2.5 shows the effect of Chromium content on an alloy's oxidation kinetics. It can be seen that adding more than 5% Cr causes the oxidation kinetics of a Ni alloy to decrease rapidly. This can be attributed to the fact that with Cr additions of less than 5%, there is not enough Cr present to form a stable, dense oxide film [13]. Therefore, additions of an appropriate amount of Cr can reduce the oxidation rate of a material due to the fast formation of a protective oxide film.
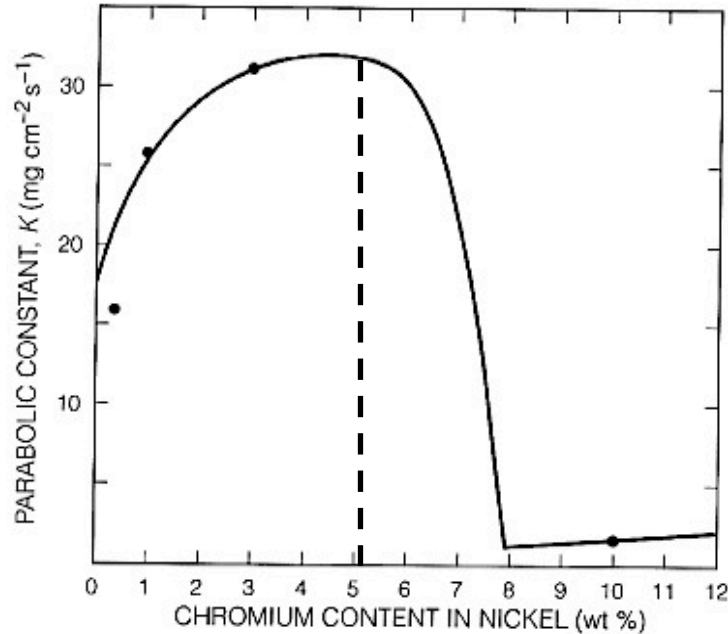
Figure 2.5: Effect of Cr content on the oxidation rate of a nickel alloy. For Cr additions above 5%, the oxidation rate slows dramatically (after [13]).

Aluminum has a similar effect on the oxidation kinetics of a Ni alloy. Aluminum is generally added to nickel-based superalloys to cause gamma-prime strengthening; however, a beneficial side effect is the increased oxidation resistance it provides [2,10]. The aluminum oxide that forms on a superalloy grows at a slower rate than a chromium oxide, but it is generally a more stable oxide than chromia, and as a result, can more effectively slow the diffusion of base metal ions [11]. However, it has been shown that maximum oxidation resistance comes from a continuous layer of aluminum oxide, which can only be formed if the Al content in a material is greater then 5-7% [10].

2.4.3 Complex Oxide Growth in Nickel-Based Superalloys

Trexler *et al.* [19] performed oxidation on samples of GTD111 at 982°C for 312 hours. The multilayer growth observed was broken down into three regions, including an "outer oxide layer" consisting of mostly Ti and Cr, an "inner oxide layer" containing large amounts of Al and Ni, and a gamma prime depleted zone, as can be seen in Figure 2.6. Although the "outer oxide layer" is difficult to see, the "inner oxide layer" can be seen to contain at least two distinct regions, as the dark islands are surrounded by another phase. The results of this thesis will clarify the different phases observed in this region.

13

Figure 2.6: Micrograph of the distinct oxide regions observed on GTD111 after oxidation at 982°C for 312 hours [19].

Liu *et al.* [16] oxidized the DD8 nickel-based superalloy in single-crystal, poly-crystalline, and nano-crystalline forms for 50 hours at 1000°C in an environment containing oxygen and water vapour. Figure 2.7 shows that in this study, an outermost TiO layer was observed, beneath which was a middle layer of Cr_2O_3, followed by the innermost discontinuous layer of Al_2O_3. Liu et al concluded that the oxides of Al and Ti formed first, due to their lower formation energies than other oxides, and that the Chromia layer formed last.
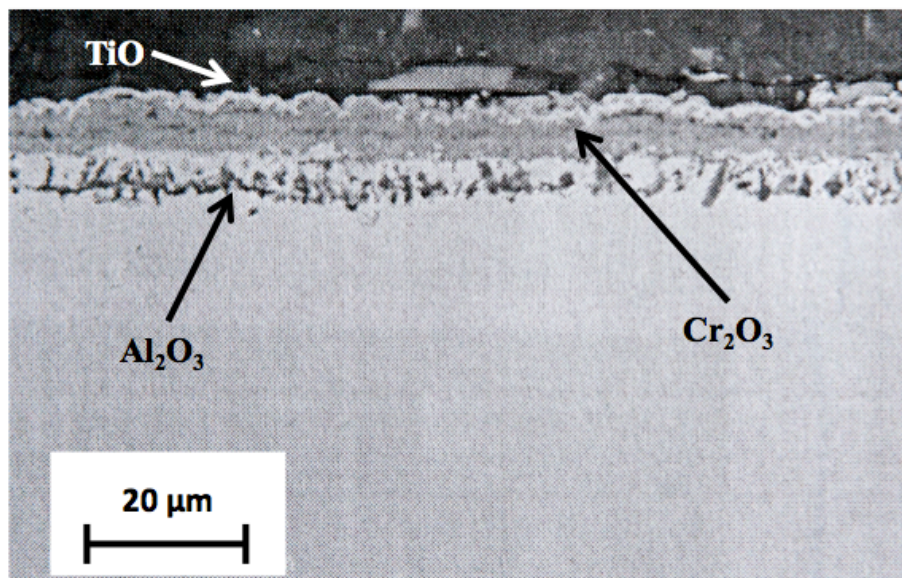
Figure 2.7: Oxide structure found on nickel-based superalloy DD8 after 50 hours at 1000°C (after [12]).

14

Sato *et al.* [10] oxidized prototype single-crystal nickel-based superalloys of varying silicon content at 900°C for 100 hours, and again observed three distinct regions of growth. An outermost continuous Chromia layer formed above a middle oxide layer rich in Ni and Ta, with an internal discontinuous region of alumina, as can be seen in Figure 2.8.
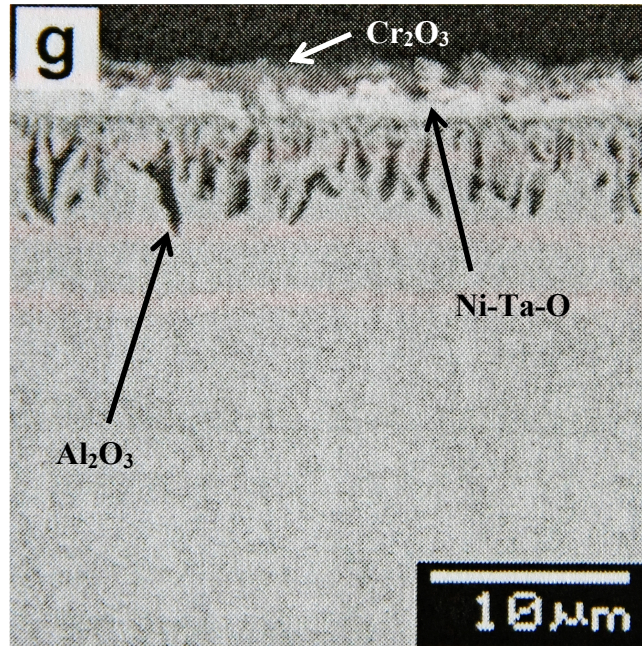
Figure 2.8: A prototype nickel-based superalloy, without Ti additions, oxidized for 100 hours at 900°C shows, three layers of oxide growth (after [4]).

The review of literature concerning the high-temperature oxidation of nickel-based superalloys has shown, at most, three regions of oxide formation within the observed oxide structures. Also, the level of analysis of these studies has left something to be desired. For example, Figure 2.6 showed the results of oxidizing GTD111 at 982°C for 312 hours. The "inner oxide layer" appeared to be made up of at least two regions, including a dark discontinuous region, above which was a thin brighter band. In the current study, the distinct regions of formation within the oxide structure of GTD111 will be analyzed in greater detail. Also, very few studies have analyzed the effect of time on the oxide structure of nickel-based superalloys, and no such study was found for GTD111.

2.4.4 The Effect of Oxidation Brazing

It has been explained that the oxide scales formed on service-run superalloy components, although beneficial in terms of slowing the overall oxidation process, can be detrimental to the service lives of said components, and when a repair is necessary, such scales present another problem altogether. In order for a brazing repair process to be successful, the molten filler metal must be able to wet and adhere to the surface of the substrate. Oxidation is a very strong inhibitor of a molten metal's wettability on a surface. However, regardless of a filler material's ability to wet an oxidized surface, a successful diffusion brazing process cannot be performed atop oxidation because an oxide presents a mechanical discontinuity, which inhibits the formation of an acceptable bond [20]. In order for a repair to be achieved with both wetting and adhesion of the molten filler metal on the substrate, oxide scales should be fully removed from a component prior to the brazing repair process, regardless of the filler metal to be used.

2.5 Fluoride-Ion Cleaning for Oxide Removal

Since a successful braze-repair cannot be applied to an oxidized component, complex oxide scales formed must be fully removed from service-run turbine blades prior to the diffusion brazing process. In industry today, two viable options for superalloy oxide removal exist [1,21]. Mechanical cleaning is possible but involves machining the oxide from the sample, which can prove labour-intensive and costly, considering the unique geometry of most repairs [22]. Since the oxides on superalloy components are found both at the surface and within the immediate subsurface of the material, this machining requires the removal of a small amount of bulk material. This bulk removal is undesirable, as it results in larger regions that need to be filled with a material different than the base metal. The other option is to remove only the oxide, via a strong chemical cleaning process.

The dynamic Fluoride-Ion Cleaning (FIC) process uses flowing HF and H gases – either pressurized or under vacuum – to remove oxide scales from components [1] by converting oxide compounds to water and volatile, removable fluorides. This process has resulted from the need to address deficiencies such as the effectiveness of the reductions and control of process parameters in past processes, which are described briefly below.

Hydrogen Bright Annealing, one of the oldest cleaning processes used prior to diffusion brazing repair, removes oxides formed on metal components via dry hydrogen reduction at approximately 1200 °C. This process worked well on older materials, but as operating temperatures began to increase, the need for increased strength and oxidation resistance meant the development of alloys with higher amounts of Al,

Ti, and Cr, whose oxides were much too stable to be reduced by hydrogen alone. The two processes following Hydrogen Bright Annealing were the Chromous Fluoride Process developed by General Electric and the Fluorocarbon (Dayton) Cleaning Process developed at the University of Dayton. Both processes reacted a substance such as Teflon with hydrogen to create HF indirectly, which resulted in inconsistent cleaning due to poor control of process parameters and the decreased strength of the HF gas produced [1].

2.5.1 Basic Principles of FIC

Figure 2.9 presents a schematic of the proprietary FIC setup at Ti-Coating Inc. The dynamic FIC process begins by loading samples in a furnace (Reactor), into which flowing hydrogen and HF gases are injected from the HF tank heater. Reaction products are purged from the system and are sent to the Scrubber and Neutralizing System. Since FIC processes are proprietary, specific parameters are not given in documentation. However, the operating ranges of temperature and HF concentration have been stated. The FIC process at T-Coating is generally conducted between temperatures of 900 and 1100°C, as HF gas is reactive with oxide compounds at temperatures greater than 800°C. The concentration of HF in hydrogen is typically within the range of 5 and 25%, and alternating stages of HF and H injection are used to continually sweep away water and fluoride products from the surface of the component [1].
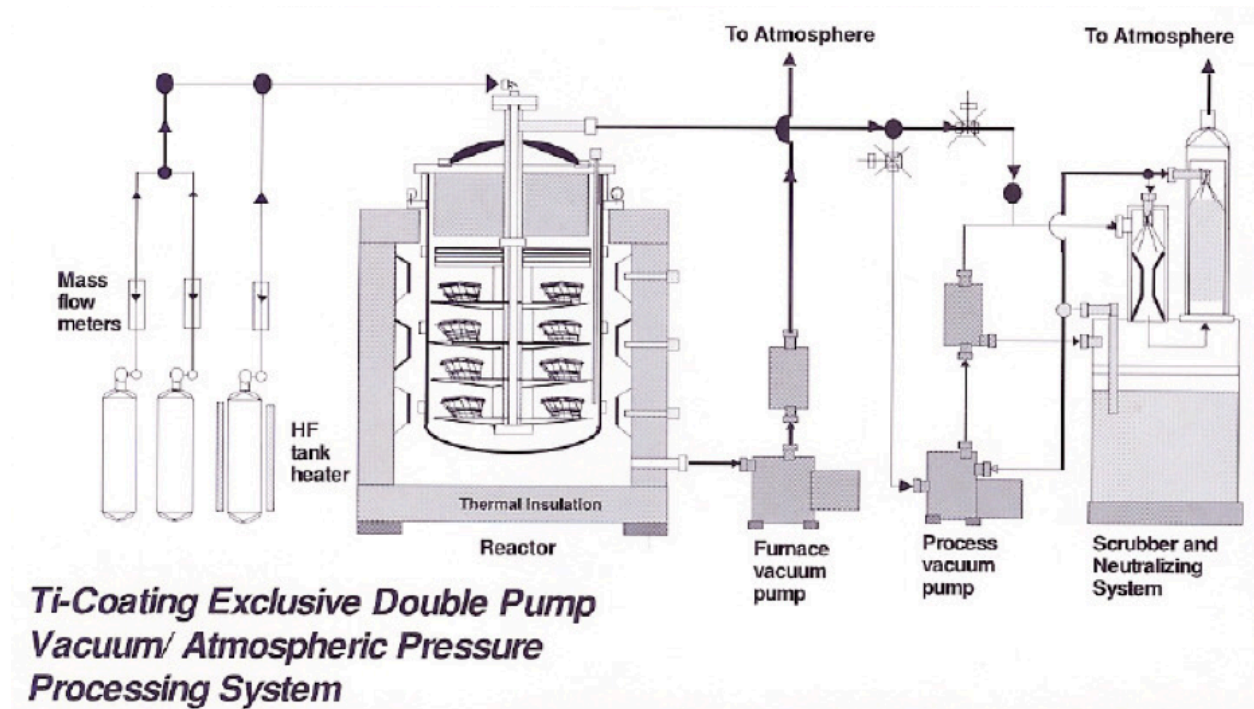
Figure 2.9: Schematic of the Ti Coating proprietary FIC process [1].

The end result of the FIC process is the removal of oxide compounds and the depletion of oxide formers such as Al and Ti from the surface of the component [1,8,21,22]. The depletion of strong oxide formers is necessary to help prevent future oxidation in the time between cleaning and the repair process and to provide better wetting characteristics during the brazing repair process, as the vacancies caused by the depletion of alloying elements increases adhesion of the molten filler metal [1,8].

2.5.2 Chemical Reactions During FIC

Fluoride ions in the HF gas react with the oxide compounds and metal particles at the surface and within the subsurface of the substrate according to the following sets of reactions:

Typical Cleaning Chemical Reactions

$$6HF + Al_2O_3 \rightleftharpoons 2AlF_3 + 3H_2O$$
$$4HF + TiO_2 \rightleftharpoons TiF_4 + 2H_2O$$
$$6HF + Cr_2O_3 \rightleftharpoons 2CrF_3 + 3H_2O$$
$$4HF + NiO_2 \rightleftharpoons NiF_4 + 2H_2O$$
$$6HF + Co_2O_3 \rightleftharpoons 2CoF_3 + 3H_2O$$
$$6HF + Y_2O_3 \rightleftharpoons 2YF_3 + 3H_2O$$
$$4HF + SiO_2 \rightleftharpoons SiF_4 + 2H_2O$$
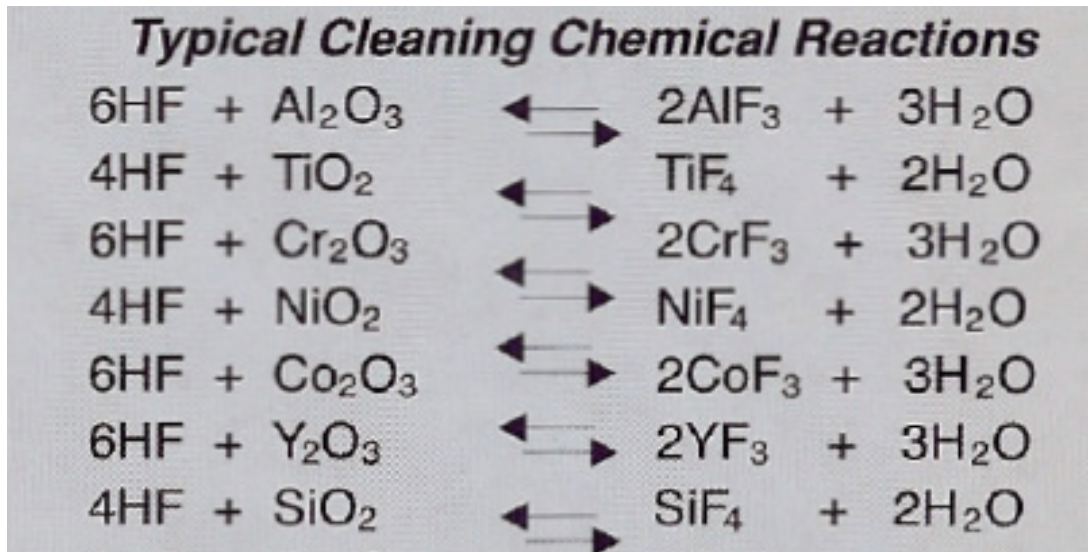
Figure 2.10: List of the chemical reactions that take place on the surface scales of an oxidized component during the FIC process [1].

Typical Surface Depletion Chemical Reactions

$$3HF + Al \rightarrow AlF_3 + 3/2H_2$$
$$4HF + Ti \rightarrow TiF_4 + 2H_2$$
$$3HF + Y \rightarrow YF + 3/2H_2$$
$$6HF + Y_2O3 \rightarrow 2YF_3 + 3H_2O$$
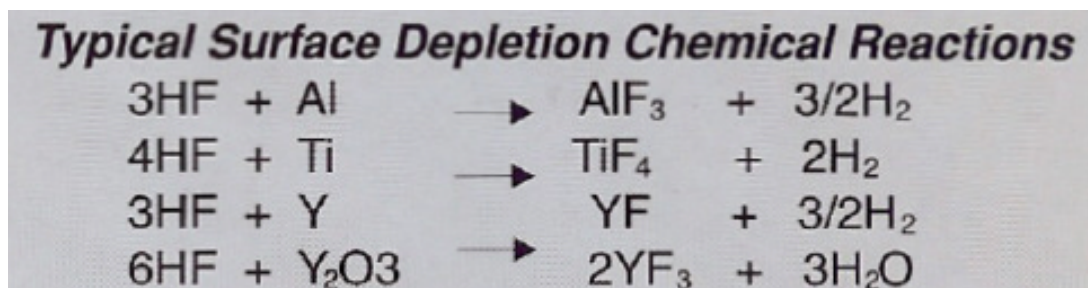
Figure 2.11: List of the desirable chemical reactions that take place to deplete metal ions such as Al and Ti at the surface and in the immediate subsurface of a component during FIC [1].

18

Typical Alloy Depletion Chemical Reactions

$$3HF + Cr \rightleftharpoons CrF_3 + 3/2H_2$$
$$3HF + Co \rightleftharpoons CoF_3 + 3/2H_2$$
$$3HF + Fe \rightleftharpoons FeF_3 + 3/2H_2$$
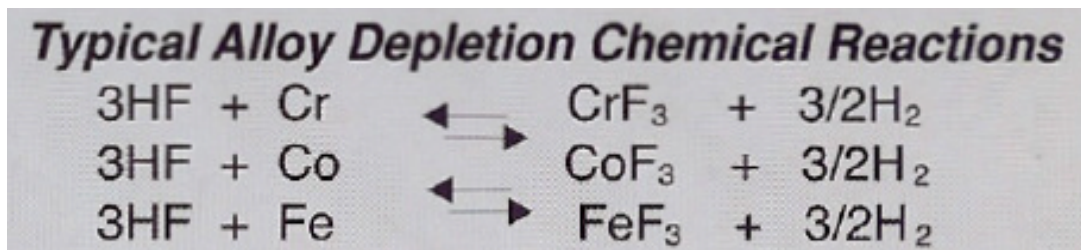
Figure 2.12: List of the undesirable chemical reactions that take place to deplete alloying elements within a component during the FIC process [1].

The first set of reactions in Figure 2.10 – the Typical Cleaning Chemical Reactions – describes the typical oxide films or scales removed by the FIC process, as the flowing HF gas converts the oxide compounds to water and volatile fluorides. Most of these films and scales are present on oxidized superalloy components, and the FIC process parameters are adjusted to maximize the effects of these reactions [1]. Following the Cleaning Reactions are the Typical Surface Depletion Reactions (Figure 2.11), which describe the depletion of strong oxide formers from the surface and subsurface of the cleaned component in order to reduce future oxidation and improve wettability and adherence of the molten filler metal on the substrate. Process parameters are adjusted to keep the depletion of strong oxide formers to a depth of less than 30 μm [1]. The final set of reactions in Figure 2.12 describes the undesirable "Alloy Depletion Reactions," and accounts for some of the other alloying elements typically added to nickel-based superalloys. The depletions of these elements are inherent in the process, but are kept to a minimum via precise control of cleaning process parameters [1].

All of the reactions listed above result in the production of removable hydrogen, water, and volatile fluoride compounds. These products are continually swept from the component's surface and purged from the system during the cleaning process to prevent the reactions from reaching equilibrium. If the products are not removed quickly, the driving force for the cleaning process will disappear, as fresh HF is required to maintain the effectiveness of the reactions. To accomplish this, alternating stages of HF and pure H injection are applied, continually forcing water and fluorides from the surface of the component [1].

It is important to note that very careful selection and monitoring of process parameters is crucial to the FIC process. Improper selection or maintenance of processing parameters such as gas flow rate and HF concentration can result in the decreased effectiveness of the desired reactions or the unwanted excessive depletion of alloying elements [1]. Past studies have found that different cleaning processes result in varying degrees of depletion. For example the Ti-Coating technical report [1] observed Al and Ti

depletions of 12 μm, whereas Miglietti and Blum [21] observed such depletions to a depth of only 5 to 7 μm. The depletion depth could be both process- and material-related, and as such it is important to determine the effects of a specific process on a given material.

The Ti-coating website and technical paper [1] do not indicate that GTD111 have been cleaned via FIC, and no past studies have been found concerning the cleaning of GTD111, so in the current study, the chemical effects of the cleaning process on this alloy will be determined. Also, past studies have not identified the dependence of the resultant chemistry after FIC on the prior oxidation time, so this relationship will be addressed in the current study, in order to determine if a cleaning process must be tailored for a specific oxidation time

2.6 Introduction to Activated Diffusion Brazing

As a result of the high costs of nickel-based superalloy components, it is necessary to subject damaged turbine blades to a repair procedure to increase their service lifetimes [5]. For this reason, there is a high demand for repair procedures that will restore components to their original structure and functionality by creating a defect-free repaired region that resembles the base metal as closely as possible [23]. The repair procedure required for a specific component will depend on the shape and size of the damaged area and the loading to be experienced at the specific location on the component [23].

2.6.1 Limitations of Previous Processes for Superalloy Repair

Repairs using fusion welding and conventional brazing techniques have been explored [6], but with little success. Nickel-based superalloys are precipitation-hardened by additions of titanium and aluminum, and are therefore susceptible to Heat-Affected Zone (HAZ) cracking and distortion [24] due to the high heating and cooling rates experienced during fusion welding processes. Also, processes tuned for the welding of superalloy components can be very complex and/or impractical to carry out on a large scale [25]. Another issue with fusion welding techniques is that the filler metals used are often of much lower strength than the superalloy to be repaired, restricting the repair process to non-critical regions or components [12].

Conventional brazing processes have also proven unsatisfactory for superalloy components, due to the low melting temperatures of conventional brazing alloys and the hard, brittle intermetallics that form during the brazing process [5,24]. The low melting temperatures of the brazing alloys render repaired components useless in the high-temperature, high-stress environment of turbine hot sections, and the intermetallics are detrimental to the component's mechanical properties and corrosion resistance.

To overcome the issues preventing fusion welding and conventional brazing from successfully restoring superalloy components to their original functionality, a process called Activated Diffusion Brazing, a wide-clearance variation of the Transient Liquid-Phase Bonding process, has been developed. Activated Diffusion Brazing (ADB) employs a two-part filler metal mixture of a material close in composition to the base metal plus an active element, called a Melting Point Depressant (MPD) such as boron, silicon, or phosphorus. The MPD decreases the melting point of the mixture and promotes diffusion of the brazing material into the base metal during isothermal holding at the bonding temperature [24].

2.6.2 Advantages and Limitations of the Diffusion Brazing Process

Some of the main advantages to the diffusion brazing process are summarized below:

- The diffusion brazing process can combine the repair of external damages with a heat-treatment intended to improve the properties of both the repaired region and the overall component [26]
- Thermal stresses, distortion, and HAZ-cracking can be avoided by the slow heating and cooling rates employed during the diffusion brazing repair process [26]
- Isothermal holding at the bonding temperature can drastically reduce or even eliminate the harmful intermetallics that form within the brazed region, by allowing sufficient time for the intermetallics to diffuse into and disperse within the base metal, creating joints that can be virtually indistinguishable from the base metal [21]
- Parts can be batch-processed to result in lower unit repair costs, provided the combination of component and equipment size is suitable for multi-component repair [31]
- Due to the absence of brittle intermetallics in the brazed region, diffusion-brazed joints are much stronger than those produced by conventional brazing and fusion welding techniques. Repairs by diffusion brazing are capable of achieving between 90 and 95% of the base metal strength [6]

Some of the main limitations to the diffusion brazing process are summarized below:

- Since the dense oxide scales that form on a superalloy during service inhibit wetting of and adhesion to the surface by the molten filler metal, all oxidation products must be removed from the component's surface prior to brazing by mechanical or chemical processing [1]
- Due to the ease with which strong oxides form on superalloy surfaces, a high level of vacuum must be achieved before the heating process can begin. Otherwise, the formation of tenacious oxides can occur before the brazing filler can melt and adhere to the substrate [7,12]
- Long processing times are generally required, to allow for adequate removal of the harmful intermetallics inherent in the diffusion brazing repair process [27]
- Due to the wide range of repair geometries, process parameters must be tailored to each repair, and can have a major effect on the quality of repair that can be achieved [11,25]

2.7 Basic Principles Activated Diffusion Brazing

2.7.1 Description of the Process and Materials

In the Activated Diffusion Brazing process, a two-part filler metal powder mixture is placed inside or over top of a damaged region on a component and inter-diffusion between the filler material and the base metal can create a repaired region similar in strength and microstructure to that of the base metal. The two-part powder mixture consists of a base metal powder (BPM) and a filler metal powder (FMP).

The BMP is a powder made of an alloy very similar or identical in composition to the base metal to be repaired. In the case of a nickel-based superalloy repair, the BMP is made either of that specific superalloy, or another superalloy of very similar composition. To prevent strong oxides from preferentially forming on certain constituents such as Ti and Al in the powder mixture, the base metal power generally comes in a pre-alloyed condition. Superalloy ingots are melted and poured into a gas atomization chamber, where cold gas causes rapid solidification of the melt to create fine, spherical, pre-alloyed base metal particles. This process of powder manufacturing ensures that little-to-no oxidation of powder particles occurs, which allows for diffusion brazing to be performed without the use of flux [28].

The FMP contains mostly the main elements in the metal to be repaired, as well as Melting Point Depressants (MPD) such as boron, silicon, and phosphorus, to promote melting, diffusion, and flow of the molten filler metal powder mixture. In the case of nickel-based superalloy repair, the FMP contains

mostly nickel. Silicon and phosphorus, when used as the MPD in such a system, can cause large amounts of base metal deterioration [29], which can be undesirable in the repair process. For this reason, filler metal powders containing boron as the MPD are desired for diffusion brazing repair.

2.7.2 Initial Conditions

Initially, a two-part filler metal powder consisting of a base metal powder and an MPD-containing filler metal powder is made into a paste and placed within the damaged region, as shown in Figure 2.13. The component is then placed in a vacuum furnace, where the remainder of the process is carried out.
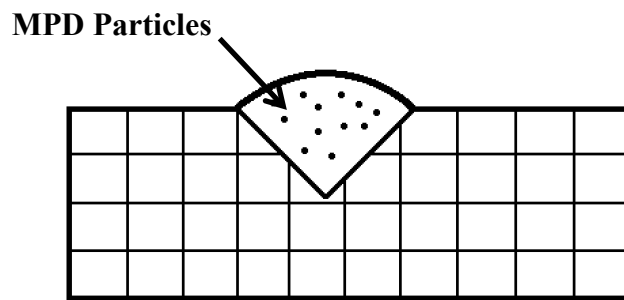
Figure 2.13: Initial conditions of the ADB process.

2.7.3 Heating Stage

The process begins with the Heating Stage. Upon heating, a small amount of inter-diffusion occurs between the interlayer and base material. A small amount of the melting point depressant diffuses into the base material during this stage [29]. The role of the MPD in the powder mixture is to ensure that melting occurs at a temperature much less than that of the base metal, and to promote homogenization of the repaired region.

2.7.4 Dissolution and Widening Stage

The dissolution and widening stage begins at the onset of melting. The MPD causes the powder mixture to melt before the melting point of the base metal, but the molten filler material causes melting of the adjacent substrate surface, resulting in a slight widening of the liquid region as shown in Figure 2.14. The amount of widening can be controlled by the MPDs used, as Si and P cause much more base metal melting (or deterioration) than is caused by boron [30]. At the end of this stage, the liquid width is at its maximum, and solidification will begin.
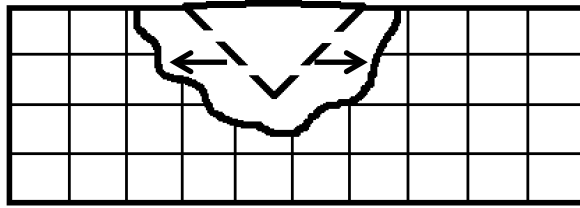
Figure 2.14: Dissolution and widening stage of the ADB process.

2.7.5 Isothermal Solidification Stage

The isothermal solidification stage takes place at the bonding temperature, where the Solid-Liquid interface moves back toward what will be the bond centreline. Solidification continues until the solid-liquid interfaces from each side of the joint meet in the middle of the repaired region. The MPD particles will be pulled along with the retreating liquid toward the centreline, resulting in a peak in MPD concentration [28].
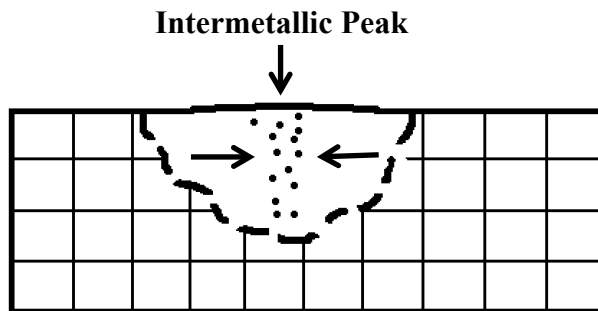
Figure 2.15: Isothermal solidification stage of the ADB process.

2.7.6 Homogenization Stage

In order to eliminate the harmful intermetallics at the joint centreline, which act as stress concentrations under loading, homogenization of the brazed region must occur. During homogenization, the sample is held at the bonding temperature for a sufficient period of time to cause diffusion of the intermetallics out of the brazed region and their dispersion within the base metal.
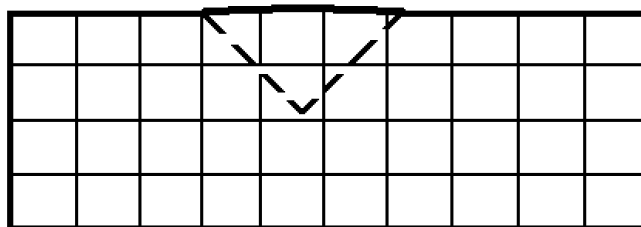
Figure 2.16: Homogenization stage of the ADB process.

24

The end result of a joint created using the ADB process can be a homogenous, nearly invisible joint with near-base metal properties [6]. It should be almost impossible to tell where the base metal ends and the repaired region begins when ADB is completed. The micrographs of Figure 2.17 show liquid widening, solidification, and a homogenized structure, respectively, after bonding times of 8, 240, and 960 minutes during transient liquid-phase bonding of pure Ni with a Ni-B interlayer at 1140°C.
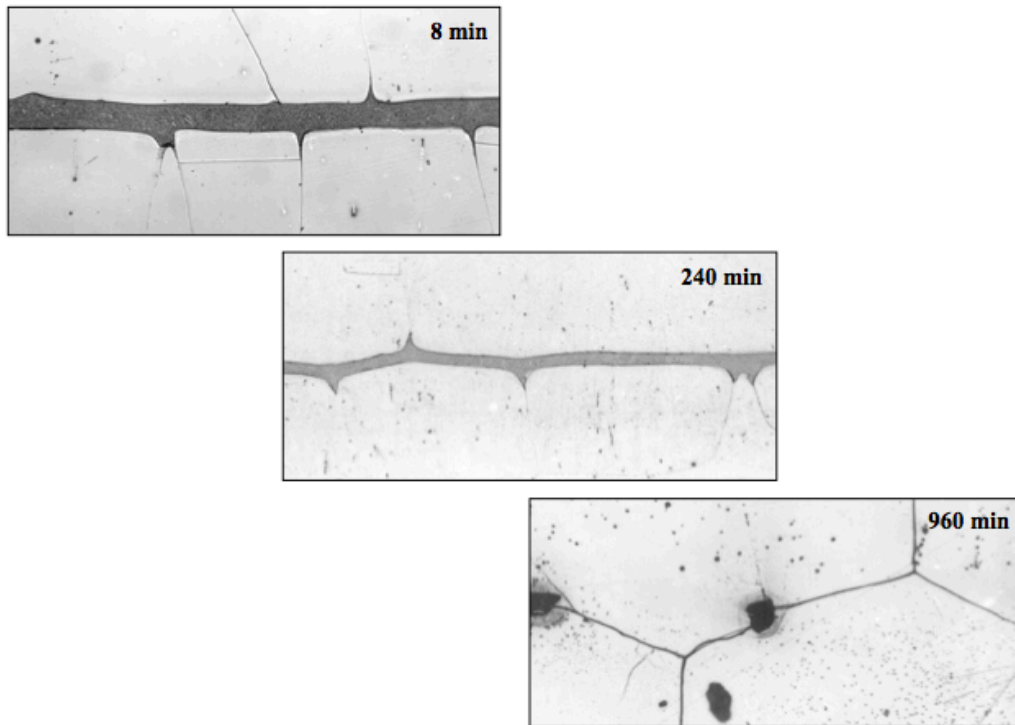
Figure 2.17: Optical micrographs taken after bonding times of 8, 240, and 960 minutes during the TLP process [31].

2.8 The Importance and Effects of Diffusion Brazing Process Parameters

Activated Diffusion Brazing relies on the ability of a filler metal powder mixture to melt and flow within a notch, to diffuse into the substrate, and to solidify into a repair free of defects such as porosity and intermetallics. There are many factors to consider when planning a repair process, as the width, depth, and shape complexity of the region to be repaired will require a complex combination of processing parameters. For example, a wide, shallow notch will require a paste to be made with a mixing ratio and viscosity very different from that needed to repair a deep, narrow crack [29]. An explanation of the four main processing parameters of mixing ratio, viscosity, time, and temperature are explained in more detail below.

2.8.1 Mixing Ratio

The ratio in which the two powders are mixed is very important to the repair process, and can have a large effect on porosity, density, mechanical properties, and the microstructure that can be obtained from the repair. For example, the MPD-containing filler metal powder has very low strength when used on its own. For large gap sizes that require a large amount of filler material, a mixture high in filler metal powder would result in a large section of weak material, and the repaired area would be much weaker than the bulk of the component. On the other hand, a very small gap size requires a higher amount of filler metal powder in the mixture, because the mixture needs to flow easily within the small gap to ensure adequate filling into the tip of the notch [29].

Kim *et al.* [6,27] performed wide-gap diffusion brazing on notches of 1.8 mm depth and 2 mm width on IN738 using mixing ratios of – in terms of base metal powder : filler metal powder – 80:20, 70:30, 60:40, 50:50, and 0:100. The mixing ratio was not found to have as strong an effect on the strength of the joints produced as time or temperature [6]. An important observation made was that the optimal filler metal powder content for this size of notch was approximately 40%. Figure 2.18 below shows the effect of filler metal powder content on the strength of diffusion-brazed joints, and it can be seen that there was an increase in strength until the peak seen at 40% filler metal powder, after which the strength began to decrease. The peak in strength came from an optimal compromise between porosity and intermetallic formation, as shown by Figure 2.19.

When a large amount of base metal powder is used, there is a larger sink for the MPD elements, which leads to a reduction in brittle intermetallics in the brazed region, which in turn leads to higher joint strengths. However, with higher amounts of base metal powder, there is also a smaller amount of the more mobile filler metal powder available to fill in-between the base metal powder particles. This decrease in filling leads to higher amounts of porosity and a lower density of filler material within the joint, which can result in stress concentrations and early failure. Therefore, the mixing ratio of 60% base metal powder to 40% filler metal was found to give the optimal compromise between porosity and intermetallic content within the joint [6]. This conclusion has also been stated in a technical report on wide-gap diffusion brazing presented by Sulzer Metco [32].
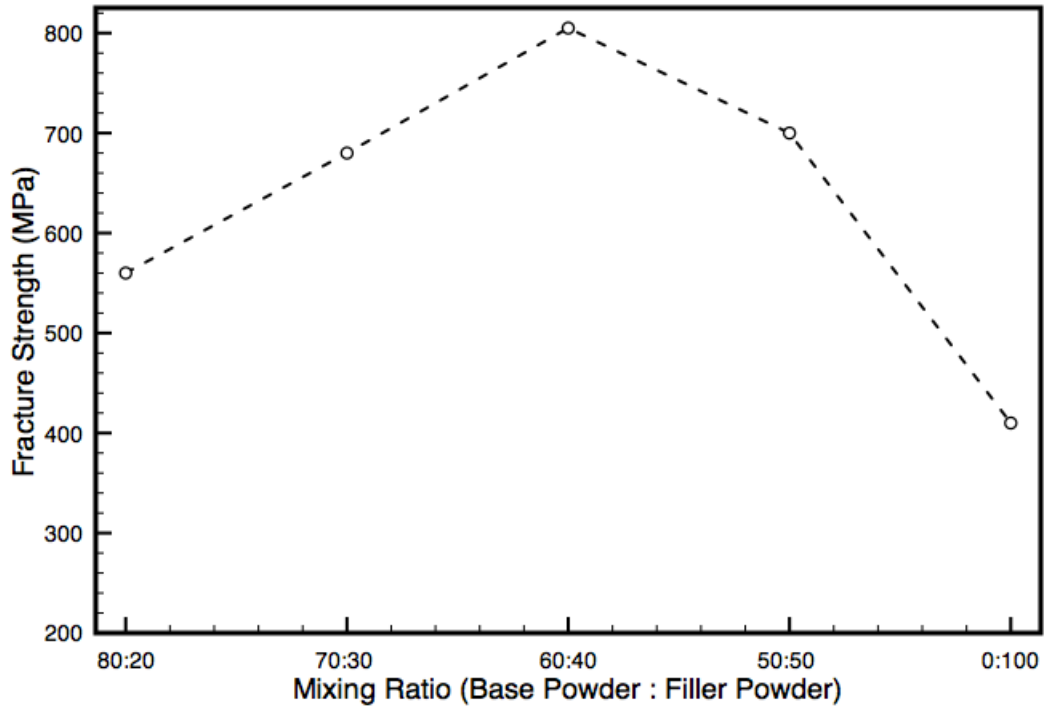
Figure 2.18: The effect of the mixing ratio on the strength of a wide-gap diffusion-brazing repair performed on a 2 mm wide by 1.8 mm deep notch on IN738 (after [6]).
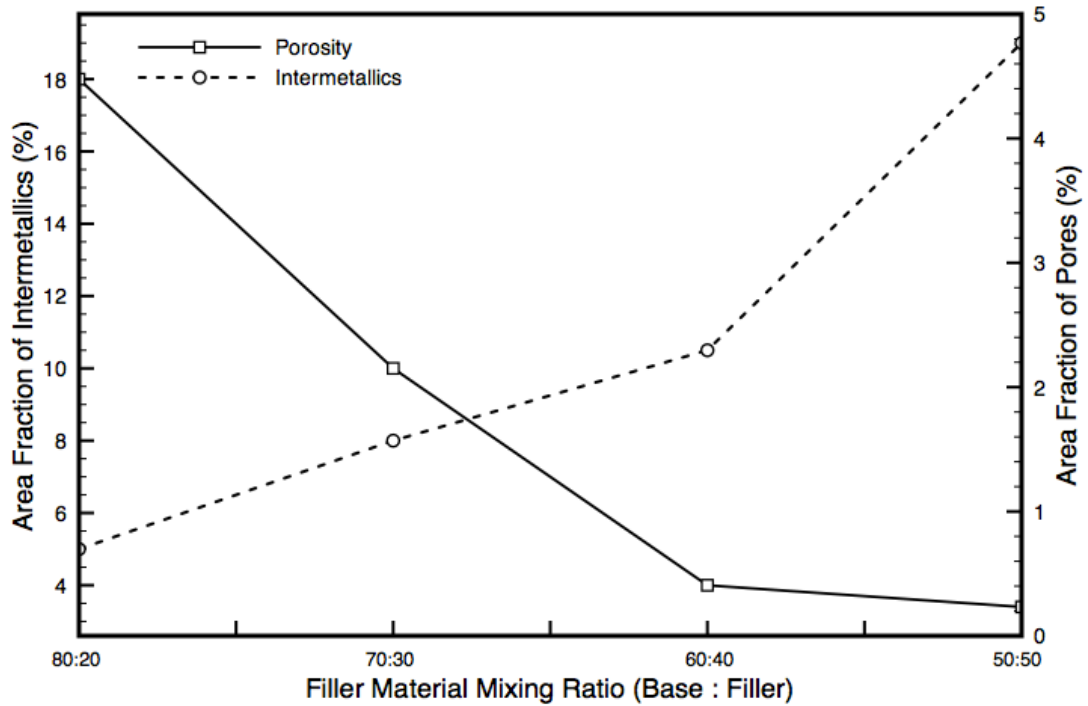
Figure 2.19: The effect of the mixing ratio of base metal and filler metal powders on the formation of intermetallics and pores (after [6]).

2.8.2 Paste Viscosity

Liquid binder is added to the filler metal powder mixture to create a workable paste that will be applied to the damaged area. The binder has a sufficiently low vaporization temperature that it will burn off long before the filler material begins to melt, which means that the binder will have no effect on the chemistry of the repair. The amount of binder added to the powder mixture has a large effect on the viscosity of the paste, and pre-placement of the paste can be very difficult in some damaged regions if a suitable viscosity is not used.

2.8.3 Bonding Time

Time is perhaps one of the most important parameters of the diffusion brazing process. Since the times required for the heating and widening stages are relatively short, "time" generally refers to the time required for the isothermal solidification and homogenization stages. Depending on the geometry of the repair, and the filler material used, these times can change dramatically, as longer times allow for more MPD diffusion out of the brazed region, which can result in higher strength. For example, a smaller gap width requires more of the MPD-containing filler metal powder, and as a result, a higher concentration of intermetallics will need to be removed during the homogenization stage, resulting in a longer overall processing time. On the other hand, a wider gap has more base metal powder, which acts as a sink for the MPD in the filler metal powder, and can allow for shorter homogenization times, as there is a relatively lower concentration of intermetallic-formers present when more base metal powder is used [6].

Kim *et al.* [6,27] performed wide-gap diffusion brazing on notches of 1.8 mm depth and 2 mm width on IN738 for bonding times of 1, 5, 10, and 30 hours at 1200°C. As can be seen in Figure 2.20 below, the fracture strength increases dramatically between 1 and 30 hours of bonding time. However, it is to be noted that the largest impact is seen between 1 and 10 hours, since another 20 hours of holding time results in an increase of only about 30 MPa above the strength achieved after 10 hours. Depending on the application of the repaired component and required throughput, this increase may not be sufficient to deem the longer holding times feasible.
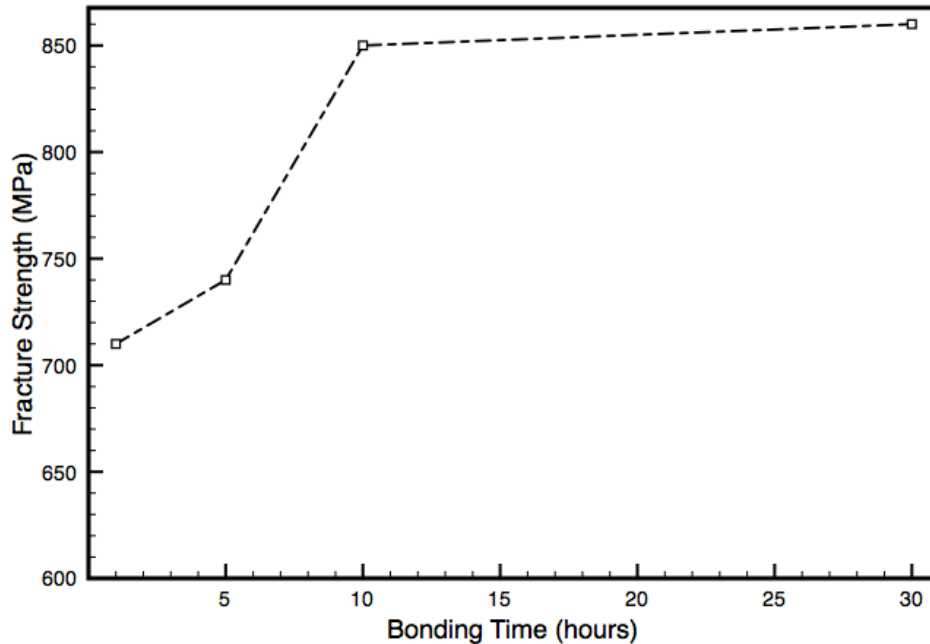
Figure 2.20: The effect of bonding time on the strength of a wide-gap diffusion-brazing repair performed on a 2 mm wide by 1.8 mm deep notch on IN738, at a bonding temperature of 1230°C (after [6]).

2.8.4 Bonding Temperature

The bonding temperature has a strong effect on the wettability and flow of the molten filler metal mixture [6], which allows for better movement of the molten metal into the damaged area and adherence to the surfaces to be repaired. With increased wettability, the molten filler metal will flow more easily, and will more effectively fill voids during the brazing process, and will result in a repaired region with higher density. Also, higher temperatures increase the rate of MPD diffusion out of the brazed region, resulting in faster homogenization times, and potentially stronger repairs when compared to repairs made for similar holding times at lower bonding temperatures [5].

Kim *et al.* [6,27] performed wide-gap diffusion brazing on notches of 1.8 mm depth and 2 mm width on IN738 at bonding temperatures of 1170°C, 1200°C, and 1230°C. Higher bonding temperatures increase filler metal powder wettability and intermetallic diffusion from the brazed region [33], and therefore joints created at higher bonding temperatures result in higher fracture strengths. From Figure 2.21, it can be seen that increasing the bonding temperature to 1230°C has essentially the same effect as increasing the bonding time to 10 hours. Therefore, by increasing the bonding temperature, shorter processing times can likely be used to achieve sound repairs from the diffusion brazing process. Ojo *et al.* [5] found that

29

higher bonding temperatures increased the rate of diffusion of intermetallics from the brazed region, resulting in higher strengths at shorter bonding times. However, it was noted that the temperature should not be too high, because adverse effects such as grain growth can occur.
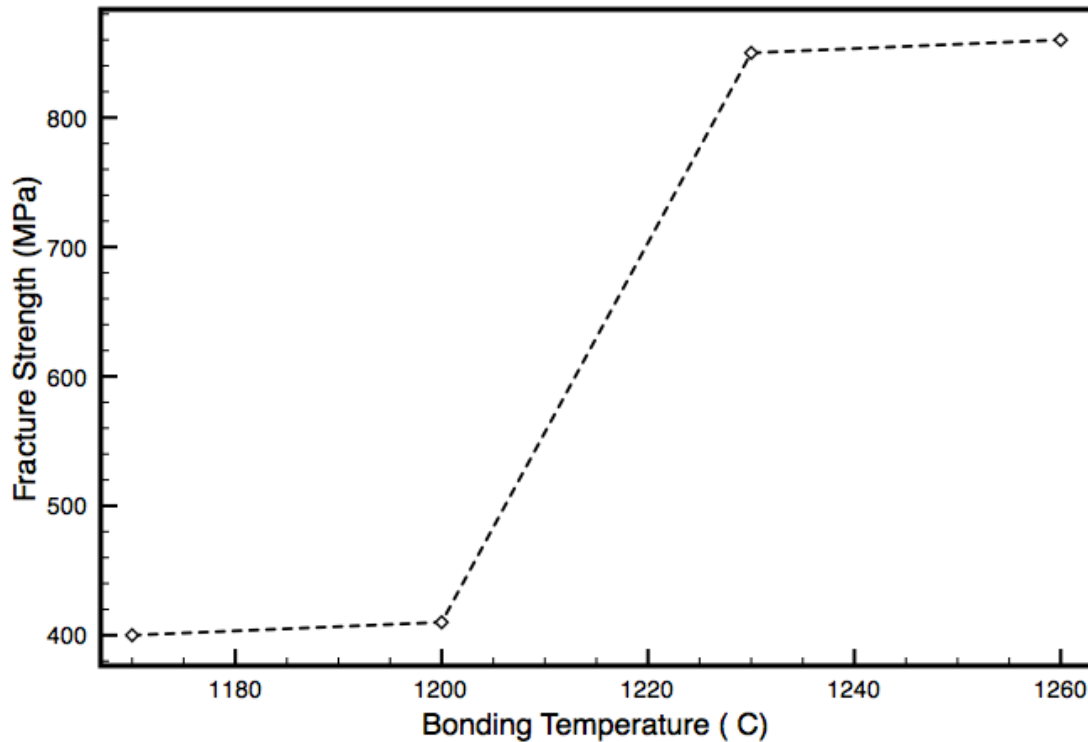
Figure 2.21: The effect of bonding temperature on the strength of a wide-gap diffusion-brazing repair performed on a 2 mm wide by 1.8 mm deep notch on IN738, for a holding time of 10 hours (after [6]).

2.9 The Effect of Gap Size on Diffusion Brazing Repairs

Ojo *et al.* [5] conducted diffusion brazing on gap sizes 30, 60, and 75 μm wide and 2.5 mm deep at bonding and homogenization temperatures of 1120 and 1065°C, respectively in IN738. A major conclusion of this study was that an increase in gap width from 30 to 75 μm resulted in a wider region of eutectic solidification near the joint centreline. This eutectic band was found to be of greater hardness than the base material, but tensile testing results indicated that an increase in gap size – and therefore eutectic width – caused much lower tensile strength and elongation. Another interesting observation from this study was that Al and Ti had diffused into the base metal from the repaired region. It was noted that this diffusion is crucial in terms of maintaining or restoring the main strengthening mechanism of gamma prime phase formation in the region of the repair.

Ch. Lecomte-Mertens [26] performed diffusion brazing on 1.5 mm deep and 360- and 750 μm-wide notches in IN792 between 1200 and 1230°C for holding times of 3 hours using two different filler materials. It was concluded that the repairs made on the larger gap size resulted in higher levels of porosity, that gaps larger than 0.5 mm were not always completely filled, and that brazing filler materials closer in composition to the base metal resulted in more homogenous repairs. This study also concluded that increased bonding temperatures enhanced the diffusion of the brazing filler material into the base metal, which led to shorter homogenization times and therefore an overall faster repair process.

In 2004, Choi *et al.* [40] conducted transient liquid phase bonding of 50 μm gaps in GTD111 at bonding temperatures of 1100 to 1200°C. As with most studies concerning TLP, the main observations were of the eutectic width and solidification time resulting from different bonding temperatures and heating rates. Choi *et al.* [40] was the only publication found to perform bonding on GTD111, but the bonding studied was not that of wide-gap diffusion brazing. The diffusion brazing of GTD111 has not been vastly studied, nor has the brazing of gaps as deep as those attempted in the current study. It was stated by Lecomte-Mertens [26] that notches wider than 0.5 mm and 1.5 mm deep were not always completely filled – as porous repaired regions resulted – and so the current study plans to attempt the filling of even deeper and wider notches in GTD111.

2.10 Summary

Previous studies have shown that oxidation resistance in nickel-based superalloys is largely dependant on the formation of a continuous layer of either chromium or, preferably, aluminum oxide, and that nickel-based superalloys exhibit complex multilayer oxide formation when subjected to high temperatures. It has also been shown that the fluoride-ion cleaning process results in effect oxide removal and the desired depletion of Al and Ti from the surface of a nickel-based superalloy component. In terms of brazing, previous publications have shown the effects of process parameters such as mixing ratio, bonding time, and bonding temperature on the quality and strength of brazing repairs.

The objectives of the current study concern the chemical effects of the processes of oxidation, fluoride-ion cleaning, and activated diffusion brazing on GTD111. Previous publications have not studied the effects of oxidation time on the chemistry and/or structure of the oxidation formed on GTD111, and past studies appear to be lacking detail on the analysis of the oxide regions formed below the surface of GTD111. Although it has been shown that the FIC process is capable of removing oxide compounds and created a depleted zone beneath the surface of cleaned nickel-based superalloys, the effects of the prior oxidation time on the chemistry of samples cleaned via FIC have not been previously analyzed. Furthermore, the effects of the FIC process on GTD111 in particular have not been studied, and the Ti-Coating Technical Report on FIC [1] does not indicate that GTD111 is an alloy that has been successfully cleaned by this process. The activated diffusion brazing (ADB) process has been proven to restore strength to repaired sections of nickel-based superalloys, but literature on GTD111 is quite limited. The objective of the brazing trials in this study is to determine how the chemistry of samples repaired via ADB compares to that of the base metal, considering the depleted region resulting from the FIC process.

The following chapter presents the materials and experimental methods of oxidation, cleaning, and brazing used to obtain the results of this thesis.

Chapter 3 Materials and Experimental Methods

3.1 Materials

3.1.1 Base Metal - GTD111

The substrate chosen for this study was a polycrystalline nickel-based superalloy GTD111, a General Electric (GE) proprietary alloy used for first-stage hot-section turbine blades [34]. The nominal composition of this alloy is shown in Table 3.1. The typical GE process for the manufacture of GTD111 turbine blades involves vacuum-investment casting, followed by hot-isostatic pressing and machining to final tolerances. Subsequent processes include coating application and heat-treatment [33]. GTD111 in the standard heat-treated condition consists of duplex gamma prime (primary and secondary) precipitates evenly distributed within an FCC gamma matrix.

3.1.2 Filler Metal Powders

Since the diffusion brazing process relies heavily on the production of a chemically and microstructurally homogenous joint, careful selection of filler materials was extremely important. That is, it was important to choose a base metal powder as close as possible to the substrate to be repaired, and to choose a filler metal powder containing few alloying elements, as extra elements simply add complexity to the repaired region. With this in mind, the selected filler material powders were chosen from Sulzer Metco's line of superalloy brazing materials. The nominal compositions of the base metal powder, AMDRY 8670, and the filler metal powder, AMDRY 915, are listed in Table 3.1

3.2 Coupon and Notch Sizes

Coupon sizes were kept small (15 mm wide x 12 mm high x 9 mm deep). Six notch sizes were selected to vary the depth-to-width ratio of the simulated damaged region. All notches were 8mm in depth, and ranged from a minimum of 0.25 mm to a maximum of 8 mm in width. A photograph of notched coupons of GTD111 is shown in Figure 3.1.

Figure 3.1: Coupons (15 mm x 12 mm x 9 mm) with notches of 8mm depth and widths of (from left to right) 0.25, 1, 3, 5, and 8 mm.

Table 3.1: Nominal compositions* of the base metal GTD111 [34], base metal powder AMDRY 8670, and filler metal powder AMDRY 915 [33,35].

Element	GTD111	AMDRY 8670	AMDRY 915
Ni	Bal	Bal	Bal
Al	2.8 – 3.2	5.5	--
Cr	13.7 – 14.3	8.4	13.0
Ti	4.7 – 5.1	1.05	--
W	3.5 – 4.1	10.0	--
Ta	2.5 – 3.1	3.05	--
Co	9.0 – 10.0	10.0	--
Mo	1.3 – 1.7	0.65	--
Fe	0.2 – 0.25	--	4.0
C	0.08 – 0.12	0.15	--
B	0.01 – 0.02	0.015	2.8
Si	--	--	4.0

* All values are given in weight %

All coupons and notches were cut using Wire Electro-Discharge Machining (EDM) at Excel Wire EDM, Inc. [42]. The 0.25 mm notch was created from the thinnest EDM wire available, and was the thinnest notch that could be created by this method.

3.3 Oxidation

Coupons containing each notch size were placed in an electric air furnace at 900°C, where high-temperature oxidation would occur. This temperature was chosen to simulate the temperature experienced inside the hot-section of an industrial gas turbine. Initially, samples of each notch size were oxidized at 900°C for 96 hours to ensure that even the smallest notch could be cleaned via the standard FIC process. When this was concluded, notches of 0.25 mm width were oxidized for times of 96, 144, 192, 260, 308, and 452 hours.

3.4 Fluoride-Ion-Cleaning

Oxidized samples were sectioned in half via wire EDM and half of each sample was sent for fluoride-ion cleaning at Ti Coating Inc. [41]. Ti-Coating's "standard" cleaning process [41] was used to clean these samples, in order to determine if a customized process would be required for this material or for certain oxidation times. Samples were returned from the cleaning process in sealed bags to prevent oxidation in the time between cleaning and brazing. A schematic of the FIC equipment is shown below in Figure 3.2, showing the placement of components in the Reactor, which will be cleaned by flowing H and HF gases from the tanks to the left of the Reactor. The reaction products of water, hydrogen, and fluorides are purged from the system to the Scrubber and Neutralizing System.
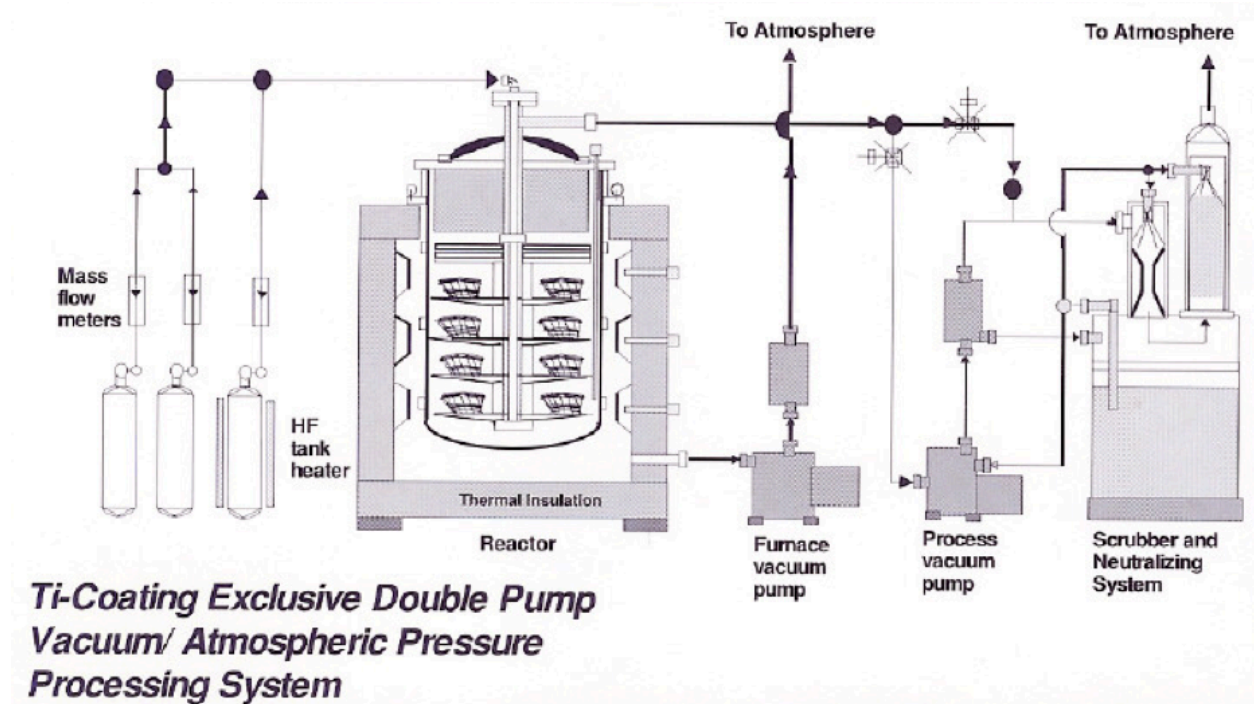
Figure 3.2: Schematic of the FIC Equipment setup at Ti Coating, Inc. [1].

3.5 Diffusion Brazing

3.5.1 Filler Material Mixtures and Pastes

The Activated Diffusion Brazing process employs a two-part filler metal powder mixture of a Base Metal Powder (BMP) and a Filler Metal Powder (FMP). Two-part filler metal powders were created with varying mixing ratios, ranging from 30% BMP : 70% FMP to 70% BMP : 30% FMP. These ratios are given in terms of weight-%, and were accomplished by simply measuring the appropriate weight of each powder required to create ten grams of mixed powder for each ratio. That is, for the 60:40 powder mixture, six grams of base metal powder was added to four grams of filler metal powder in a small glass vial.

In order to achieve complete mixing and avoid segregation of the two different powders, the mixtures were ball-milled in ethanol for approximately four hours at a sufficiently low speed to keep the powders from sticking to the vial walls while spinning, which would ultimately result in unmixed powders. Prior to ball milling, each powder mixture was combined with ten grams of zirconia balls of 3 mm diameter and topped off with ethanol. The lid of each vial was secured with tape to avoid leakage. Figure 3.3 shows a photo of the filler metal powder mixture after initial powder mixing (left) and after combining with zirconia balls and ethanol (right).
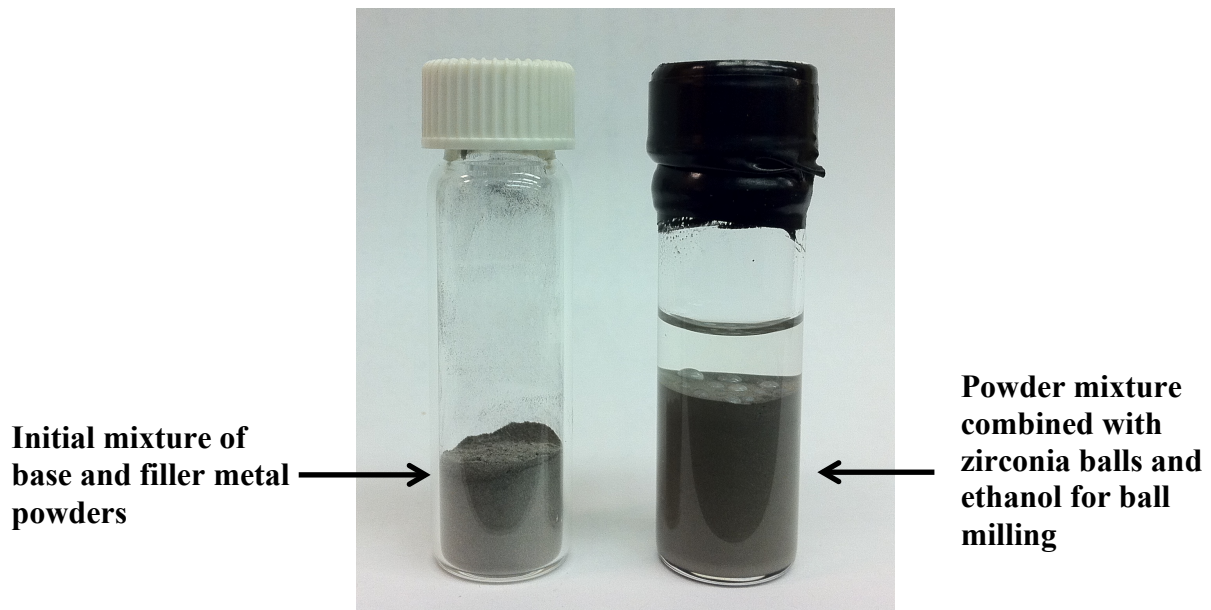
Figure 3.3: Filler metal powder mixtures after initial powder mixing and prior to wet ball-milling.

Figure 3.4 shows a dried, fully-mixed powder after wet ball-milling. Wet ball-milling of powder mixtures is advantageous in that an even distribution increases the surface area of contacting powder particles, which promotes melting and reduces the time required for subsequent solidification [35]. After milling, the mixture was poured through a strainer to remove the zirconia balls and dried in a fume hood to create fully-mixed powders at each mixing ratio.

Figure 3.4: Filler metal powder mixtures after wet ball-milling, resulting in a fully-mixed combination of base and filler metal powders.

Prior to applying the filler metal paste to a notch, a refractory liquid called a "bond stop" was applied to the top and side surfaces of the samples. The purpose of this liquid is to dry on the surface and help to keep most of the molten filler metal inside the notch by preventing the wetting of the coated surfaces.

The filler metal powder mixture was made into a paste by combining the powders with a liquid binder, which evaporates from the paste upon heating. This is again a mixture based on weight-%. Typically, the amount of binder used for a paste is between 11 and 14% of the total paste weight, and the binder is generally added to the powders to prevent clumping [29]. The pastes were mixed in a petri dish and applied to the notch using a small steel spatula. Figure 3.5 shows a notch coated with bond stop, filled with paste, and ready to be repaired.

Filler Material Paste
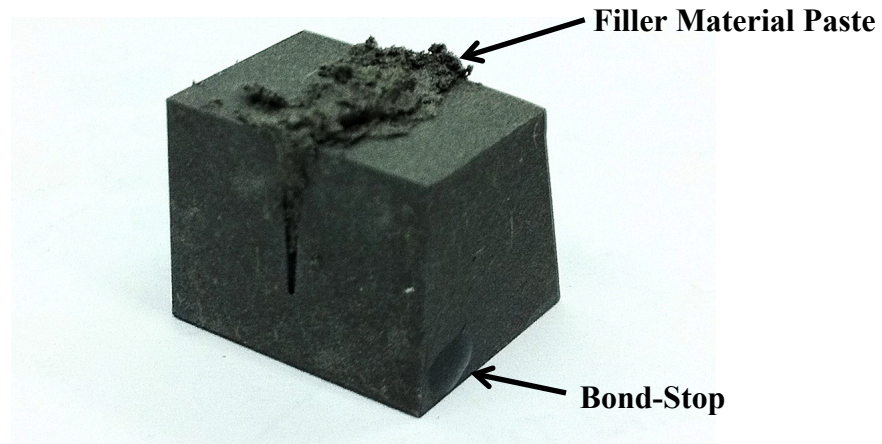
Bond-Stop

Figure 3.5: A notched coupon of GTD111 prior to the diffusion brazing repair process, after application of bond-stop to the surfaces and filler metal paste to the notch.

3.5.2 Brazing Process

Activated Diffusion Brazing was carried out in a Vac Aero VAH-1220HV vacuum furnace. This furnace, shown in Figure 3.6, has a hot zone 12" wide, 12" tall, and 20" in depth. Although this study focuses only on small test coupons, this furnace can hold full service-run components. The heating schedule for the activated diffusion brazing repair process in all preliminary bonding trials can be seen in Figure 3.7. Brazing was conducted at a maximum temperature of 1220°C, for a holding time of 65 minutes.
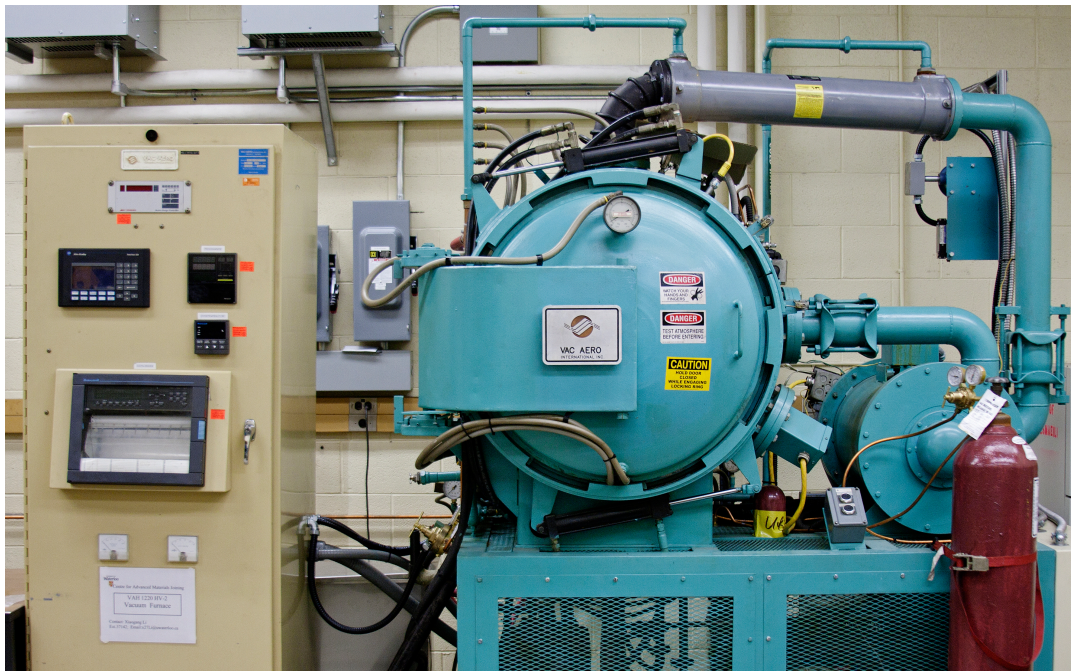
Figure 3.6: Vac Aero VAH-1220HV vacuum furnace.
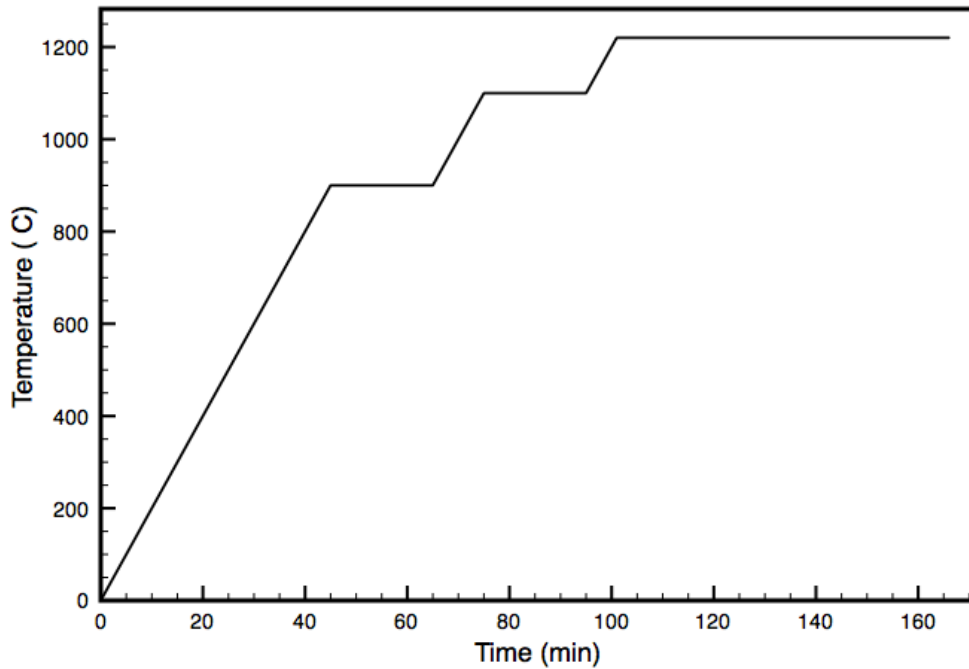
Figure 3.7: The heating schedule employed for the preliminary diffusion brazing repair trials.

The heating schedule was chosen to maximize the vacuum level within the furnace at all times and to reduce thermal stresses on the component during the repair process. Heating was conducted in stages separated by holding, or "soaking," at intermediate temperatures. As heat is applied to the hot zone of a vacuum furnace, moisture trapped on the furnace walls – specifically condensed water vapour from when the furnace door was opened – is vaporized and needs to be purged from the system, at which time the vacuum process is halted. To reduce this "outgassing" effect [36], soaking stages were employed, where holding at a constant temperature helps to recover most or all of the vacuum level lost during the heating stages. This way, by the time the bonding temperature is reached, the furnace has potentially achieved an optimal level of vacuum, in order to reduce or eliminate oxidation on the component or in the filler metal. A holding time of 65 minutes at the bonding temperature of 1220°C was selected as the starting point for the preliminary brazing tests. Finally, slow furnace cooling was employed to minimize thermal stresses in the braze repair, which will in turn minimize the likelihood of cracking within the repaired region.

39

3.6 Grinding and Etching

All samples to be analyzed were ground to a final stage of 1200-grit SiC paper and rinsed with water and ethanol. Samples were not mounted, so that both cross-sectional and surface analysis could be performed. Etching was only necessary for analysis via optical microscopy. Marble's reagent [40] was chosen as the etchant, as it reveals the depletion of the gamma prime phase from the microstructure. Marble's reagent was prepared by adding 10 g H_2SO_4-$5H_2O$ and 50 mL HCl to 50 mL distilled water, and etching was achieved by immersing the samples in the etchant for approximately 45 seconds. Etched samples were then rinsed with water and ethanol.

3.7 Microscopic Analysis

Optical Microscopy was performed using an Olympus BX15M metallurgical microscope, on samples etched with Marble's reagent to determine the effects of oxidation, cleaning, and bonding on gamma prime depletion. Scanning Electron Microscopy was performed on a LEO 440 SEM equipped with a Quartz Xone EDX detector. Coupled with element mapping, SEM-EDX analysis was performed on all samples to evaluate the chemical effects of the oxidation, cleaning, and brazing processes on oxidized, cleaned, and bonded samples of GTD111. Rigaku Micro-Area X-ray Diffraction was used to analyze the types of oxide present on the surface of oxidized samples.

In the following chapter, samples oxidized between one and 452 hours will be analyzed via SEM-EDX and element mapping to determine the order of oxide growth and the oxide structure and chemistry observed in GTD111 after different oxidation times.

Chapter 4 Oxidation Behaviour of GTD111

This work described in this chapter was performed to determine the high-temperature oxidation behaviour of GTD111 in dry air. The objective of this chapter is to understand how oxide scales form on this particular alloy, and how the chemistry and structure of such scales depend on oxidation time.

4.1 Results

4.1.1 Gamma Prime Depletion Analysis via Optical Microscopy

Oxidized samples were immersed in Marble's reagent for approximately 40 seconds to reveal the extent of gamma prime phase depletion after each oxidation time. The gamma prime precipitate phase is a major strengthening phase in GTD111. Areas depleted of the gamma prime phase appear very bright after immersion in Marble's reagent. Figure 4.1 below shows oxidized and unoxidized samples etched using Marble's reagent.

(a) (b)
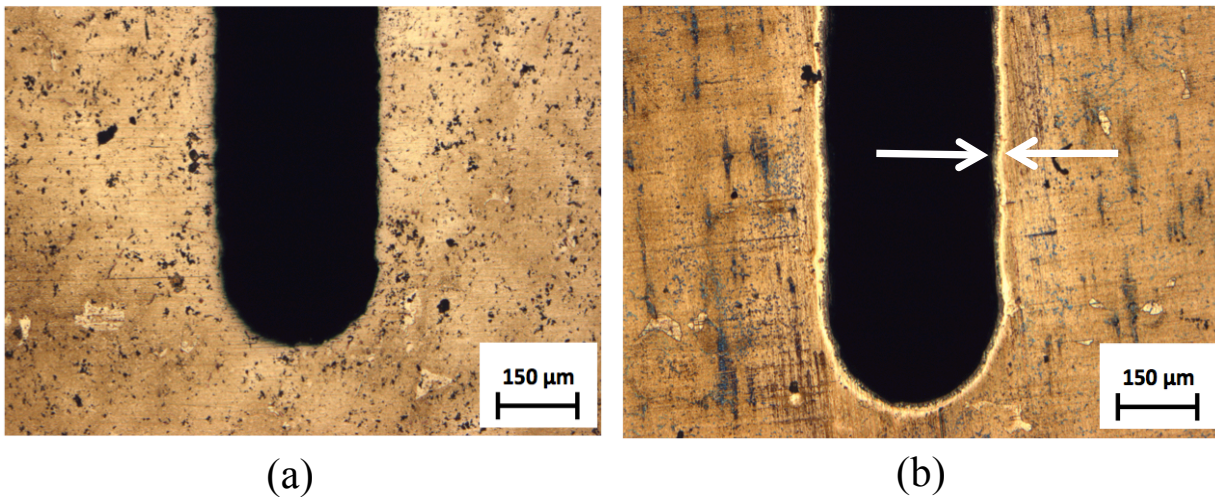
Figure 4.1: Optical micrographs at 5X magnification of notched samples after etching with Marble's reagent for 45 seconds shows that an unoxidized sample (a) exhibited no gamma prime phase depletion, whereas a sample oxidized for 308 hours (b) showed clear evidence of such depletion, indicated by the bright halo around the notch, indicated by the white arrows.

The unoxidized sample in Figure 4.1 a exhibited no evidence of depletion, as the etchant had the same effect on the entire cross-section. However, the oxidized sample was depleted of the gamma prime phase near the edges of the notch, as indicated by the bright region nearest the surface in Figure 4.1 b.

The extent of gamma prime depletion was measured on each oxidized sample. Five measurements were taken from the tip of each notch, as in Figure 4.2 below. It is important to note that the measurements were taken only within the bright region, as can be seen in Figure 4.2, where the measurement lines end at the dark scale beyond the bright region. The results of this analysis were plotted in Figure 4.3.
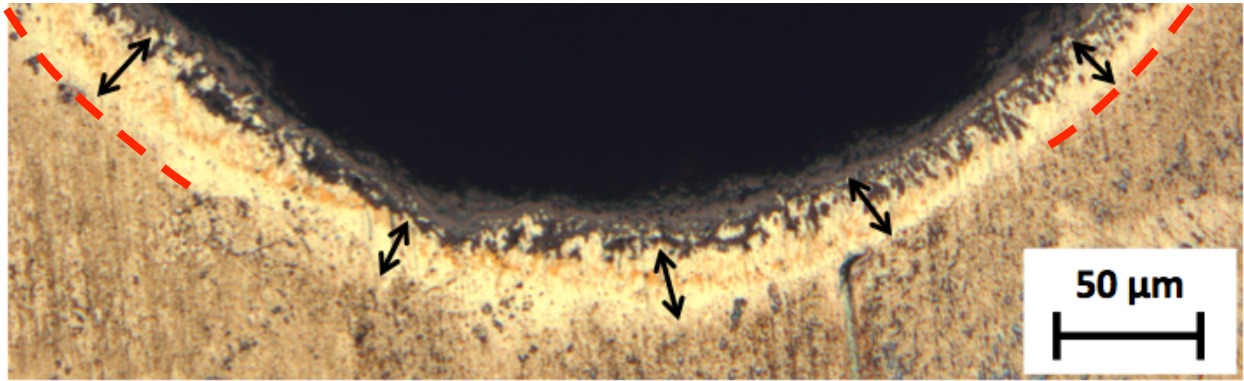
Figure 4.2: Optical micrograph showing the measurements taken of the gamma prime depletion of a sample oxidized for 308 hours.
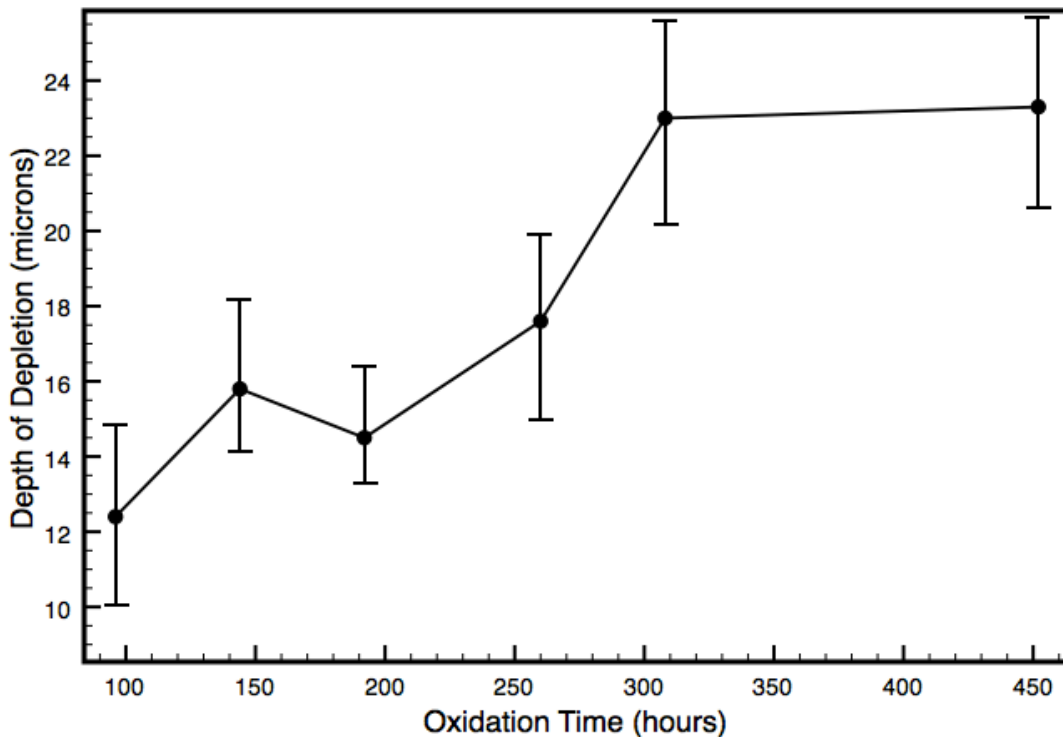
Figure 4.3: Depth of gamma prime depletion observed with respect to oxidation time.

The gamma prime phase depletion was observed to increase, in general, until 308 hours. Very little increase was observed between 308 and 452 hours.

4.1.2 Differences in Oxide Structure Observed Using Back-Scattered Electron Imaging

Back-Scattered Electron (BSE) images at 20 keV were taken at 100 and 500X magnifications to show the differences in appearance of samples that had and had not been oxidized, and to evaluate any immediate differences in the structures of oxides formed after different durations. Figure 4.8 below shows BSE images of oxidized and unoxidized samples.

(a)   (b)
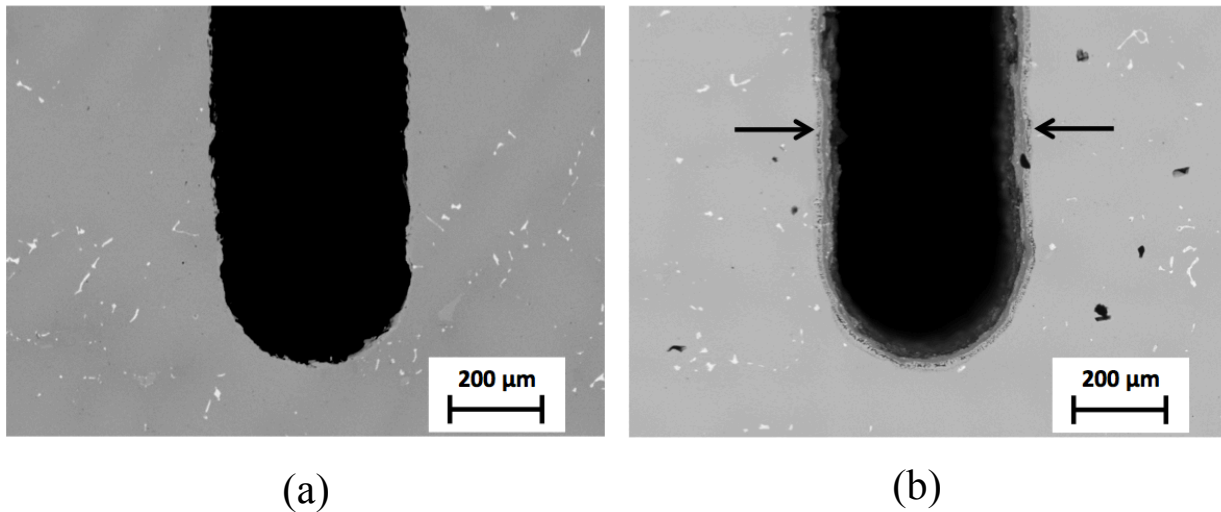
Figure 4.4: Back-scattered electron images of: (a) an unoxidized notch in GTD111 and (b) a notch in GTD111 oxidized for 308 hours.

A clear difference between the oxidized and unoxidized samples was observed, although only within the immediate subsurface. Back-scattered electron images were taken at 500X magnification in order to differentiate between the oxidized regions after different oxidation times. The BSE images for each sample, from 1 hour to 452 hours, are shown in Figures 4.5 and 4.6. The low oxidation times showed the onset of oxidation. The one-hour sample shown in Figure 4.5 a exhibited a normal notch surface, with no obvious signs of oxidation, but the sample oxidized for four hours (see Figure 4.5 b) showed the formation of initial oxides at the surface. It can therefore be stated that the GTD111 surface began to show clear signs of oxidation at some time between one and four hours at 900°C. At such times, however, the extent of oxidation observed was quite low, and there was not much of a distinct oxidized structure.
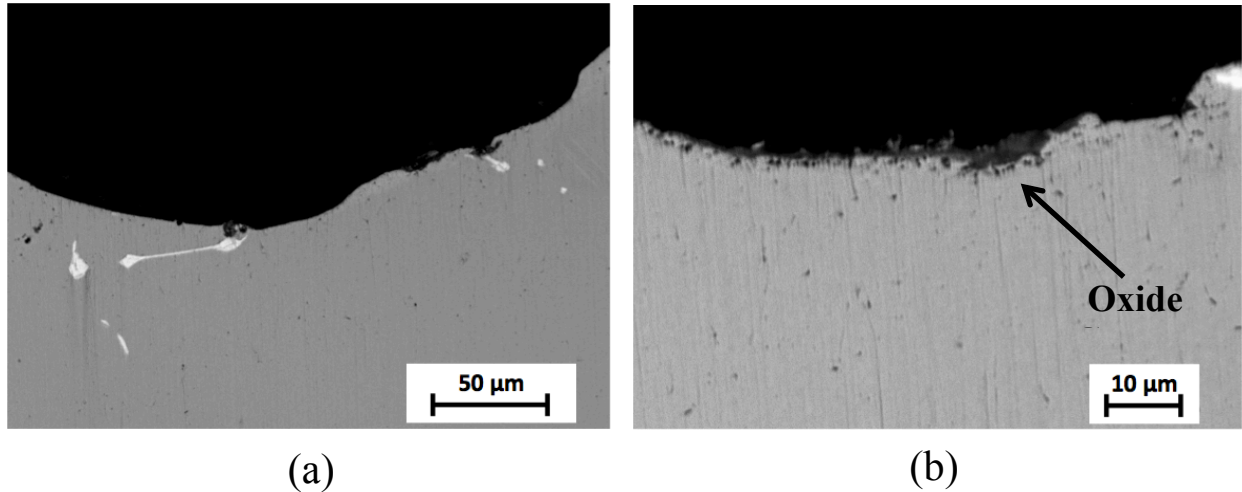
Figure 4.5: A notch: (a) oxidized for 1 hour at 900°C exhibited no clear signs of oxidation, whereas (b) clear evidence of oxidation was visible after 4 hours of oxidation.

Figure 4.6 shows BSE images of specimens that had been oxidized from 96 to 452 hours. Very distinct regions of oxide growth were observed. For example, Figure 4.6 b shows a sample oxidized for 144 hours. Dark, circular phases were found within the surface, above which was a white line, followed by a dark band, above which was the surface of the cross-section. This general pattern was observed on each oxidized sample, regardless of time, after 96 hours of oxidation at 900°C. Although the pattern remained very similar for all oxidation times, it is important to note minor differences that were observed, mainly in the thickness of the different regions at different times.
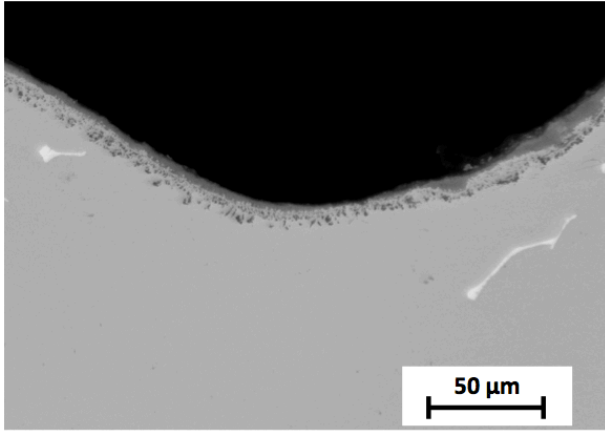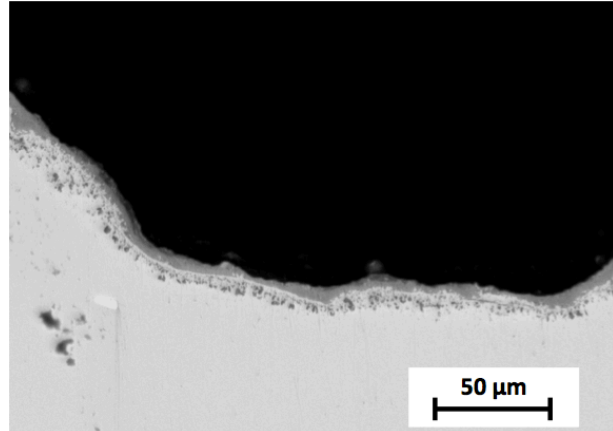
(a) Oxidized for 96 hours   (b) Oxidized for 144 Hours
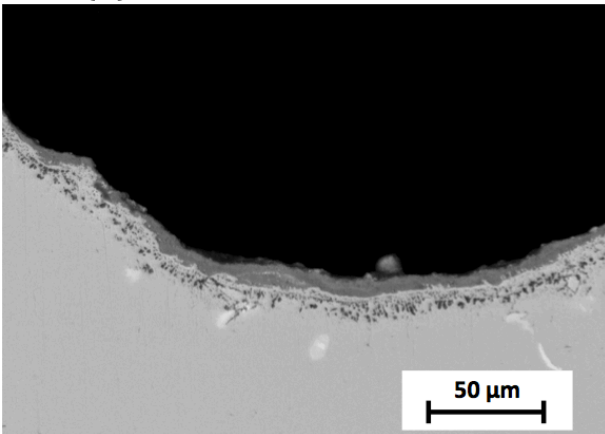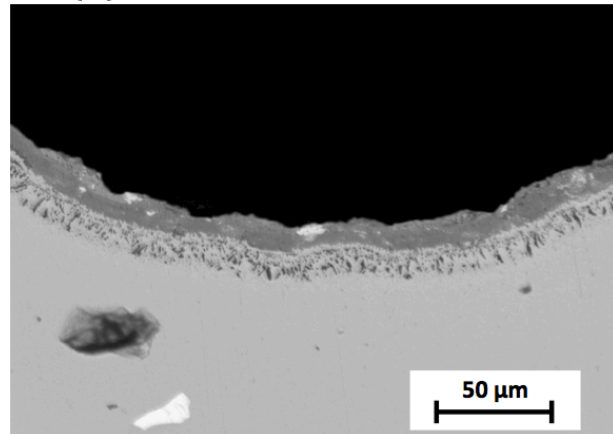
(c) Oxidized for 192 hours   (d) Oxidized for 260 Hours
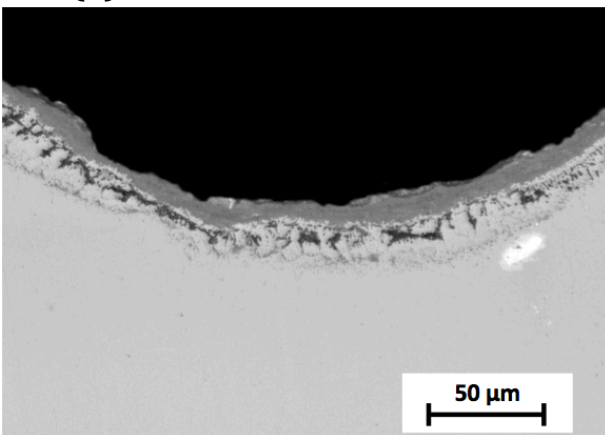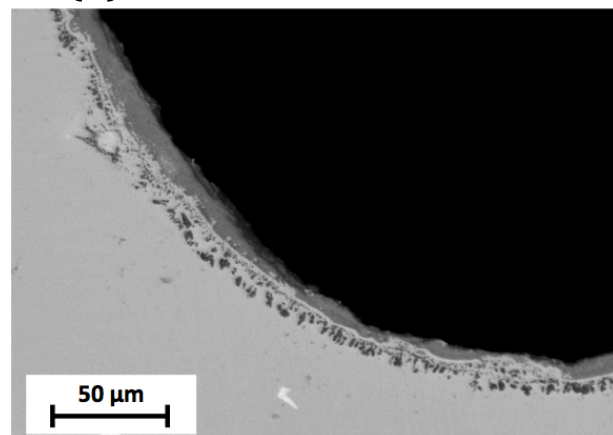
(e) Oxidized for 308 hours   (f) Oxidized for 452 Hours

Figure 4.6: BSE images of samples oxidized for (a) 96, (b) 144, (c) 192, (d) 260, (e) 308, and (f) 452 hours showed slight differences in overall oxide thickness.

4.1.3 – Elemental Distribution Within Oxide the Structure

In order to further understand the oxidation behaviour of GTD111, it was necessary to perform chemical analysis on the cross-section of each sample. Firstly, qualitative chemical analysis via element mapping using the EDX on the SEM was performed to provide a visual representation of the chemical distribution within the oxidized structure at each oxidation time. Element maps of oxygen, nickel, aluminum, tungsten-tantalum, titanium, and chromium were created for all six oxidized samples. It should be noted that tungsten and tantalum have been grouped together as one element (tungsten-tantalum) for the remainder of the chemical analysis. Tungsten and tantalum have been added to the GTD111 in similar concentrations and it was difficult for the EDX detector used to differentiate between the two elements, due to their overlapping M-alpha peaks in the spectra. In order to differentiate between tungsten and tantalum, the L-alpha peaks required excitation, but a higher energy (30 keV) was required to do so. Also, using the L-alpha peaks for element mapping would have required very long acquisition times, and so the M-alpha peaks for W and Ta were combined for the remainder of the elemental analysis.

Element maps for nickel K-alpha (red), oxygen (light blue), aluminum K-alpha (dark blue), tungsten-tantalum M-alpha (purple), chromium K-alpha (green), and titanium K-alpha (yellow) were made for each oxidation time, and have been presented in Figures 4.7 through 4.13 below. As would be expected, the baseline sample (see Figure 4.7) – which had not been oxidized – showed no concentrations of oxygen or any other element, with the exception of the bright heavy-element phases (high in W-Ta-Ti and high in Cr-Ti) within the bulk of the sample.

Element maps for the sample oxidized for 1 hour are shown in Figure 4.8. After one hour of oxidation at 900°C, the formation of the first oxide compounds were observed, as indicated by the concentrated region on the oxygen element map in Figure 4.8. The Ti element map showed concentrations in this region, and so the first-formed oxide was that of titanium.

Element maps for the sample oxidized for four hours can be seen in Figure 4.9. After 4 hours of oxidation, the initial formation of distinct regions was observed, as bands of concentration were seen in the aluminum and chromium maps at this point. At this early stage in the oxidation process, distinct oxide formations were not observed, as the oxides of Al, Ti, Ni, and Cr cannot be easily differentiated on the sample oxidized for four hours.
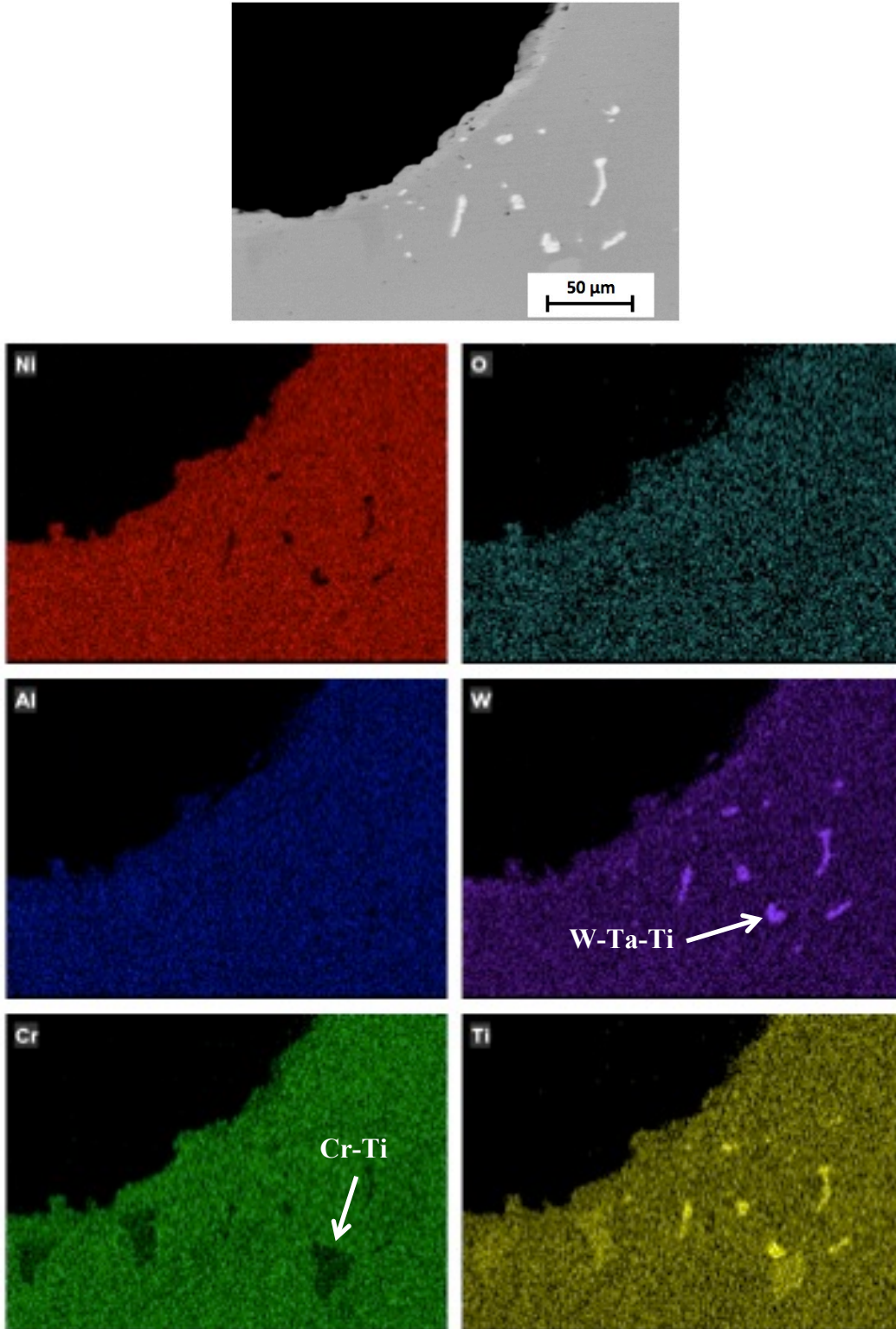
Figure 4.7: SEM photomicrographs of an unoxidized sample: (a) BSE image and (b) element maps of the same area of the sample.

Element maps for the 96-hour sample are shown in Figure 4.10. The sample oxidized for 96 hours exhibited the formation of much more distinct regions of elemental concentration than was observed on previous samples. The oxidation process had caused the oxides of nickel, aluminum, chromium, and titanium to form at different levels within the sample. Small amounts of Ni were observed above the surface, indicated by the few red dots seen above the surface on the nickel element map. Titanium particles formed mostly above and within the very top portion of the surface, whereas chromium concentrations were observed below this titanium region. The concentration of Cr particles in the Cr element map corresponded to the region very low in Ti particles on the Ti element map. Even at 96 hours, the chromium oxide formed was found to be quite dense. The dark blocky regions deepest within the surface of the BSE image were be associated with concentrations on the Al element map, indicating that the deepest-formed oxide was rich in aluminum.

Element mapping results for the 144-hour sample are shown in Figure 4.11. As was observed in the 96-hour sample, the Ti particles seemed to concentrate in two regions. The upper Ti concentrations displayed inconsistent widths, and were associated with the regions rich in Ni, whereas the lower Ti concentrations were much more consistent, thinner bands associated with W-Ta-rich regions, as shown by arrows on the 144-hour sample element maps.

Element maps for the 192-hour sample can be seen in Figure 4.12. The elemental distribution at 192 hours was found to be very similar to that observed at 144 hours, but with a thin external region rich in Ni and Ti above the Cr-rich oxide layer, as well as a small concentration of Ti particles observed below the Al-rich region as indicated by the arrows on the BSE image and Ti element map. This region was not found to be associated with oxygen, as concentrations on the oxygen element map did not extend as far into the sample as the Ti concentrations.

Figure 4.8: SEM photomicrographs of a sample oxidized for 1 hour at 900°C: (a) BSE image and (b) element maps of the same area of the sample.
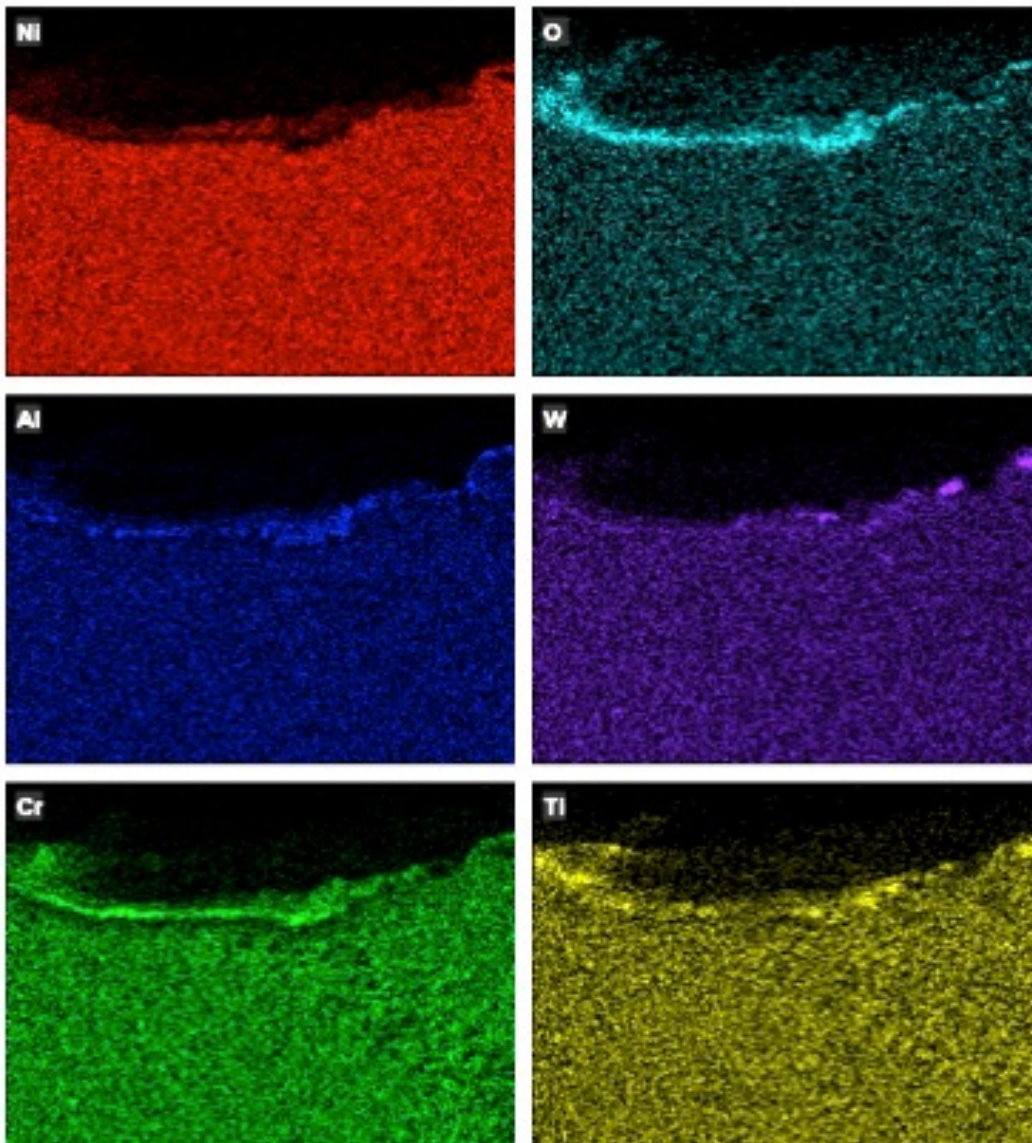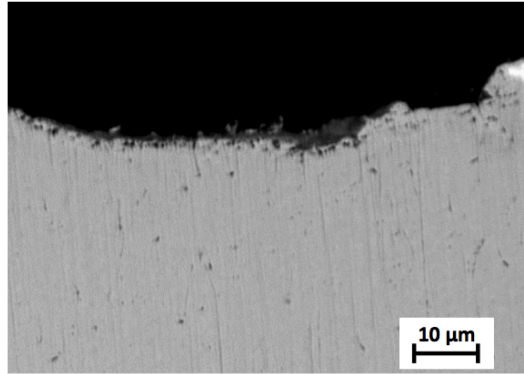
Figure 4.9: SEM photomicrographs of a sample oxidized for 4 hours at 900°C: (a) BSE image and (b) element maps of the same area of the sample.
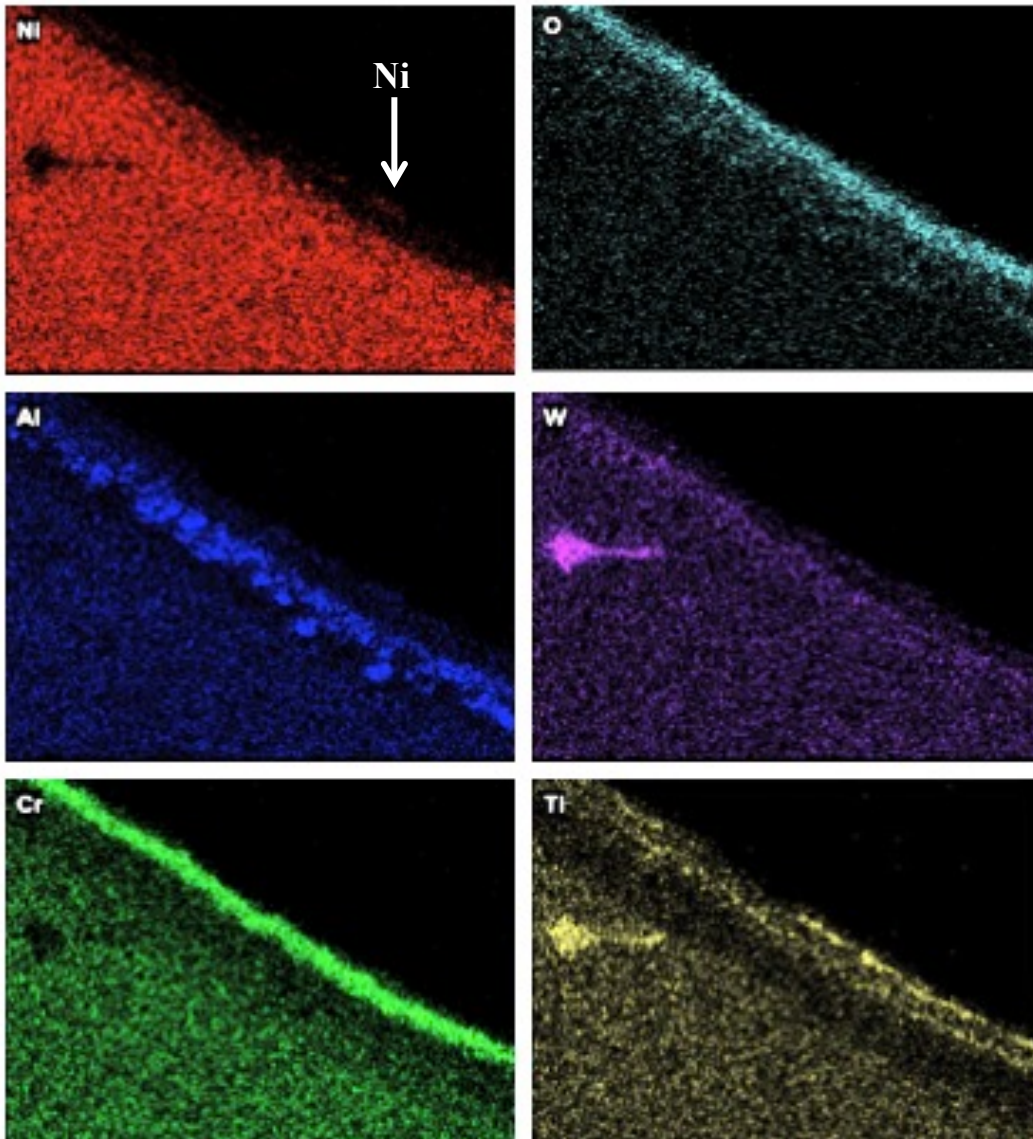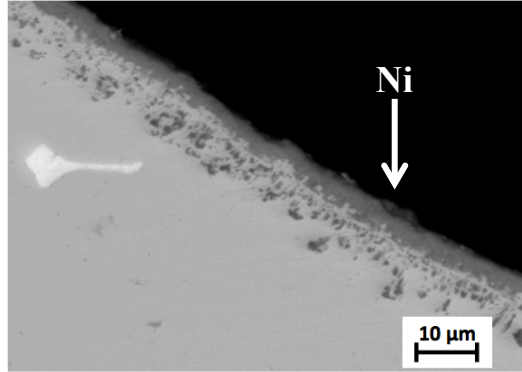
Figure 4.10: SEM photomicrographs of a sample oxidized for 96 hours at 900°C: (a) BSE image and (b) element maps of the same area of the sample.
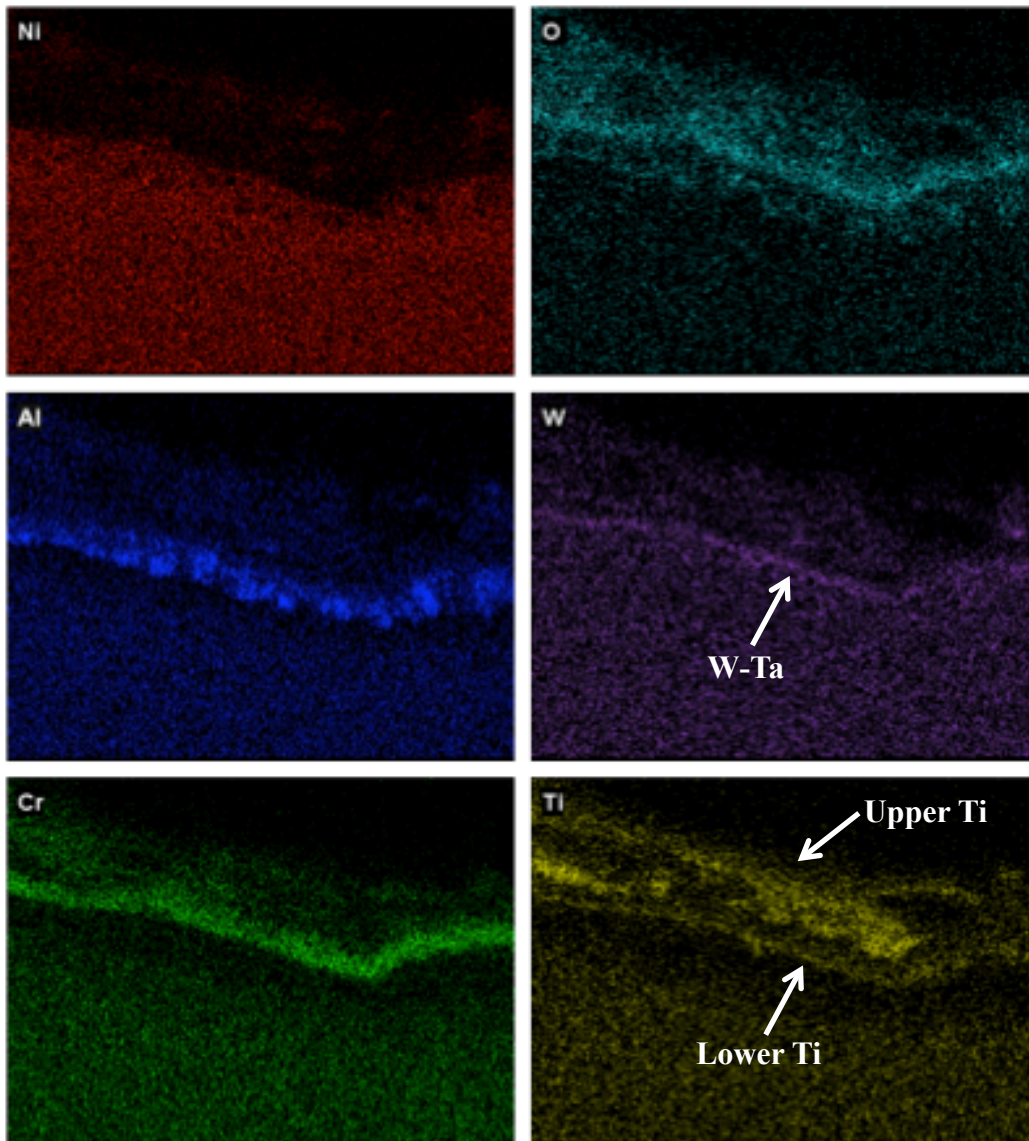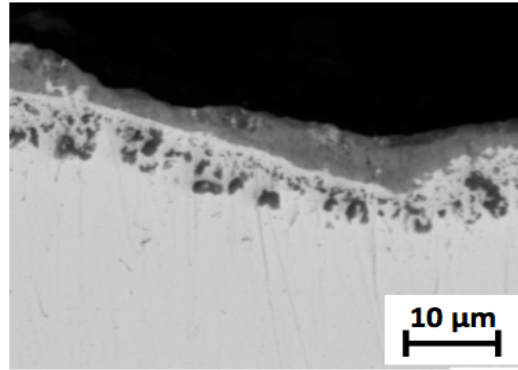
Figure 4.11: SEM photomicrographs of a sample oxidized for 144 hours at 900°C: (a) BSE image and (b) element maps of the same area of the sample.

Element maps for the sample oxidized for 260 hours are shown in Figure 4.13. The sample oxidized for 260 hours exhibited a fairly thick, inconsistent external region rich in Ni and Ti, which had formed above the chromium oxide layer. The Ti particles that were observed below the Al-rich oxide regions at 192 hours were not seen on this sample, possibly indicating their migration toward the surface of the sample to react with oxygen.

Element maps for the 308-hour sample are shown in Figure 4.14. The structures of samples oxidized for 260 and 308 hours (Figures 4.12 and 4.13, respectively) displayed very similar characteristics, except for the apparent increase in density of the regions rich in Al and the very distinct band of Ti particles – again not associated with oxygen – below the Al-rich regions.

Figure 4.15 shows the element maps for the sample oxidized for 452 hours. The element maps for the sample oxidized for 452 hours once again showed very thin, but inconsistent regions rich in Ni and Ti atop the sample's surface, and increased densities of the Cr- and Al-rich regions below the surface. The Al-rich region was observed to be discontinuous – unlike the continuous Cr band observed – across the entire range of oxidation time. The region high in unoxidized Ti particles observed below the Al-rich region at 308 hours was not observed on the sample oxidized for 452 hours.

All samples oxidized for 96 hours or more exhibited very similar structures, wherein inconsistent outermost regions high in Ni (at some oxidation times) and Ti were located atop a very dense band high in Cr. Following this band was a thin, continuous band showing concentrations of W-Ta and to lesser extents Ni and Ti. In all cases, the deepest-forming region associated with oxygen was the blocky, discontinuous region high in aluminum. It is important to note that times of 192 and 308 hours showed high levels of titanium in their element maps below the Al-rich oxide regions (see Figures 4.12 and 4.14), but this region was clearly not associated with oxygen, as was apparent by the oxygen element maps, which showed concentrations only as deep as the aluminum-rich regions.
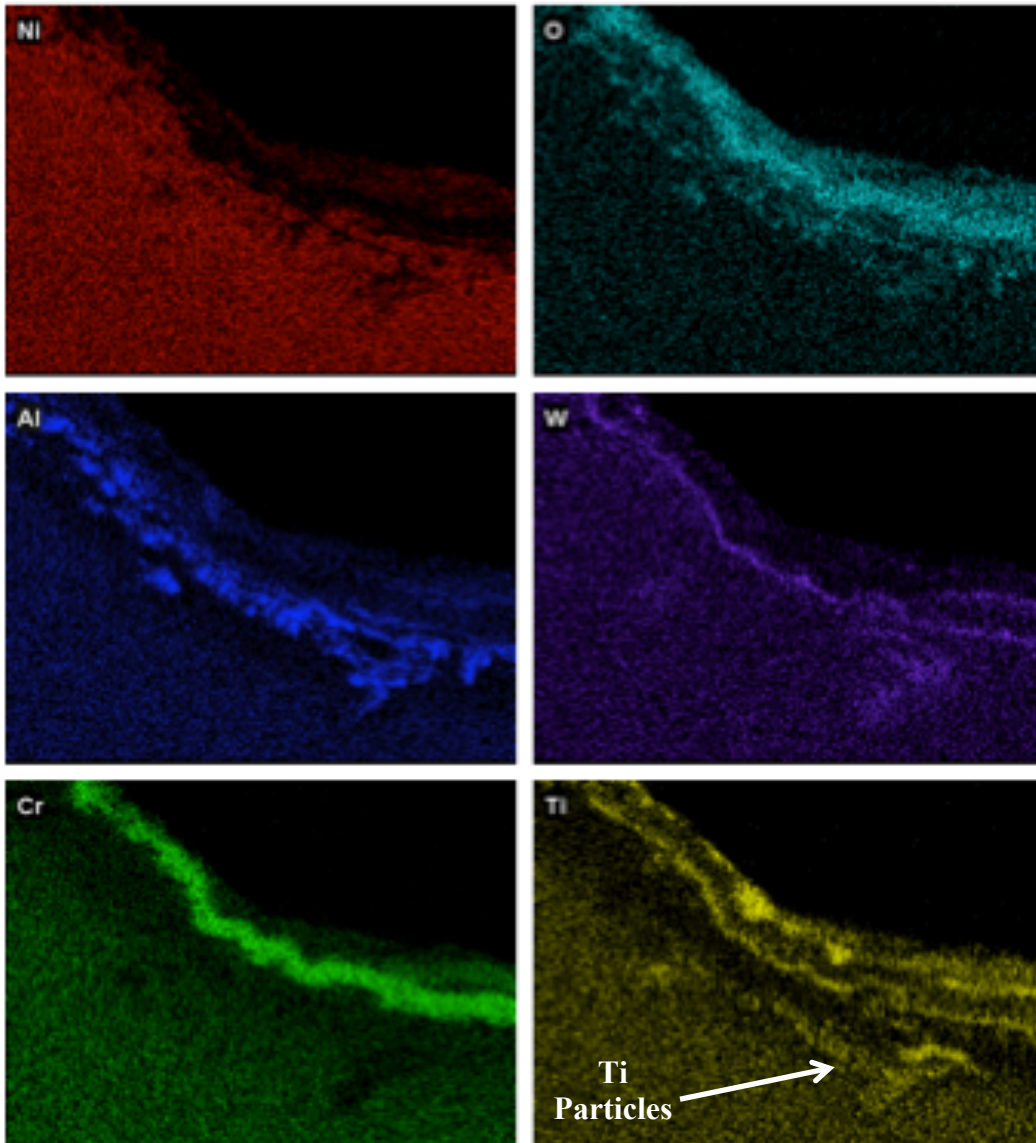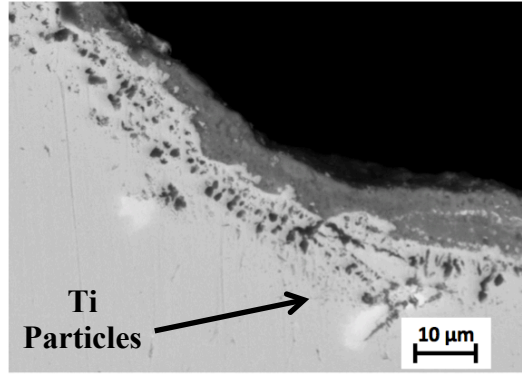
Figure 4.12: SEM photomicrographs of a sample oxidized for 192 hours at 900°C: (a) BSE image and (b) element maps of the same area of the sample.
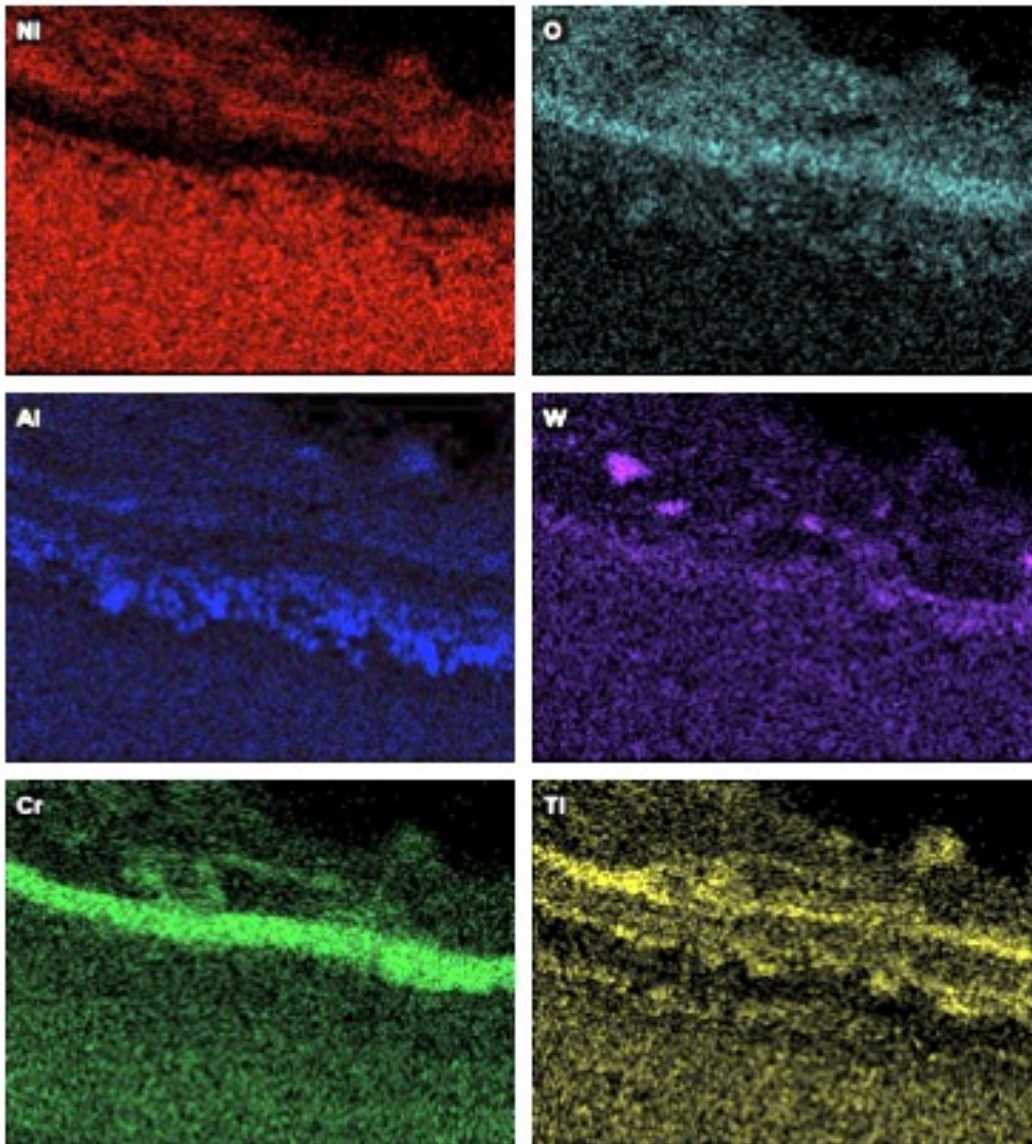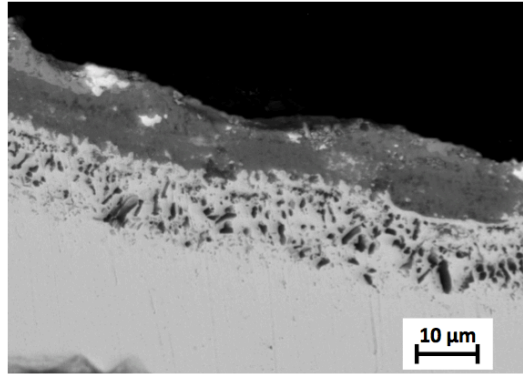
Figure 4.13: SEM photomicrographs of a sample oxidized for 260 hours at 900°C: (a) BSE image and (b) element maps of the same area of the sample.
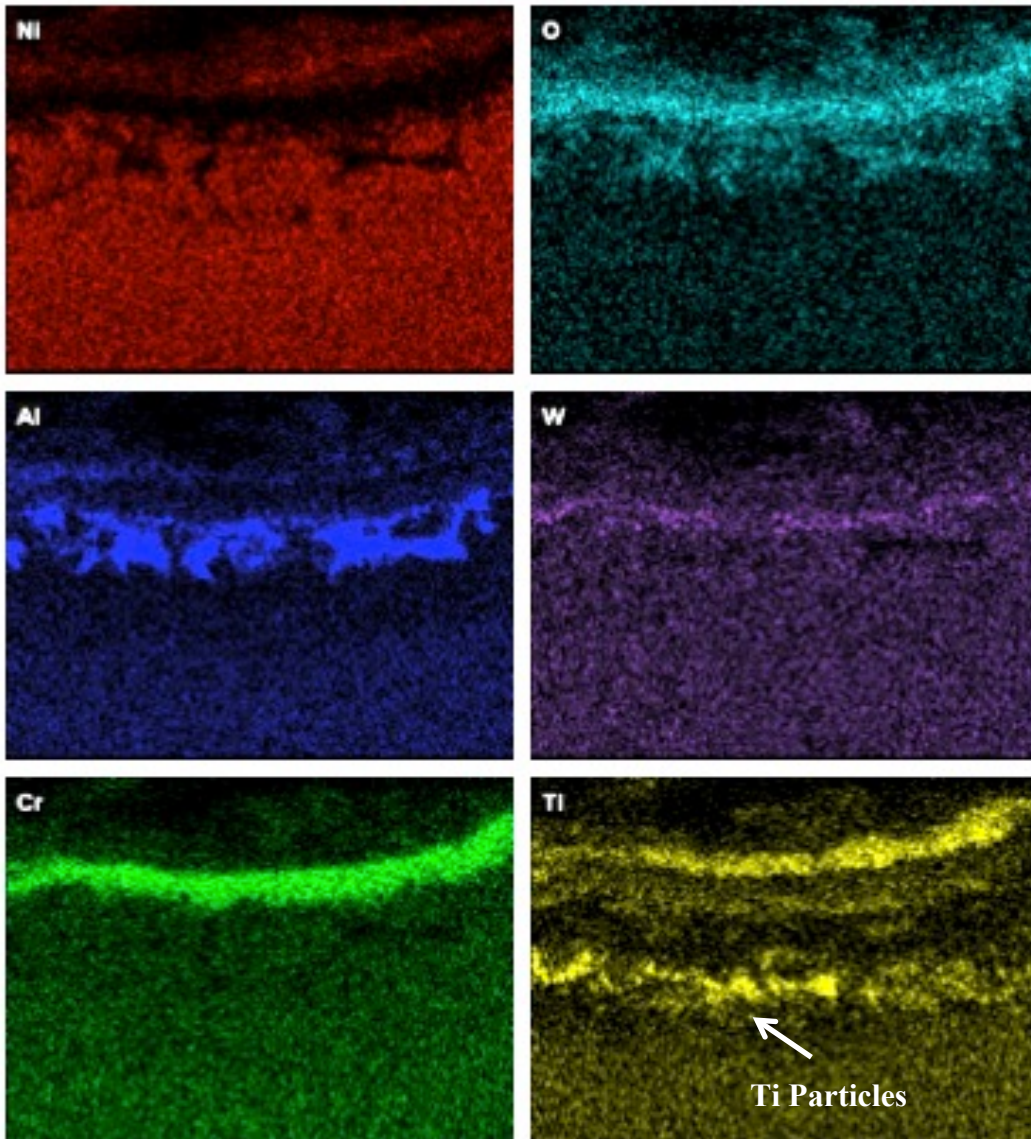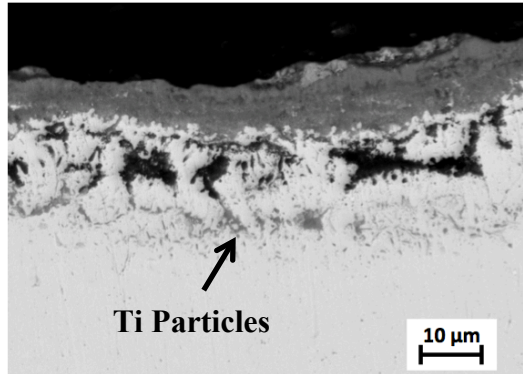
Figure 4.14: SEM photomicrographs of a sample oxidized for 308 hours at 900°C: (a) BSE image and (b) element maps of the same area of the sample.
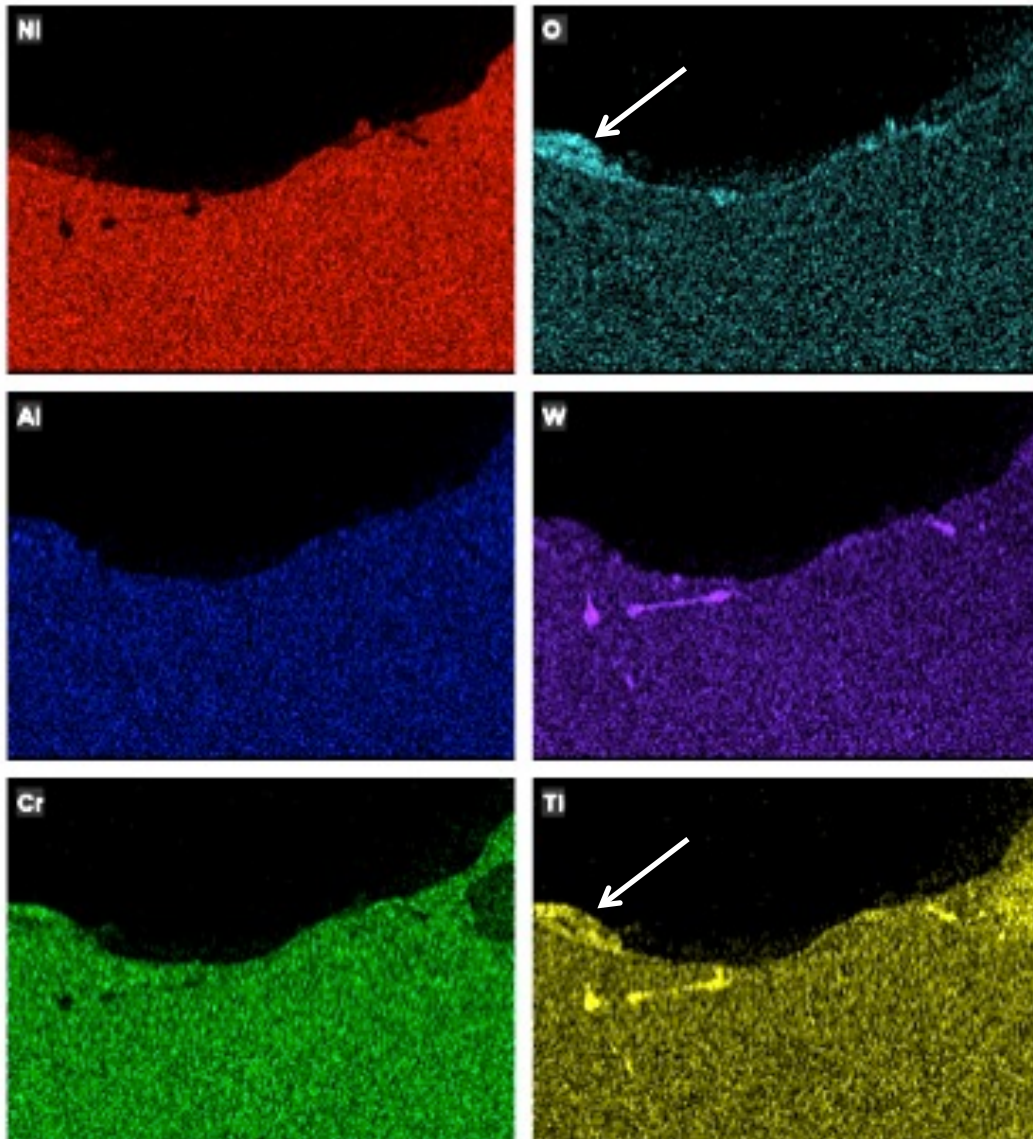
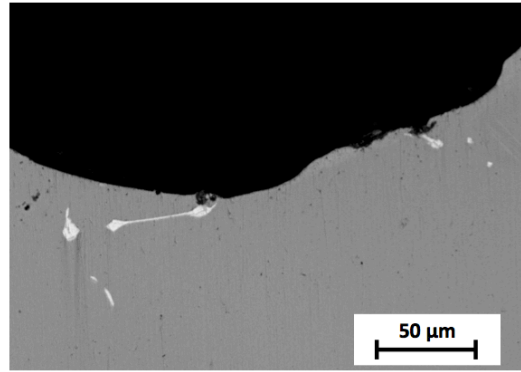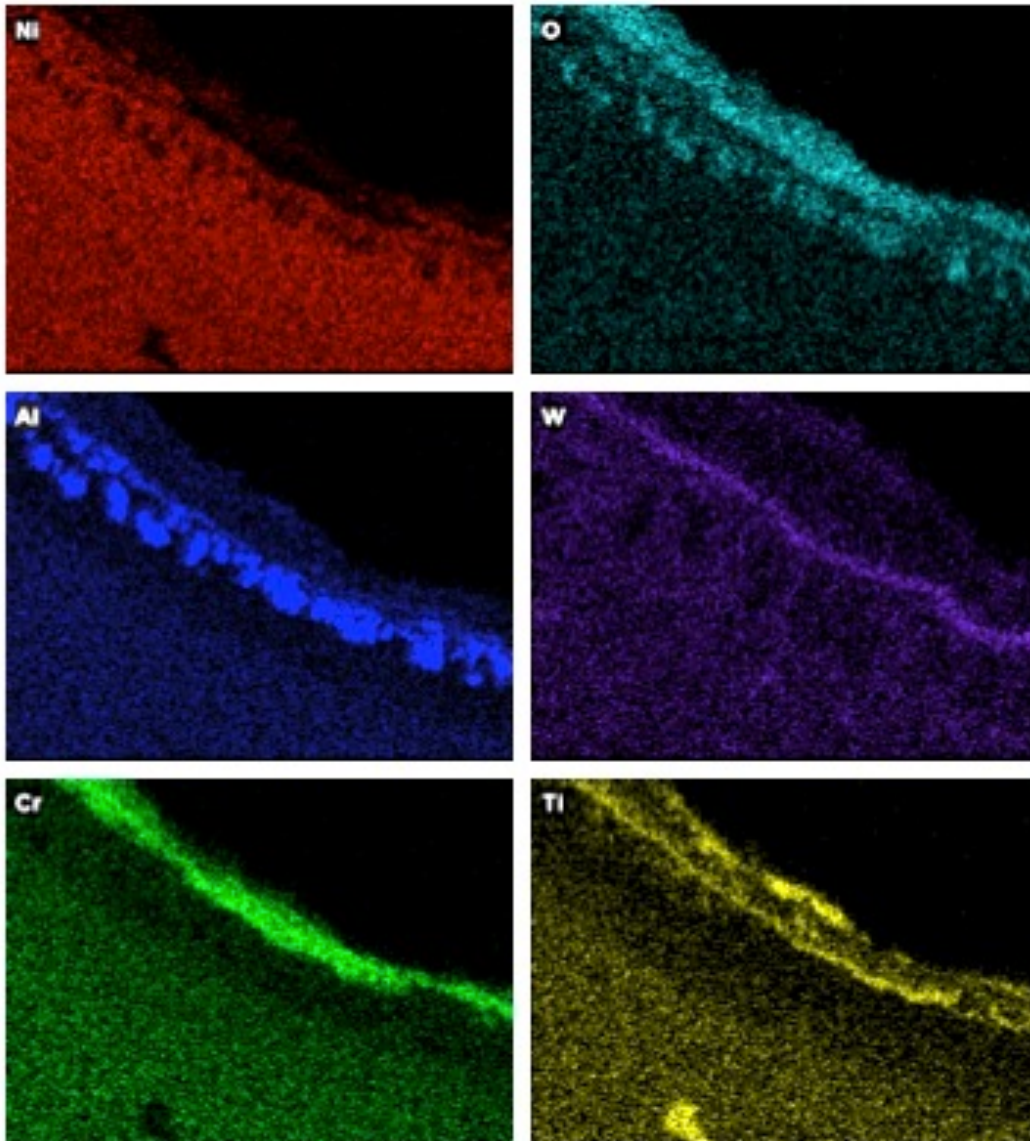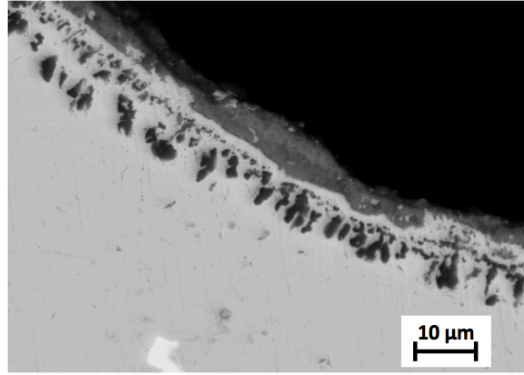**Figure 4.15:** SEM photomicrographs of a sample oxidized for 452 hours at 900°C: (a) BSE image and (b) element maps of the same area of the sample.

4.1.4 Element Map Overlays to Show Interaction of Main Oxidizing Alloying Elements

The software within the particular SEM used was capable of taking multiple element maps from a sample to create composite images showing the distribution of many elements in one image. This function was used to overlay the element maps of the main oxidizing elements of aluminum (blue), titanium (yellow), chromium (green), and tungsten-tantalum (red) for each oxidation time. These maps can be seen below in Figure 4.16. It should be noted that oxygen and nickel were removed from the overlays because they were essentially constant within the oxidized regions of each sample, and their presence in the overlays caused the distinct regions to appear much less obvious.

Element map overlays were a great tool for showing the distribution and interaction of various elements within the oxidized samples, and to show that there were some interesting changes in chemistry and structure with increasing oxidation time. For example, there seemed to be an increasing concentration of tungsten-tantalum (red) above the dark blue aluminum region from 96 to 192 hours of oxidation, and then this region began to increase in titanium (yellow) until 452 hours. Also, the exterior regions, which were found to be rich in titanium, showed a large variation in thickness and presence with respect to time. The green Cr-rich region appeared to be a very dense, continuous oxide layer, while the blocky aluminum oxide phases grouped together in a thick, discontinuous region closest to the unoxidized base metal.
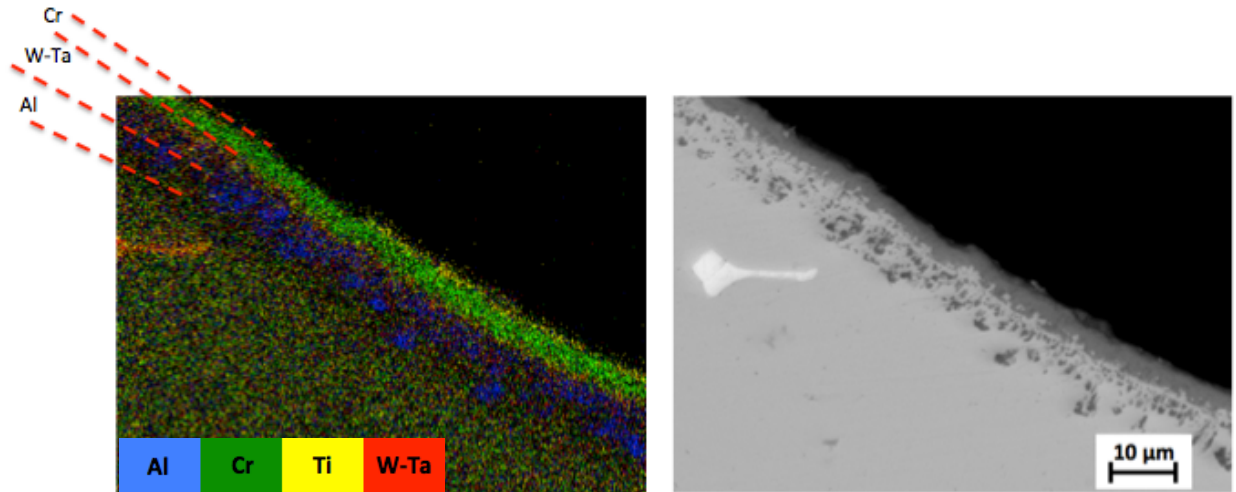
(a) Oxidized for 96 hours
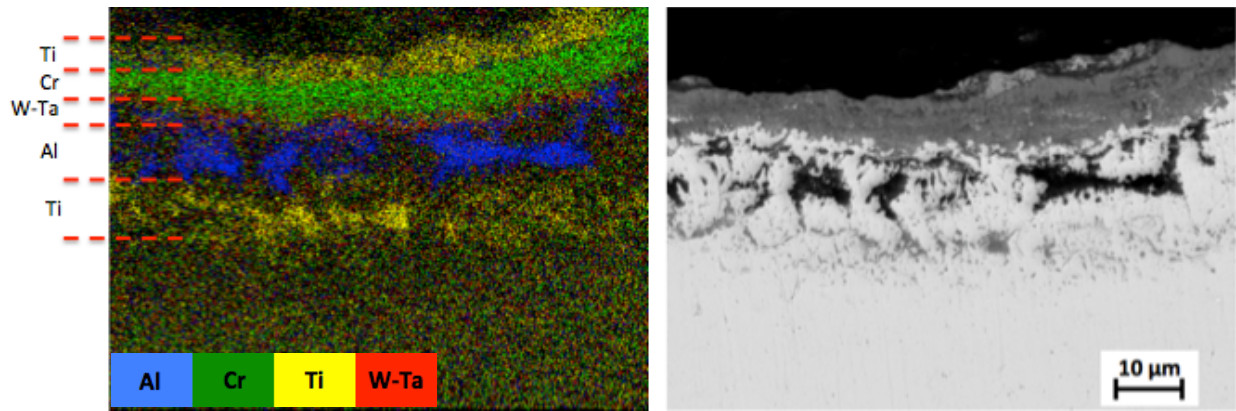
(b) Oxidized for 308 hours
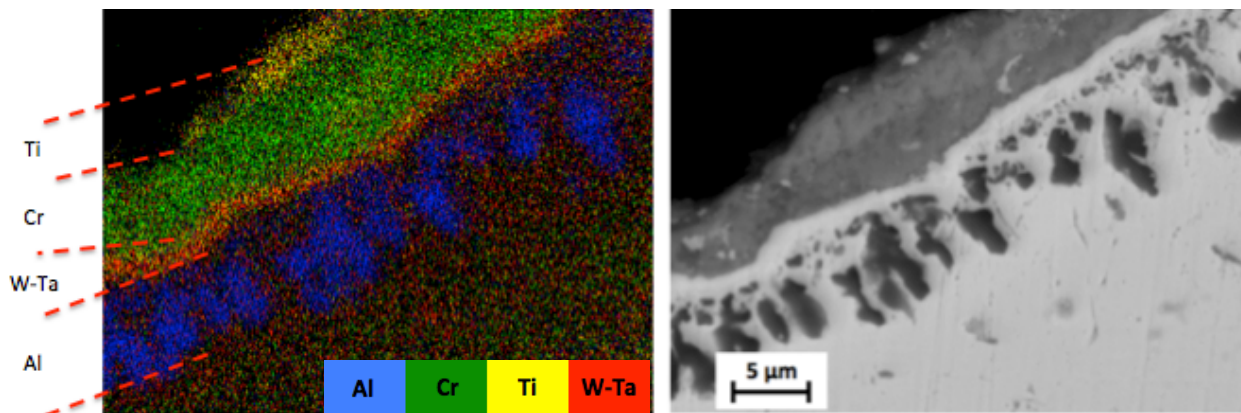
(c) Oxidized for 452 Hours

Figure 4.16: Composite element map overlays showing the distribution of Al (blue), Ti (yellow), Cr (green), and W-Ta (red) after each oxidation time. The distinct regions observed at each time have been indicated.

4.1.5 Energy-Dispersive X-Ray Analysis

Although element mapping provided a visual representation of chemical analysis, it was important to also obtain quantitative data on the chemistry of the apparently distinct regions of growth in order to verify the observations made from the element mapping analysis.

4.1.5.1 Distinct Regions of Formation

Once a visual "map" of the observed oxidation had been established, it was important to focus on each potentially distinct region at a deeper level, in order to verify the differences in chemistry and create a more accurate model of the general oxidation behaviour of GTD111. Below, Figure 4.17 shows a BSE image of the general oxide structure observed over the range of oxidation times above 96 hours. Regions 1 to 7 were observed on all samples, and region 8 was observed only on a few samples. However, this image can be used to summarize the general appearance of oxide scales on GTD111, oxidized in the range of 96 and 452 hours at 900°C.
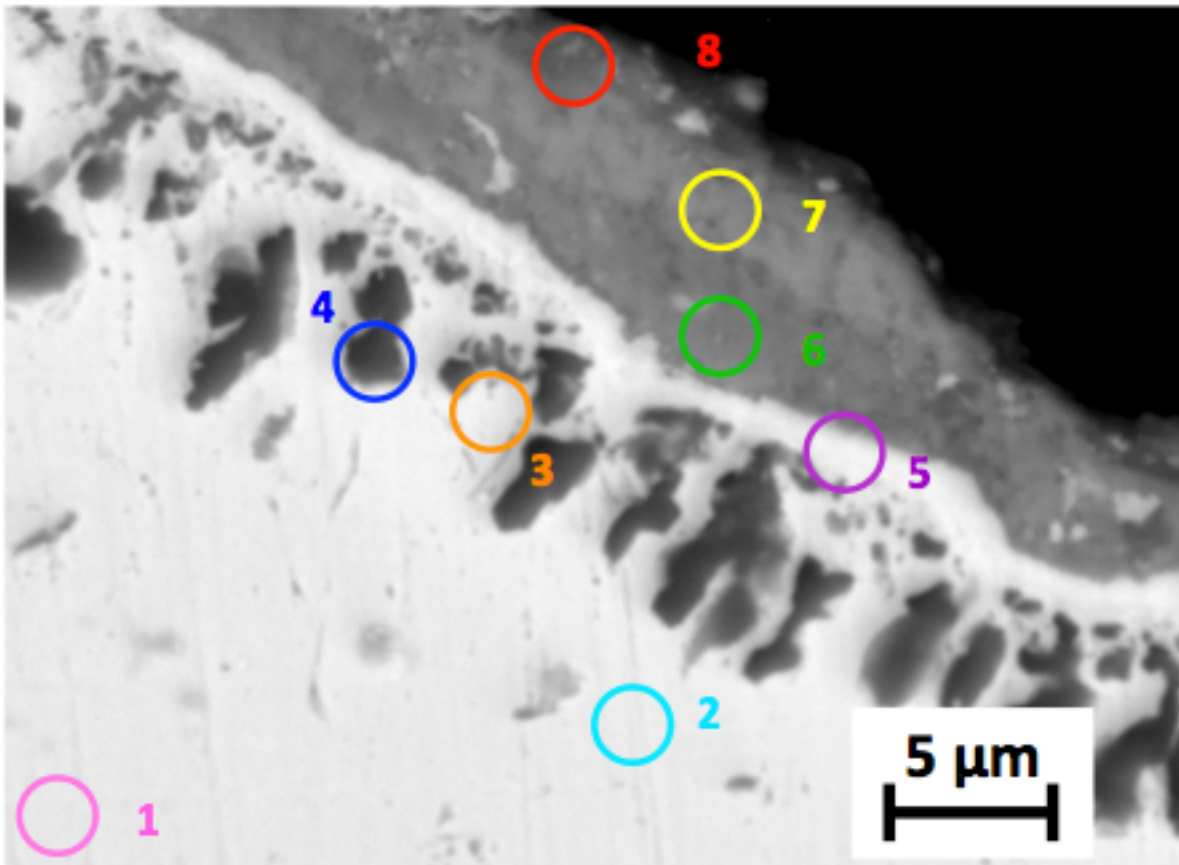
Figure 4.17: BSE image showing the oxide structure observed for most oxidation times, with distinct regions numbered.

4.1.5.2 Distinct Region Chemistry

Energy-dispersive X-ray spectrometry was performed at each potentially distinct region of each sample. A very small region from inside each of the numbered circles in Figure 4.17 was sampled, ensuring that the beam stayed within each distinct region, thus preventing the collection of data from the surrounding regions. EDX analysis provided the semi-quantitative weight-percentage of each element making up a given region. The average concentrations of the alloying elements in each distinct region, across the range of oxidation times, have been summarized in Table 4.1. It is necessary to point out that although the upper and lower depleted regions (regions 2 and 3 from Figure 4.17) were analyzed as different regions, they were very similar in composition. This region of elemental depletion was associated with the gamma prime phase depletion as observed in Section 4.1.1.

Table 4.1: Average concentrations* of the main oxidizing elements present in each distinct region.

Region	Al	Ti	Cr	Ni	W-Ta	O	Description
8	2.1	9.0	6.6	25.3	3.9	27.5	Ni-Ti external
7	2.2	10.4	18.6	16.1	1.6	34.5	Cr-Ti
6	1.2	4.6	47.8	3.1	2.1	39.1	Cr
5	1.7	9.3	7.3	34.6	19.4	20.9	Ni-W-Ta
4	33.7	1.5	2.2	17.3	2.1	40.0	Al
3	1.4	0.4	5.5	69.3	7.5	2.2	Upper Depleted
2	1.7	2.2	8.7	68.0	6.2	0.0	Lower Depleted
1	3.5	4.6	12.2	62.7	6.7	0.0	Base

* All values are given in weight %

Figure 4.18 shows a diagram of the general oxidized structure seen on GTD111 in the range of 96 to 452 hours at 900°C. The data from Table 4.1 was used to create a schematic of the main layers of oxide growth within GTD111 over the range of oxidation times studied, thus verifying the element mapping results. This schematic provides more detail on the oxide structure of GTD111 than has been noted in previous publications. In all cases, the deepest-forming oxide islands were rich in Al, and were surrounded by a region of depleted, unoxidized base metal reaching even deeper into the bulk material. Observed above this aluminum region was a thin, continuous band of nickel-tungsten-tantalum oxide,

followed by a thicker, continuous and very dense band of chromium oxide. A thin band of chromium-titanium oxide, inconsistent in thickness, formed atop the chromium-rich band. Finally, outermost regions rich in Ni and Ti were observed at some oxidation times, but their presence was very sporadic, and these weak oxide regions may have spalled from the surface due to differences in CTE between different oxide regions during cooling or during the process of grinding
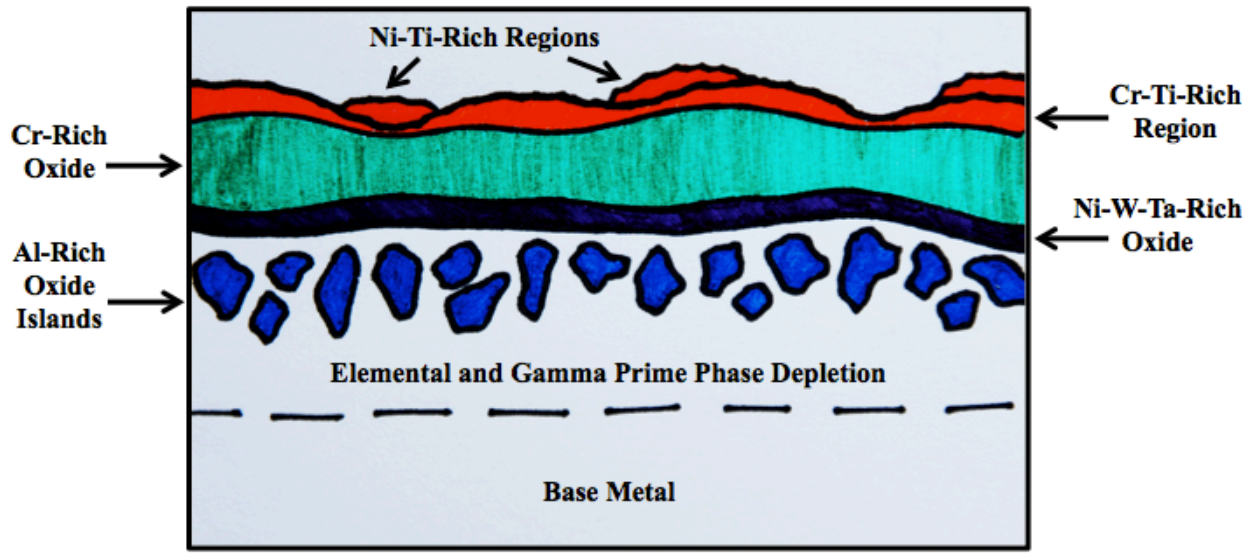
Figure 4.18: A schematic showing the distinct regions of oxidation formed in and on GTD111 at 900°C.

4.1.5.3 Analysis of the Time Dependence of Each Region's Chemistry

After a general schematic had been developed for the oxidation behaviour of the GTD111 superalloy, it was important to analyze any changes in the chemistry of each region as the oxidation time increased. From the element map overlays in Section 4.1.4, it appeared that there were different elemental concentrations in some regions at different oxidation times. For example, the amount of Ti in the Ni-W-Ta band increased with time, and the chromium and Ti regions exhibited changes in chemistry between 308 and 452 hours. This was verified by plotting the main alloying elements' concentrations with respect to time for each distinct region, as shown in Figures 4.19 to 4.22. Each graph plots the concentration of nickel and the main alloying elements against the oxidation time. In each case, one measurement was taken from inside the specific distinct region at each oxidation time. For example, Figure 4.20 a shows the results of EDX analysis taken from within the aluminum oxide region of each oxidized sample.
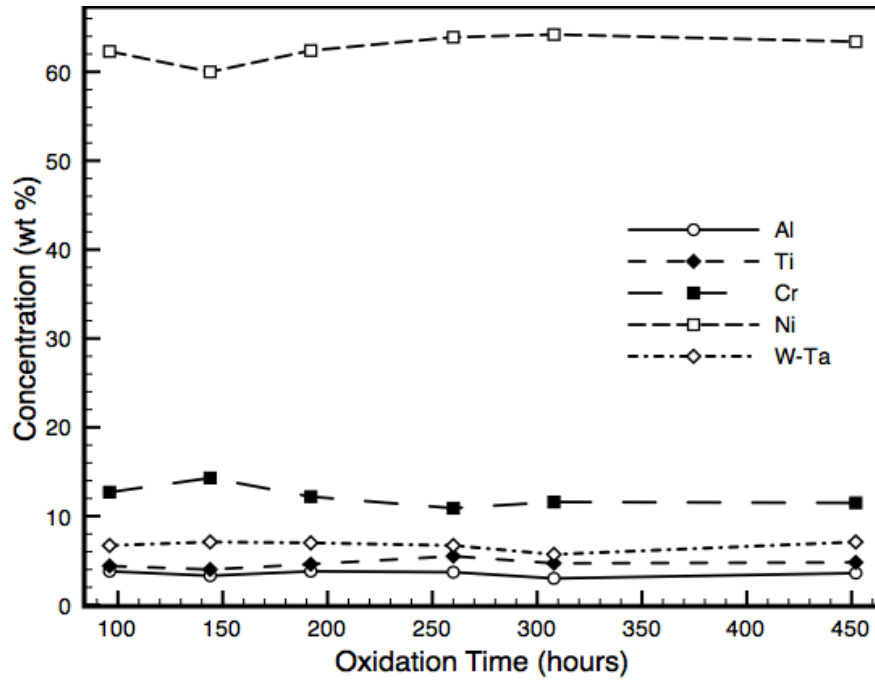
(a) Base Region
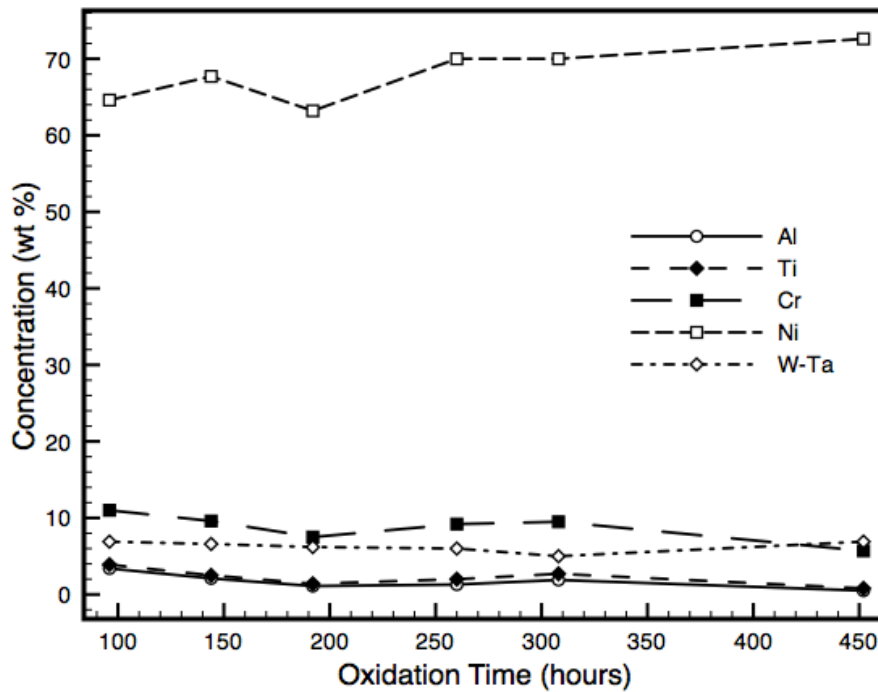
(b) Lower Depleted Region

Figure 4.19: The effect of oxidation time on the chemistry of: (a) the base region (1) and (b) the lower depleted region (2).
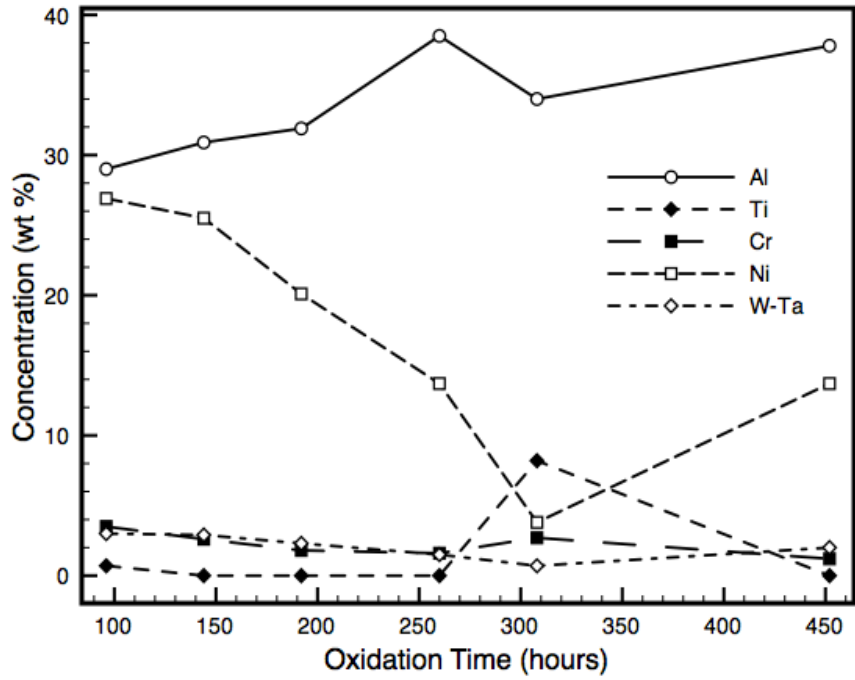
(a) Al Region
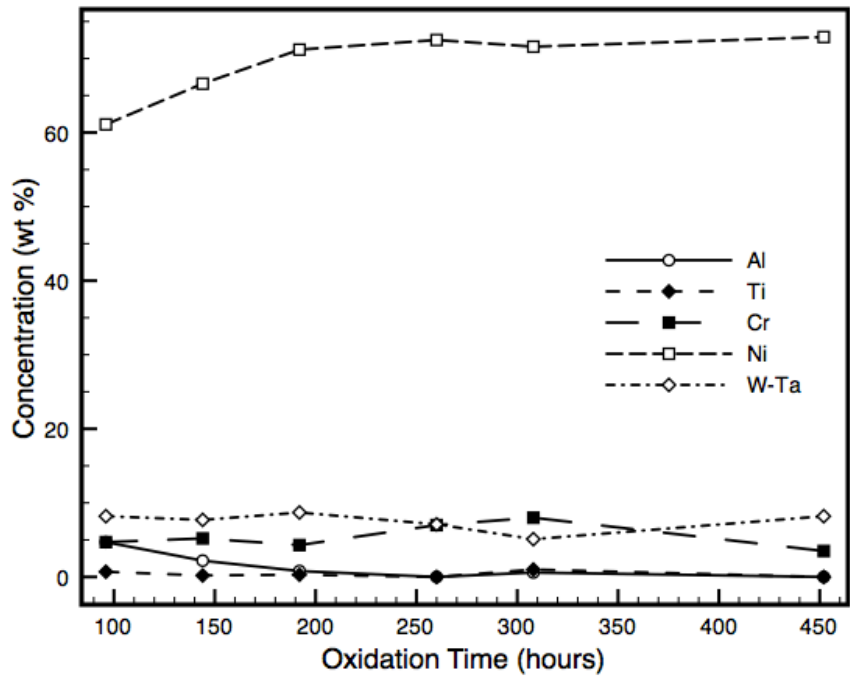
(b) Upper Depleted Region

Figure 4.20: The effect of oxidation time on the chemistry of: (a) the Al region (3) and (b) the upper depleted region (4).
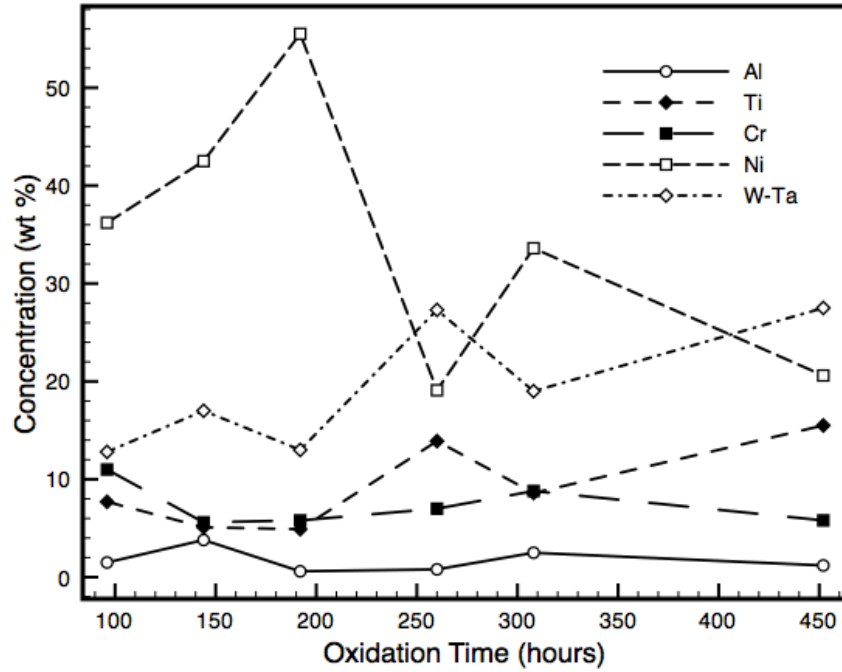
(a) Ni-W-Ta Region
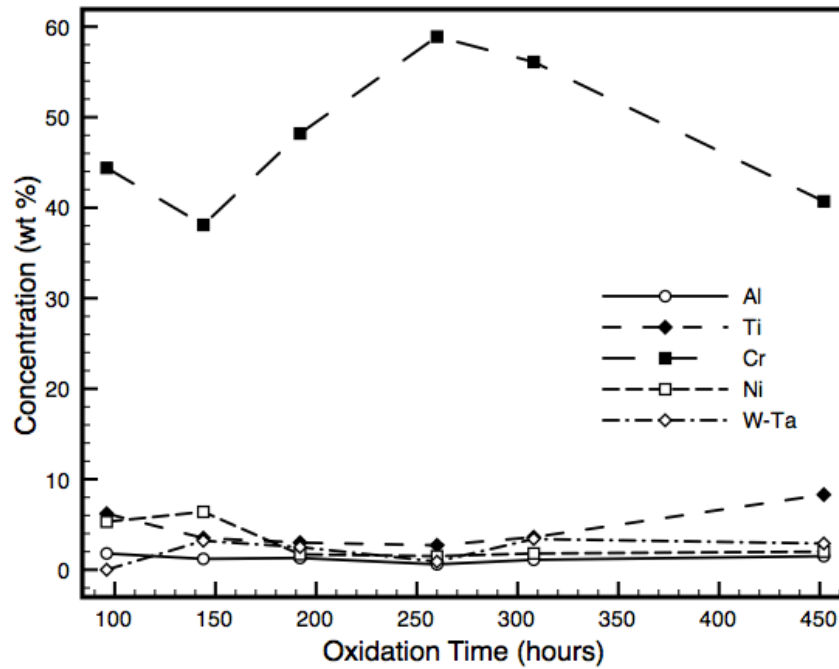
(b) Cr Region

Figure 4.21: The effect of oxidation time on the chemistry of: (a) the Ni-W-Ta region (5) and (b) the Cr region (6).
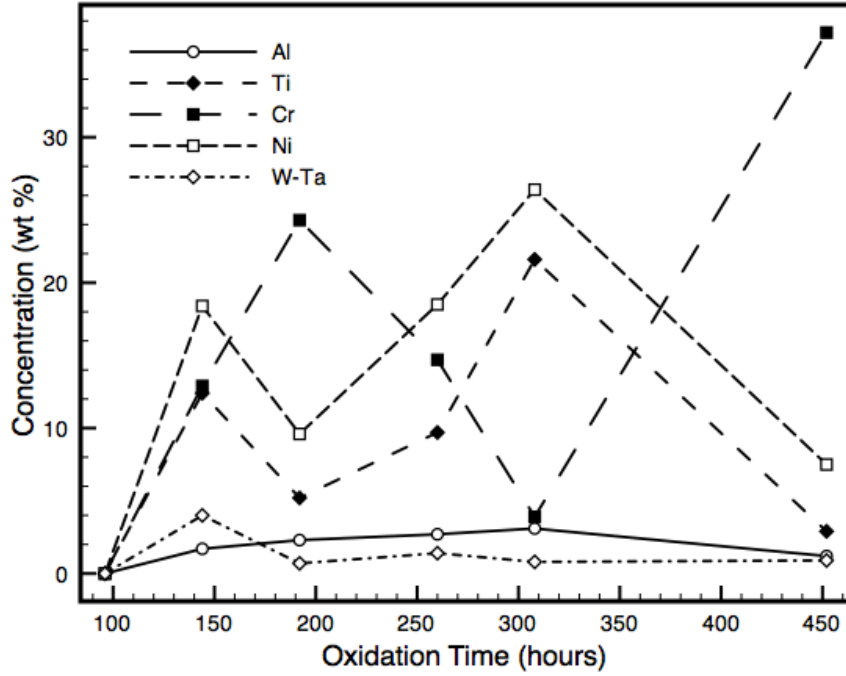
(a) Cr-Ti Region
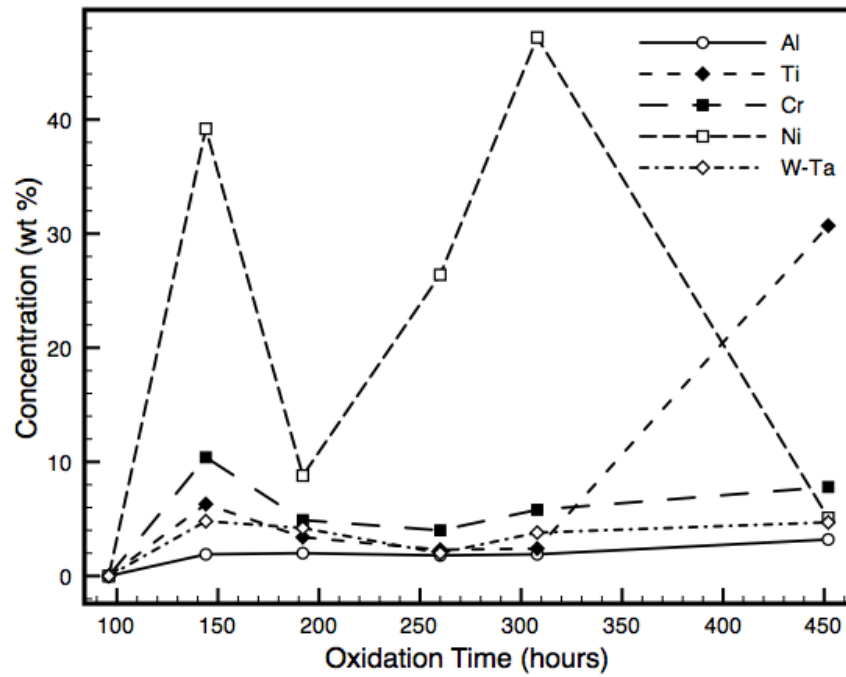
(b) N-Ti External Region

Figure 4.22: The effect of oxidation time on the chemistry of: (a) the Cr-Ti region (7) and (b) the Ni-Ti external region (8).

The above figures showed the changes in chemistry experienced by each distinct region within the oxidized structure with respect to oxidation time. Figure 4.19 a shows that the base metal chemistry did not fluctuate with increasing time, but the chemistries of the lower and upper depleted regions (see Figures 4.19 b and 4.20 b) exhibited depletion of all elements over time. The upper depleted region showed a small increase in Ti content at 308 hours, which may have been tied to the large amount of Ti particles observed in the element mapping of the sample oxidized for 308 hours (see Figure 4.14). The Al region chemistry in Figure 4.20 a showed an increase in Al content and a decrease in the amounts of all other elements, as this region continued to draw in more oxygen and aluminum over time. Again, a spike was seen in the Ti concentration at this time. The Ni-W-Ta band in Figure 4.21 a increased in W-Ta and Ti content, and also experienced a decrease in Ni content, over time. The dense band high in Cr increased in Cr content until 260 hours, when its Cr content began to drop. This drop in Cr content was accompanied by an increased amount of Ti observed in this region (Figure 4.21 b). The Cr-Ti-rich oxide scale exhibited a great deal of fluctuation in chemical content with respect to time, as shown in Figure 4.22. This could be due to the inconsistent nature of this region, as the element maps in Figures 4.10 to 4.15 showed that the Ti region was much less consistent in thickness and density of particles than the Cr-rich region below it. Finally, Figure 4.22 b showed that the outermost region rich in Ni and Ti, which was observed only at a few oxidation times due to its spallation from the surface, fluctuated in chemistry between the times of 308 and 452 hours. It is possible that the Ni-Ti external region had spalled from the surface, leaving the Cr-Ti-rich oxide as the outermost phase at this time. It should be noted that the spallation of the Ni-Ti-rich external oxide may have been due to CTE mismatch between oxide regions – in which case spallation would be the result of cooling from high temperature – or this phase may have been removed during the grinding process. Either case indicates the weak, non-protective nature of the outermost oxide scales.

4.1.4 X-Ray Diffraction Analysis of Surface Oxides

X-Ray Diffraction was performed on the surface of each sample to determine the outermost oxides present at each oxidation time. All peaks observed through XRD analysis were associated with oxides of Ni, Ti, and Cr, which was consistent with the EDX data obtained in Section 4.1.5.2, which found Ni, Ti, and Cr to be the largest contributors to the outermost oxide regions, as is shown in the XRD plots in Figures 4.23 to 4.25. However, the database used for XRD analysis was not capable of providing clear identification of the actual oxide compounds observed. That is, the database could not differentiate beteen CrO_2 and Cr_2O_3. For this reason, the actual oxide compounds observed could not be identified, but it was clear that the only oxides of Ni, Ti, and Cr were present at the surfaces of oxidized samples.
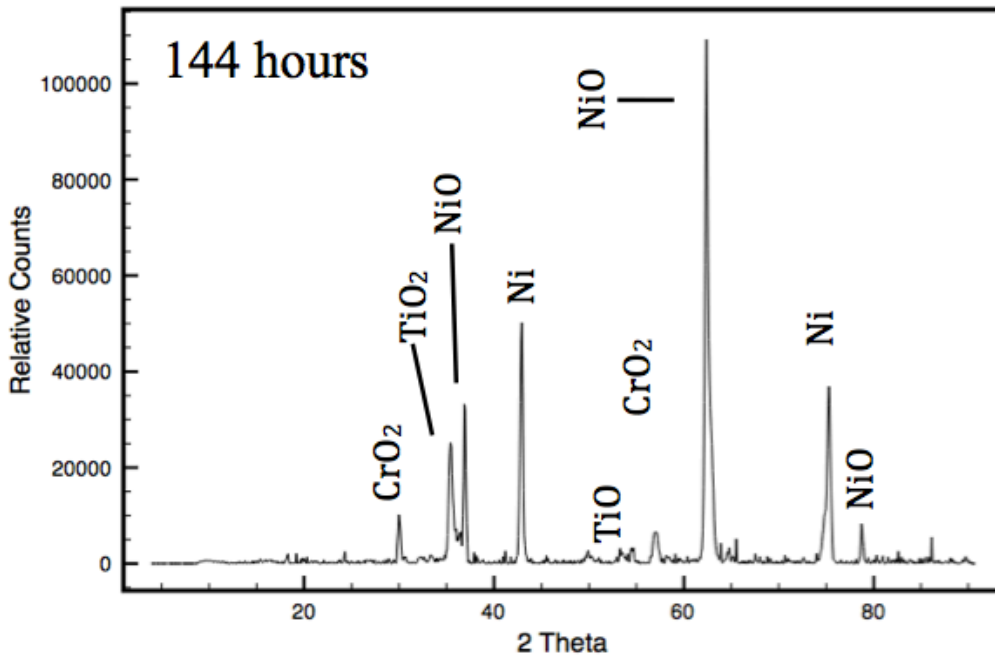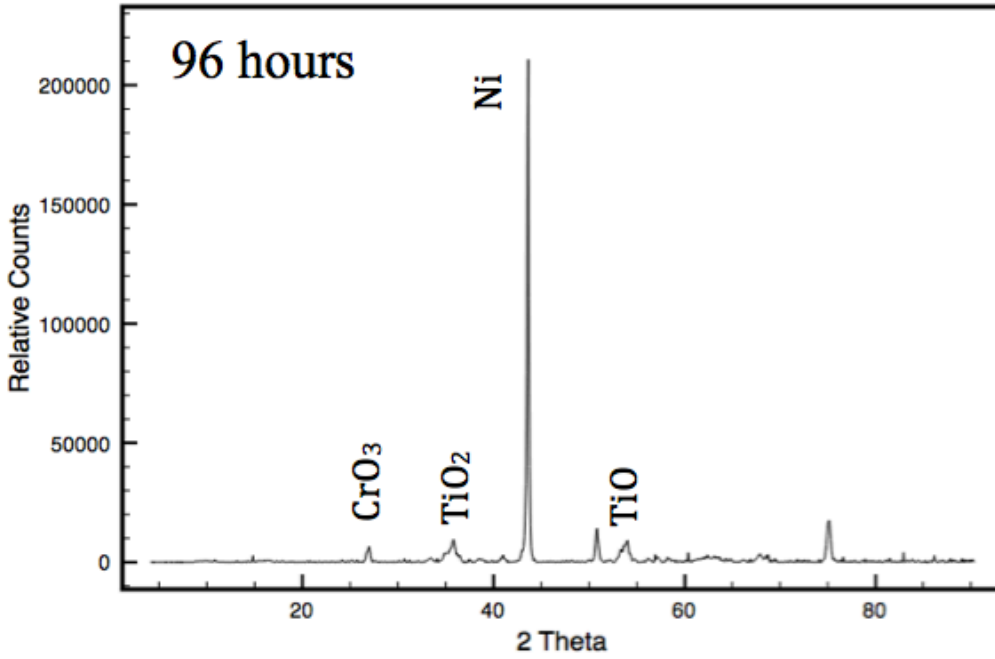
Figure 4.23: XRD plots of the peaks observed after 96 and 144 hours of oxidation.
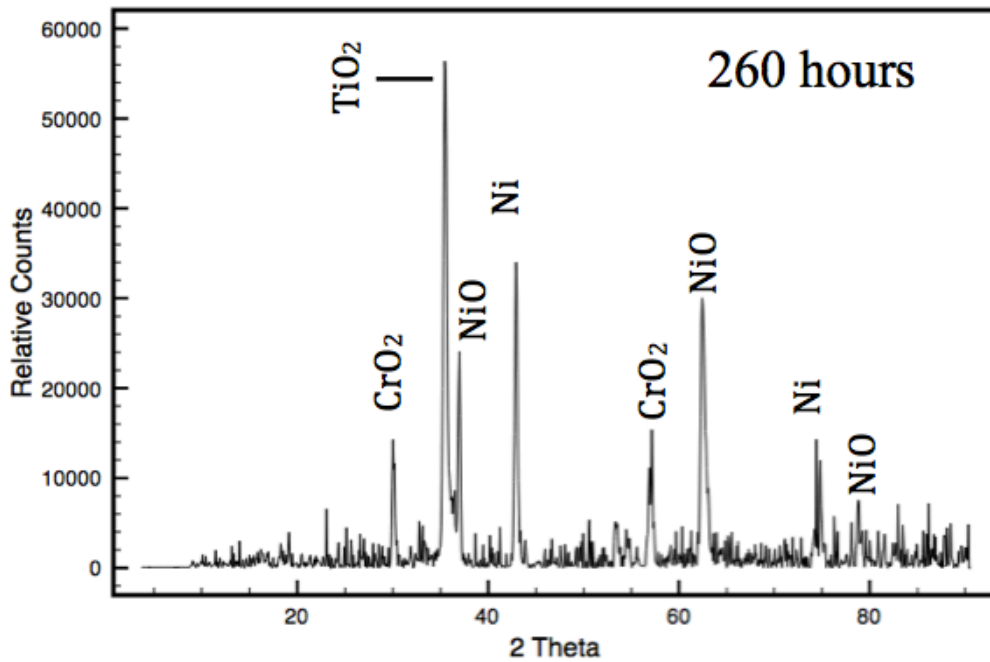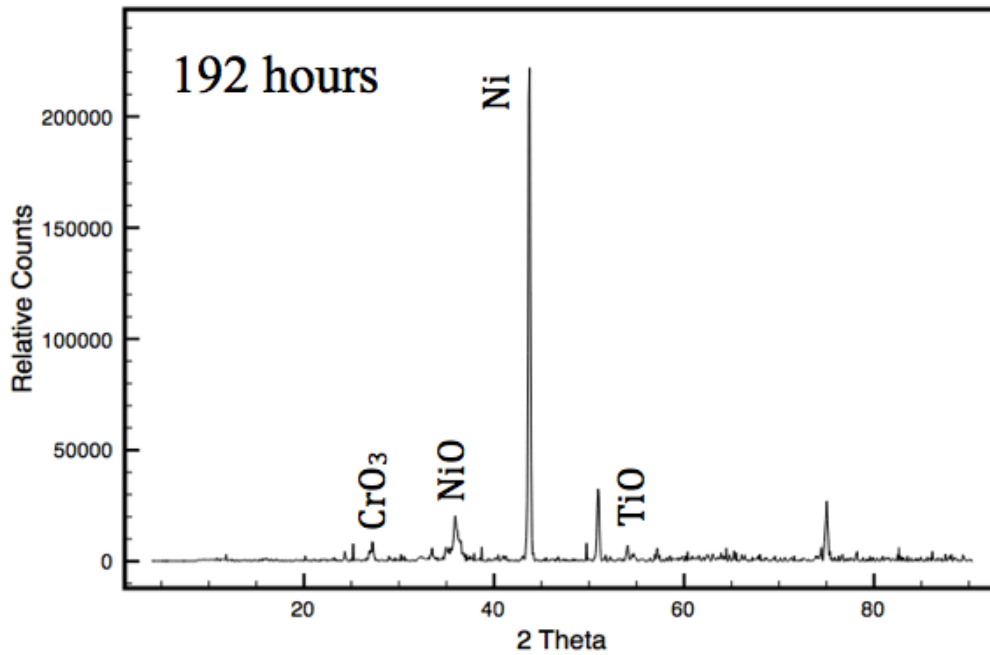
Figure 4.24: XRD plots of the peaks observed after 96 and 144 hours of oxidation.
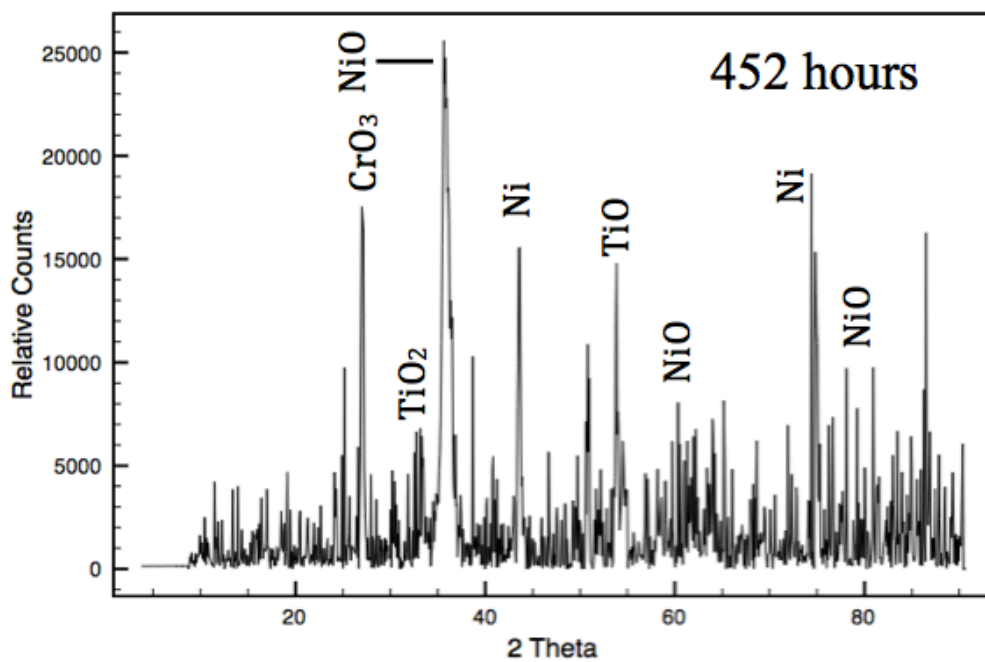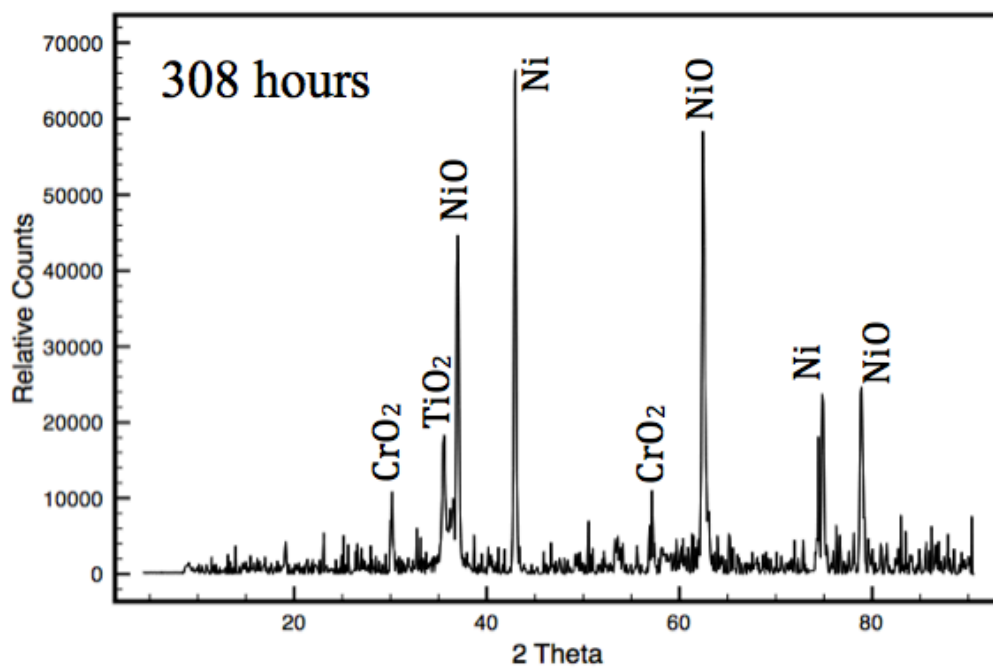
Figure 4.25: XRD plots of the peaks observed after 96 and 144 hours of oxidation.

4.2 Discussion

4.2.1 The Outermost Oxides Exhibited the most Fluctuation

Since the two exterior regions were the only oxide regions whose compositions changed drastically with respect to time, it can be stated that their presence or absence could have the largest effect on the overall oxide thickness. The upper exterior region, especially, exhibited large fluctuations, and was only present at times of 260 and 308 hours, where the overall oxide thickness was observed to be the greatest in Figure 4.25.

Two explanations can be considered for the presence or absence of the variable external oxide regions. Firstly, the exterior oxides, which were largely composed of Ni and Ti, were non-protective in nature, as only the oxides formed from Al and Cr have been found to form dense, protective layers in nickel-based superalloys [8]. Stresses induced by differences in the coefficients of thermal expansion of different oxide scales may have caused the weak oxide regions to spall from the surface, especially during cooling [17].

Secondly, oxide particles first formed at oxide-former sites on the surface of a material, and grew laterally to coalesce into a thin oxide film. With increased time at high temperature, the external oxide regions films grew outward from the surface. The growth of this weak, low-density oxide may have resulted in induced pores and cracks in the oxidized structure, weakening the scale. Shawkat and Xiao [4] stated that the transient oxides on nickel-based superalloys became especially weak after a certain thickness, and spalled from the surface, although the study did not mention a specific thickness at which this occurred.

4.2.2 Time-Dependent Multi-Layer Oxide Growth

Similar to many past publications [2,16,19,37], distinct multilayer growth was observed on GTD111 oxidized at all times studied. While multilayer growth was observed in all past studies, the current work provided more detailed analysis of the distinct oxide regions, as well as a time-dependent chemistry within the oxidized structure on a nickel-based superalloy containing Cr, Al, and Ti.

4.2.2.1 Description of Overall Oxide Structure

The schematic of the overall oxide structure (see Figure 4.18) provides greater detail on the distinct regions of oxidation formed on GTD111 and other such nickel-based superalloys than has been presented in previous publications. The oxidized structure for all times, as observed in the element mapping of Section 4.1.3, contained an innermost discontinuous aluminum oxide region, followed by a continuous band of Ni-W-Ta oxide, a continuous and very dense band of chromium oxide, an inconsistent region rich in Cr and Ti, and an outermost, inconsistently-present region rich in Ni and Ti that was present only at some oxidation times. The outermost Ni-Ti rich region may have spalled from the surface due to CTE mismatch between oxide regions – in which case spallation would be the result of cooling from high temperature – or due to the forces experienced during grinding. Either case indicates the weak, non-protective nature of the outermost oxide scales. The regions rich in Al and Cr observed must be Al_2O_3 and Cr_2O_3, since these are the only stable oxides formed in the Al-O and Cr-O systems [37], although the XRD analysis in Section 4.1.4 could not verify this. Further XRD analysis using a more complete oxide database is recommended.

The innermost oxide region formed on a component is said to be the most thermodynamically stable oxide, as it has the ability to form furthest from the source of oxygen atoms [3]. A continuous alumina layer is the most protective oxide that can be formed in a nickel-based superalloy component, since it has the best ability to slow the transport of other metal ions through its lattice in the range of 900 to 1200°C [39]. However, an alloy must contain at least 5 to 7% Al for the formation of a continuous alumina layer to occur [10]. Since this is not the case for GTD111, a continuous aluminum oxide layer was not formed, and the continuous band of chromium oxide provided the most protection against further oxidation for this alloy. This observation agrees with Patnaik [37], who stated that the internal oxidation of Al_2O_3 occurs where the main protective scale in the alloy is Cr_2O_3, due to the higher free energy of formation of Al when compared to Cr. However, this internal oxidation can have deleterious effects on the strength of a component due to the depletion of aluminum, a main strengthening element, from the base metal [39], and the depletion of the strengthening gamma prime phase (due to Ti and Al particles being stripped from the gamma prime phase to form Ti and Al oxide compounds) was observed by optical microscopy in Section 4.1.1.

Recall that Trexler *et al.* [19] observed three distinct oxide layers formed on GTD111 after 312 hours at 982°C. The "inner oxide layer" contained at least two distinct regions, and was high in Ni and Al. The current study showed that this "inner oxide layer" was in fact made up of three distinct regions; an aluminum oxide region, the upper depleted region, and a thin band of Ni-W-Ta oxide. This agreed with a finding from Sato *et al.* [10], who observed the formation of a layer rich in Ni and Ta between the chromia and alumina regions.

4.2.2.2 Effect of Time on the Chemistry of Distinct Oxide Regions

An interesting observation concerned the buildup of Ti particles below the aluminum oxide region on samples oxidized for 192, 260, and 308 hours, as indicated by the small grey dots observed below the black aluminum oxide phases on the BSE images in Section 4.1.3. The Ti ions in the material appeared to be constantly moving toward the surface of the component to meet with the O ions in the air. This movement likely became more difficult after the formation of the dense band of chromium oxide, as the buildup of Ti was observed to increase from 192 to 308 hours, but the sample oxidized for 452 hours was observed to be free of such a phase. This observation has not been made in past studies, and it can be assumed that the Ti particles were eventually able to migrate through the Al and Cr regions. For example, at 308 hours (see Figure 4.14), where the amount of Ti particles was greatest, a small amount of Ti was detected in the aluminum oxide region, indicated by the spike in Ti at 308 hours in Figure 4.20 a. This sample, therefore, captured the migration of the Ti particles toward the surface. Also, the Ti element map of the sample oxidized for 452 hours (see Figure 4.15) and the EDX analysis plots for the Ni-W-Ta and Cr-Ti oxide regions (Figures 4.21 a and 4.22 a, respectively) showed a much higher amount of Ti. These observations suggested the migration of Ti particles toward the surface between 308 and 452 hours.

4.2.3 Order of Oxide Growth

The element maps of the sample oxidized for one hour (Figure 4.8) showed that small amounts of titanium oxide was the first to form. Titanium has the lowest free energy of formation on the Ellingham diagram (see Figure 2.1), and as such it made sense that Ti was the first-formed oxide. Thin regions of Al and Cr oxides within the surface were the next to form, and were both observed in the element maps of the sample oxidized for four hours (see Figure 4.9). Aluminum has a lower free energy of formation (see Figure 2.1) than chromium when associated with oxygen, but it has been found in past studies [10,11] that alumina formation is generally quite slow in comparison to that of chromia, so it is therefore concluded that the chromium oxide region forms before the aluminum oxide region. After the initial formation of Al and Cr oxides, Ni and Ti continued to migrate through these regions to form oxide compounds at the surface, and the Ni-W-Ta oxide band was formed after approximately 96 hours of oxidation (see Figure 4.10). The Ni and Ti oxides at the surface formed one or two external transient oxide regions, which were present at some times and absent at others, as their weak, low-density nature would have resulted in their spallation from the surface of the oxidized component, most likely upon cooling [17].

4.3 Summary

The results of this chapter have shown that the overall oxide structure on and within GTD111 remained almost constant with increasing oxidation time past 96 hours, with slight changes in the chemistry of the distinct regions and the sporadic presence and absence of an outermost oxide rich in Ni and Ti. The presence or absence of such scales could possibly be attributed to spallation during cooling or from removal during the grinding process, and as such further analysis is required, in samples should be mounted ensure the external oxide regions remain intact. Due to the formation of a discontinuous innermost aluminum oxide region, oxidation resistance in the GTD111 alloy can be attributed to the formation of a dense, continuous layer of chromium oxide near the component surface. The first-formed oxide on this alloy was titanium oxide, followed by chromium oxide, aluminum oxide, and lastly by the formation of an oxide layer rich in tungsten and tantalum. Due to the spallation of the weak nickel oxides, it is uncertain where the nickel oxide fits into the order of oxide formation.

In the following chapter, samples that have been oxidized between 96 and 452 hours and cleaned via the FIC process have been analyzed using SEM-EDX and element mapping to determine the ability of the FIC process to remove oxide compounds and to understand the effects of oxidation time on the chemistry of cleaned samples.

Chapter 5 Fluoride-Ion Cleaning of GTD111

In the previous chapter, the results of analysis of the differences in chemistry and oxide structure of samples oxidized between 96 and 452 hours in an air furnace at 900°C were presented. In this chapter, the results of a study of the effectiveness of the FIC process in terms of oxide removal and alloy depletion will be presented. The effect of oxidation time on the ability of the FIC process to remove oxidation and on the resultant chemistry of GTD111 samples were also investigated.

5.1 Results

5.1.1 Optical Microscopy of Oxidized and Cleaned Samples

The difference between the gamma prime depletion on oxidized and cleaned samples was observed via optical microscopy. Figure 5.1 shows optical micrographs of a sample oxidized for 308 hours and a sample oxidized for 308 hours and subsequently cleaned via the FIC process. The depletion of the gamma prime phase was observed on all oxidized and cleaned samples. The oxidized sample exhibited gamma prime depletion only under an external oxide scale, whereas the cleaned sample showed depletion from the surface, indicating that the cleaning process had removed the external scale from the oxidized sample.

(a) 308 hours Oxidized   (b) 308 hours Cleaned
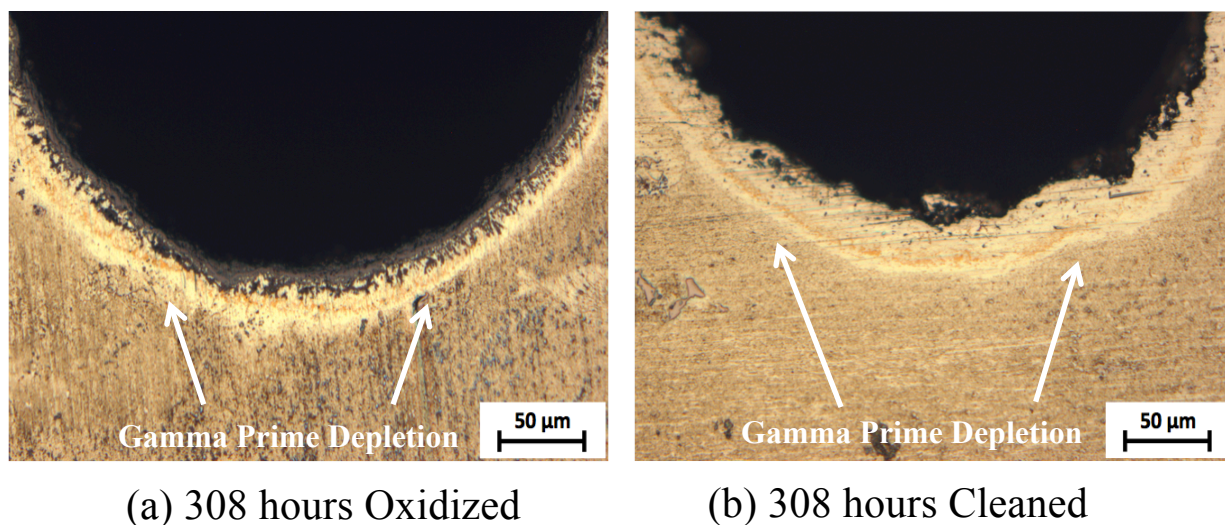
Figure 5.1: Optical micrographs of samples etched with Marble's reagent [40]: (a) oxidized for 308 hours and (b) oxidized for 308 and cleaned via FIC.

The gamma prime depletion observed on cleaned samples reached deeper into the substrate than on the oxidized samples. This indicated that the FIC process had removed all oxide compounds, and then continued to deplete the strong oxide formers of Al and Ti from deeper within the substrate than the oxide had reached. This "over-cleaning" was necessary in ensuring that all oxidation had been removed from the sample and to reduce the possibility of re-oxidation between cleaning and brazing.

5.1.2 Comparison of Oxidized and Cleaned Cross-Sections using Back-Scattered Electron Imaging

Figure 5.2 shows BSE images of samples oxidized for 96, 260, and 452 hours, as well as for the samples oxidized for these times and subsequently cleaned via FIC. A significant difference between the structure of the oxidized and cleaned samples was observed. The oxidized samples exhibited very distinct regions of growth within their structures, whereas the cleaned samples were almost homogeneous, with some evidence of porosity, as indicated in Figure 5.2 f.
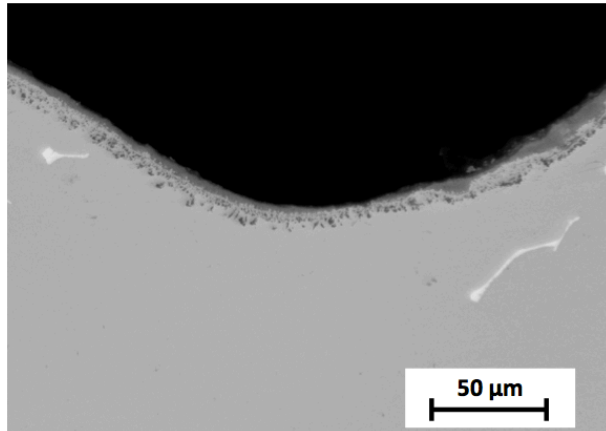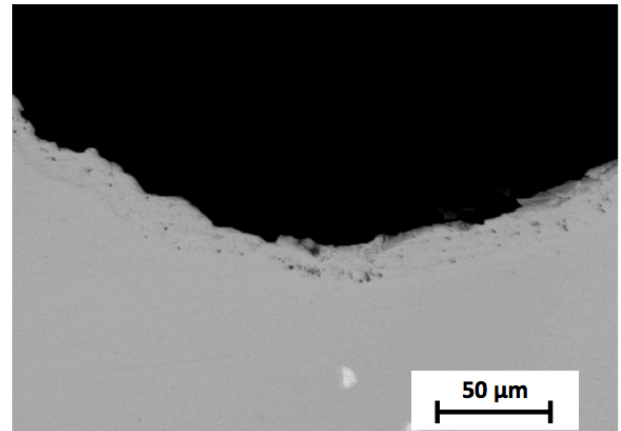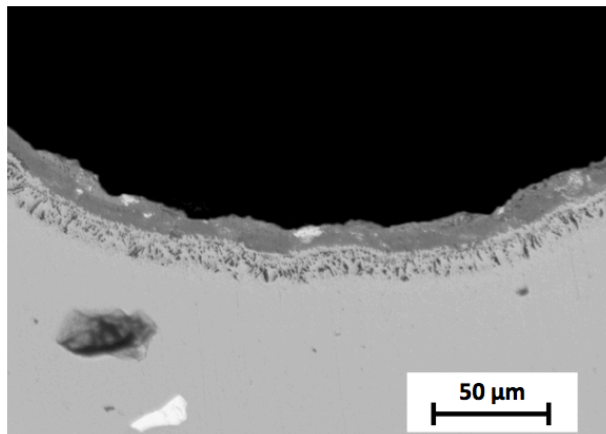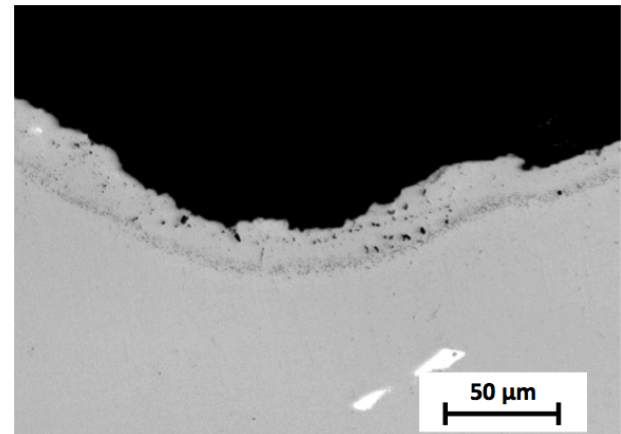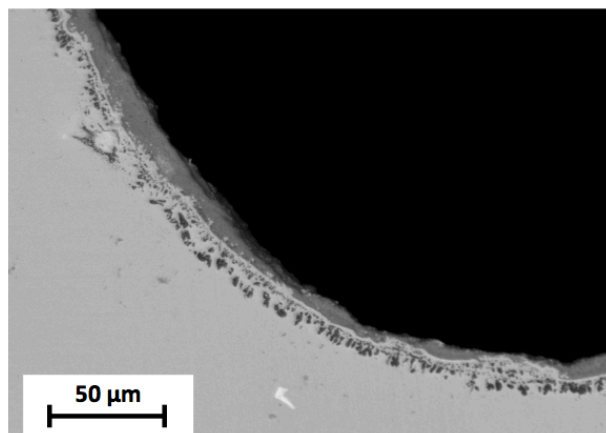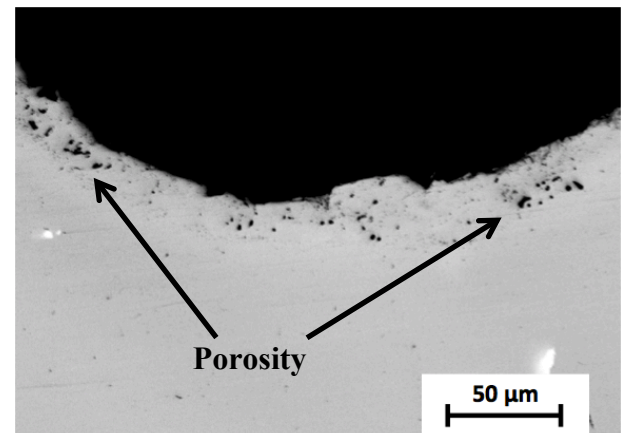
Figure 5.2: BSE images of oxidized (a, c, & e) and cleaned (b, d, & f) samples after various oxidation times.

5.1.3 Elemental Distribution Within Oxidized and Cleaned Samples

Since the BSE images in the previous section could only show differences in the structure, it was necessary to utilize a more analytical tool such as element mapping to understand the differences on a chemical level. Figures 5.3 and 5.4 show the element maps of nickel K-alpha (red), oxygen (light blue), aluminum K-alpha (dark blue), tungsten-tantalum M-alpha (purple), chromium K-alpha (green), and titanium K-alpha (yellow), used to show the differences in elemental distribution near the surfaces of oxidized and cleaned samples. The element maps

Very distinct regions of elemental concentration were observed in the element maps of the oxidized sample, whereas the cleaned sample showed only minor concentrations, aside from the increase in Cr nearest the surface. An important observation made was that there were no obvious signs of oxidation-rich concentrations within the cleaned sample, indicating that the cleaning process had effectively removed all oxide components from the component. On a similar note, only very small concentrations of other elements were observed in the element maps of the cleaned sample, and these concentrations were clearly not tied to oxygen, as indicated by the absence of oxygen concentrations in these regions in Figure 5.4. However, it is important to note that chromium was concentrated in a fairly thick band at the surface, and titanium had formed a thin band within some cleaned samples. The element maps of titanium, aluminum, chromium, and nickel all exhibited, to various degrees, depletion beginning at the surface of the cleaned sample, whereas the depleted region for chromium was completely contained within the subsurface, below a region of increased Cr content near the surface.

From this analysis, it was assumed that Al and Ti reacted strongly with the HF, and were heavily depleted from the surface, while Ni was much less reactive, as was evident from the degree of depletion experienced by each of these elements. Chromium oxide compounds migrated to the surface so that oxygen atoms could be stripped from the oxide, but unlike Al and Ti, the cleaning process did not remove Cr atoms, and instead, these atoms coalesced at the surfaces of the cleaned samples.
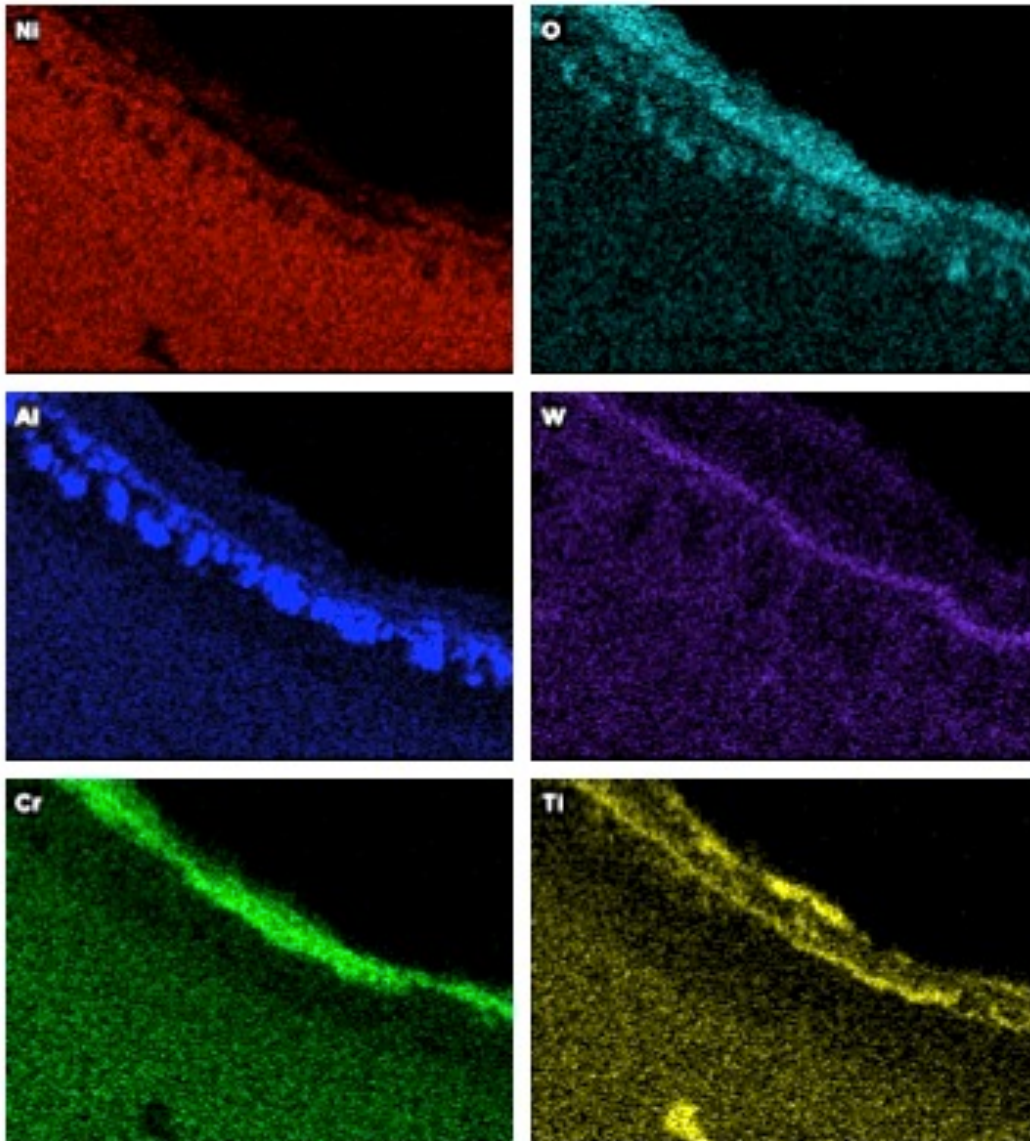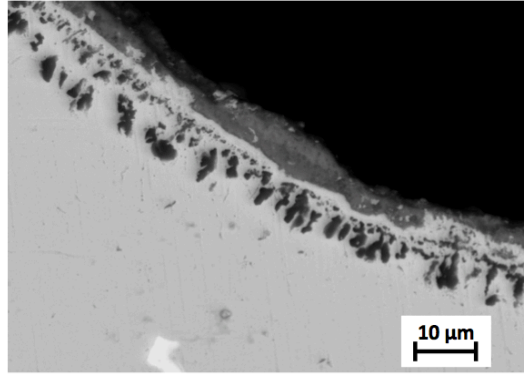
Figure 5.3: BSE image and element maps for the sample oxidized for 452 hours.
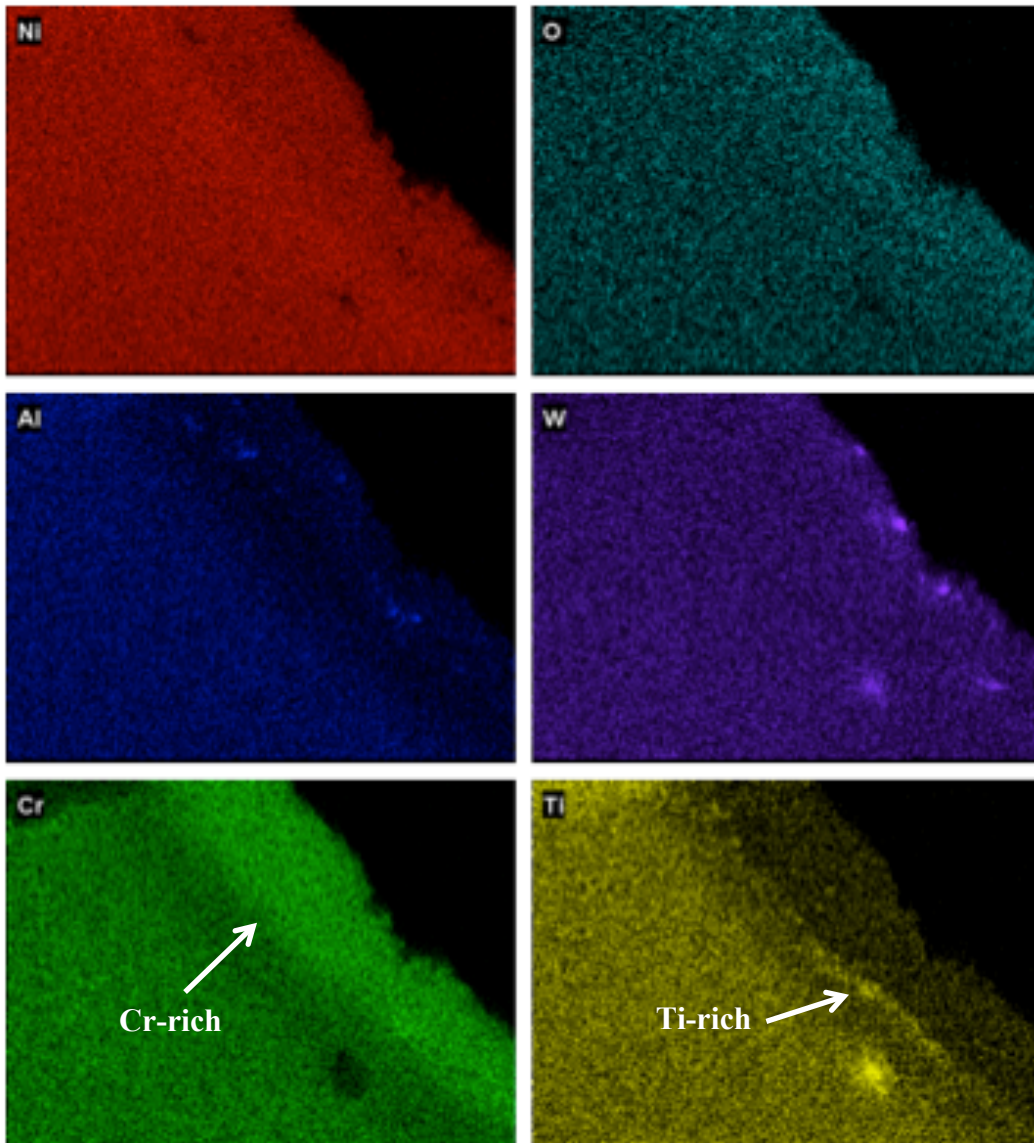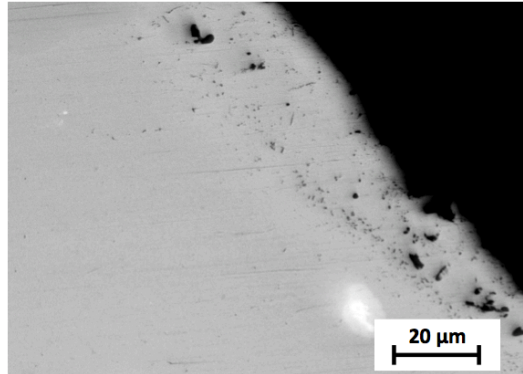
Figure 5.4: BSE image and element maps for the sample oxidized for 452 hours and subsequently cleaned via FIC.

5.1.3.1 Element Map Overlays of Oxidized and Cleaned Samples

Composite element maps for aluminum, titanium, tungsten-tantalum, and chromium have been created to show the distribution of the main oxidizing elements observed in GTD111 before and after the cleaning process.
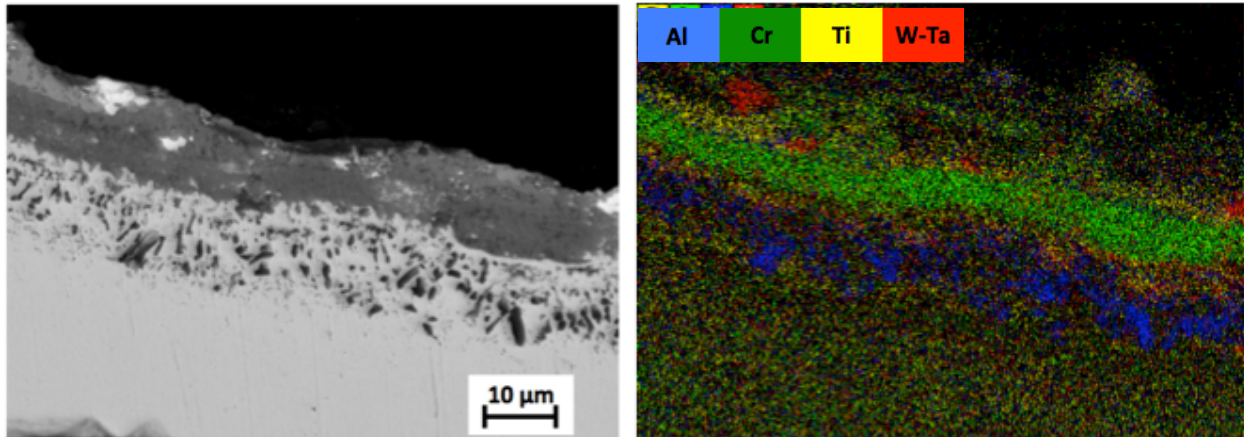
(a) 260 hours Oxidized
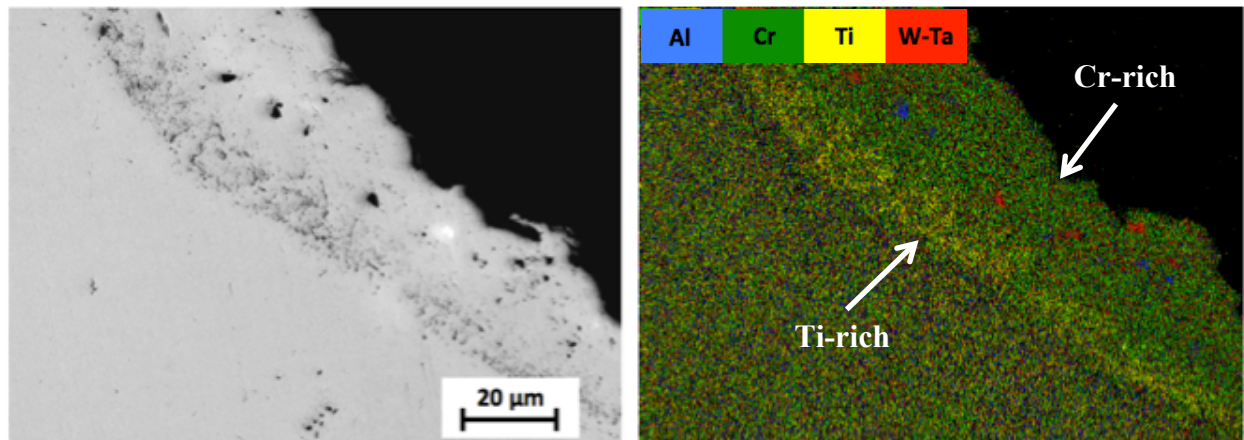
(b) 260 hours Cleaned

Figure 5.5: Element map overlays of aluminum (blue), titanium (gold), chromium (green), and tungsten-tantalum (red) of a sample: (a) oxidized for 260 hours and (b) oxidized for 260 hours and subsequently cleaned via FIC.

A noticeable difference was observed between the elemental distribution of oxidizing elements within the oxidized and cleaned samples. The only elemental concentrations observed in the cleaned sample were an increased Cr content (green region) near the surface and a thin band of titanium (yellow) observed beneath the Cr region. However, there was no oxygen associated with these regions, and they were found to simply be accumulations of the alloying elements. Previous studies on the FIC process [1, 21] have pointed out the depletions of Al and Ti, but the concentration of Cr near the surface of cleaned samples has not been previously observed.

5.1.4 Chemical Analysis via Energy-Dispersive X-Ray Spectrometry

Thus far, only qualitative methods have been used to compare oxidized and cleaned samples. A relatively homogenous structure seemingly devoid of oxygen was observed in the cleaned samples. That being said, it was important to obtain some quantitative data in order to verify the presence or absence of oxidation.

5.1.4.1 EDX Analysis Locations

EDX analysis was performed at five points within each cleaned sample, starting near the surface and ending after the depleted region, at which point it was assumed to have roughly the chemical content of the base material. Figure 5.6 below shows the locations of EDX analysis on a BSE image and on the element maps of aluminum (blue), titanium (yellow), and chromium (green). It is clear that the locations selected for EDX analysis covered areas of both depletion and concentration of the alloying elements, as well as the base material of each sample.
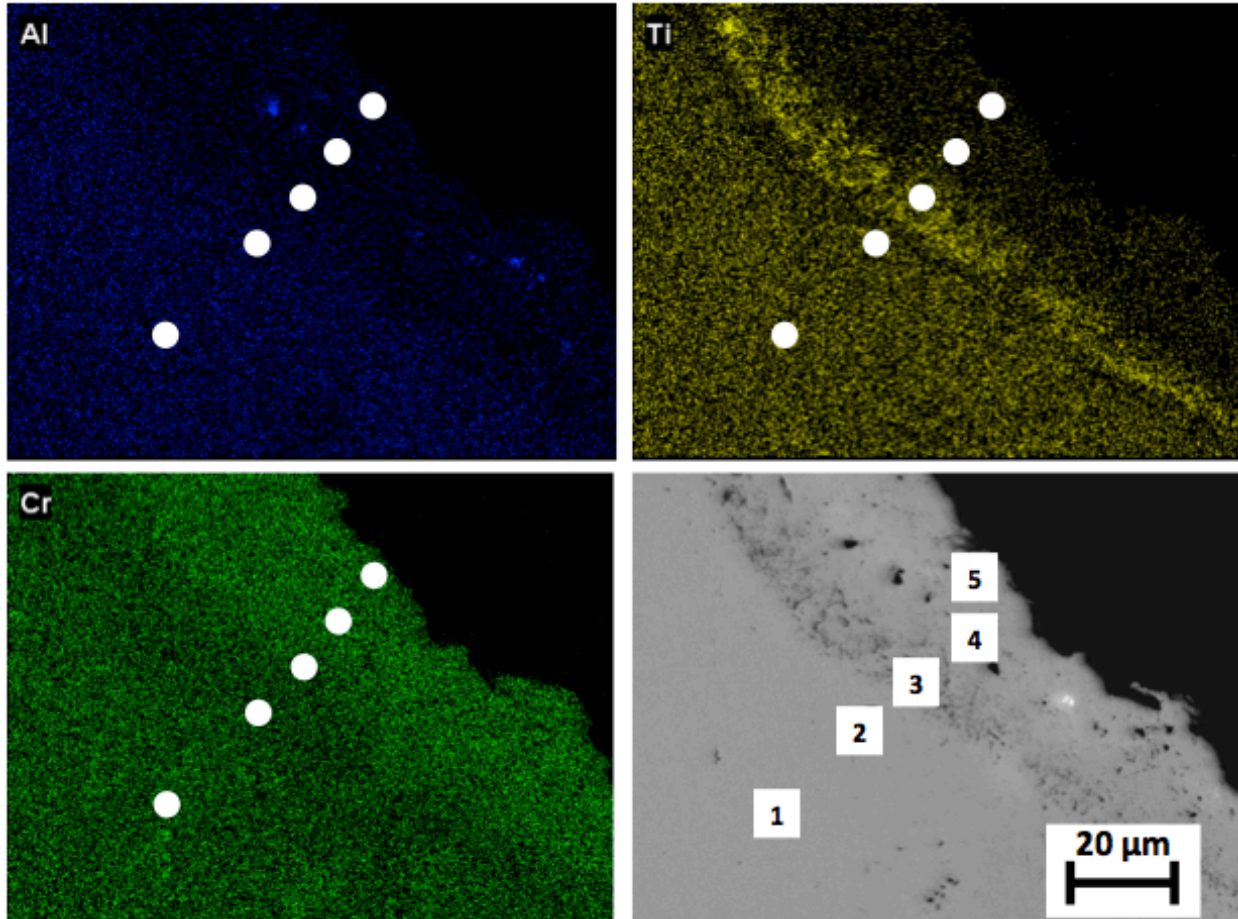
Figure 5.6: Element maps and a BSE image, including the locations of elemental analysis via EDX on a sample oxidized for 260 hours and subsequently cleaned via FIC.

5.1.4.2 EDX Analysis Results

The locations selected on each sample were very close, but not exactly the same, in depth. The average depth of each location has been used to summarize the data from all samples. Figure 5.7 below shows the data, in terms of the average semi-quantitative chemical concentration in weight-percent at each location's average depth across the six cleaned samples.
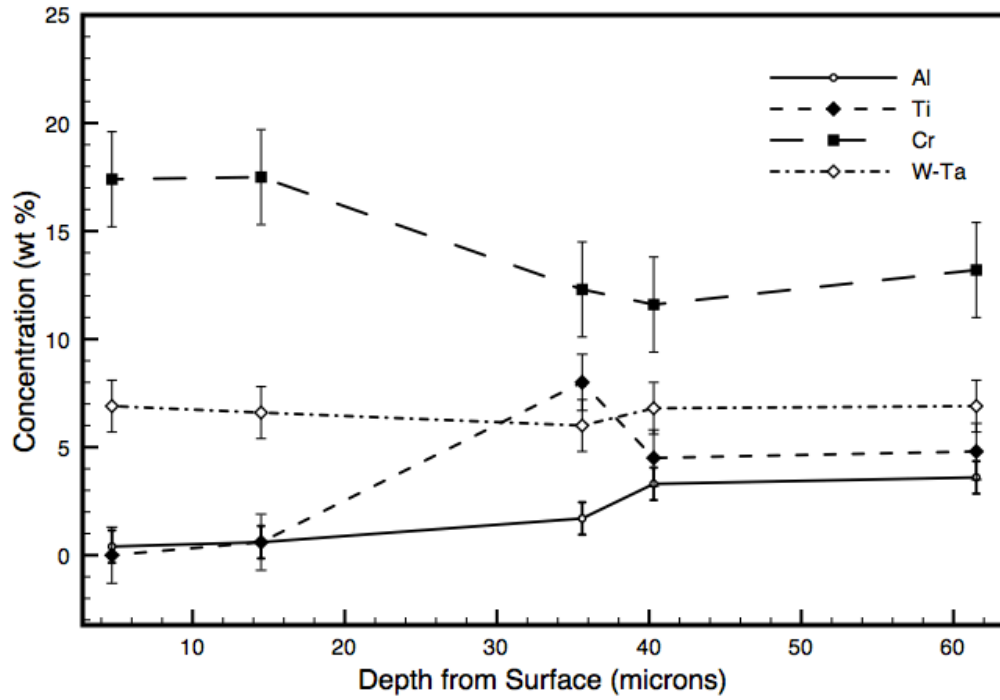
(a)
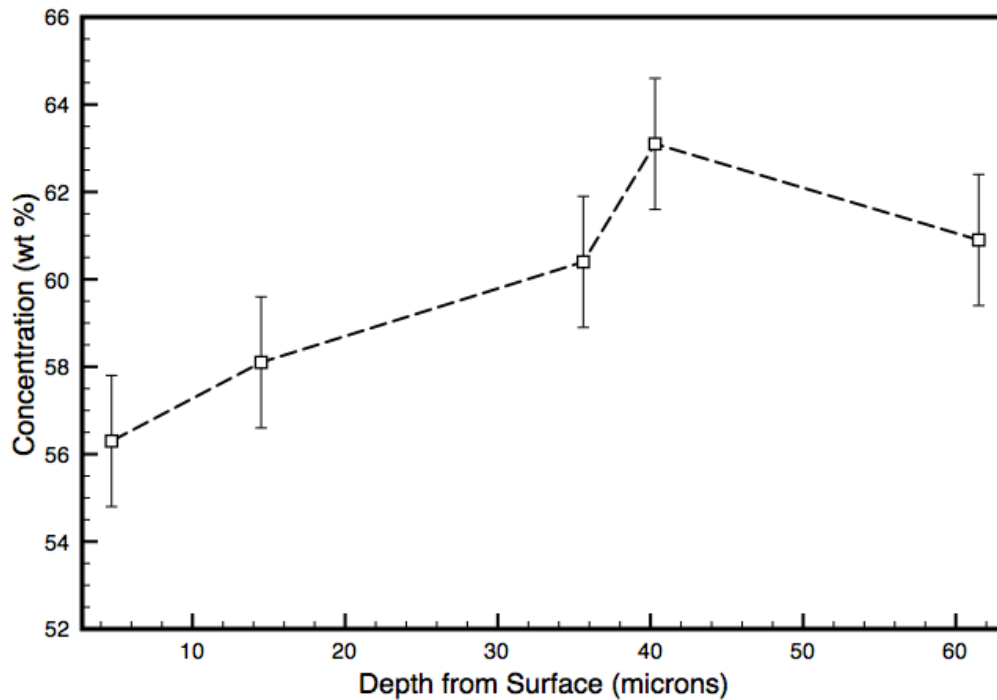
(b)

Figure 5.7: Average concentration of: (a) major alloying elements and (b) nickel with respect to the distance from the surface of a cleaned sample.

The amount of each element, with the exception of W-Ta, was found to vary as the depth from the surface increased, in a manner similar to that observed in the element maps of Figure 5.6. Essentially no aluminum was observed within the first 35.5 μm of the cleaned sample, after which point the concentration of aluminum increased back to normal. This observation supported the claim of previous studies, which also observed a noticeable depletion of aluminum near the surface of a component cleaned by the FIC process [1,8,21,22].

Titanium was found to follow a very similar trend to that of aluminum, except that the depletion of titanium was observed only until 27.2 μm. Also, an increase in titanium was observed at approximately 35 μm on each sample, in the form of a Ti-rich band. No oxygen was associated with this band; it was determined to simply be a region of titanium concentration.

In a similar manner to aluminum and titanium, but to a much lesser extent, the cleaned samples exhibited nickel depletion to a maximum depth of 34.7 μm. This slight nickel depletion had not been previously described by literature and was therefore not expected. This depletion was much less obvious, especially in the element maps, before 260 hours of oxidation time.

Chromium experienced an interesting distribution within the structure of the cleaned samples, as Figures 5.6 and 5.7 showed that chromium is concentrated, in an opposite manner to the depletion of aluminum and titanium nearest the surface, to a maximum depth of 24 μm. Also, observed between this region of concentration and the base material was a region of chromium depletion, which was, on average approximately 10 μm thick.

5.1.5 Effect of Time on the Chemistry of Samples Cleaned via FIC

The previous chapter showed that samples oxidized for different times exhibited differences in the overall oxide structure and in the chemistry of the distinct regions observed. It was predicted that such chemical differences might have affected the chemistry of cleaned samples that had been previously oxidized for different durations. Figure 5.8 shows the chemistry, with respect to oxidation time, at depths of 5 and 40 μm from the surface of the cleaned samples.
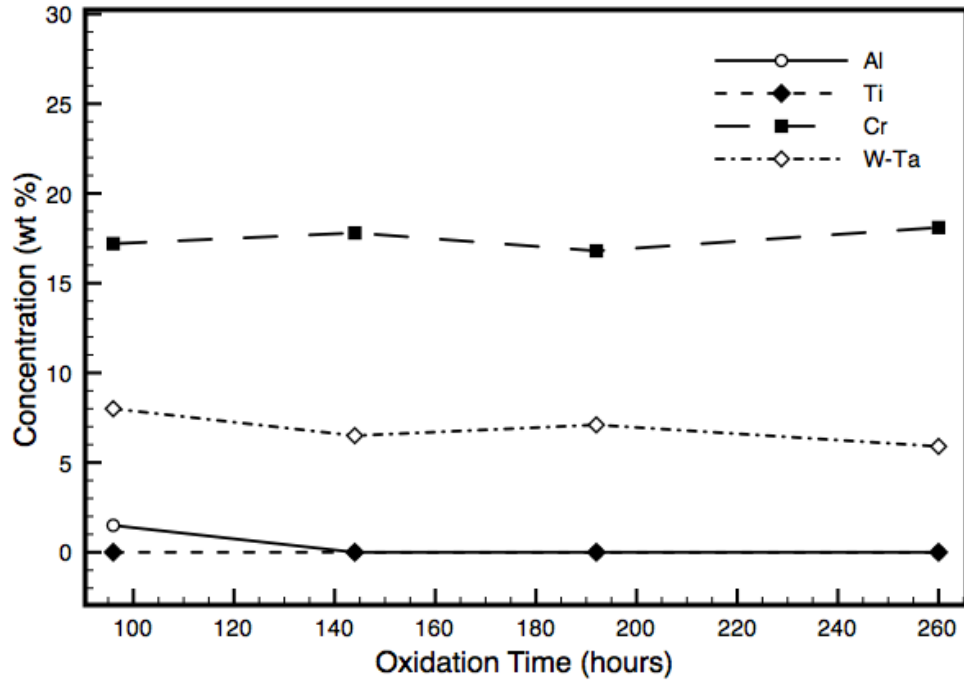
(a)
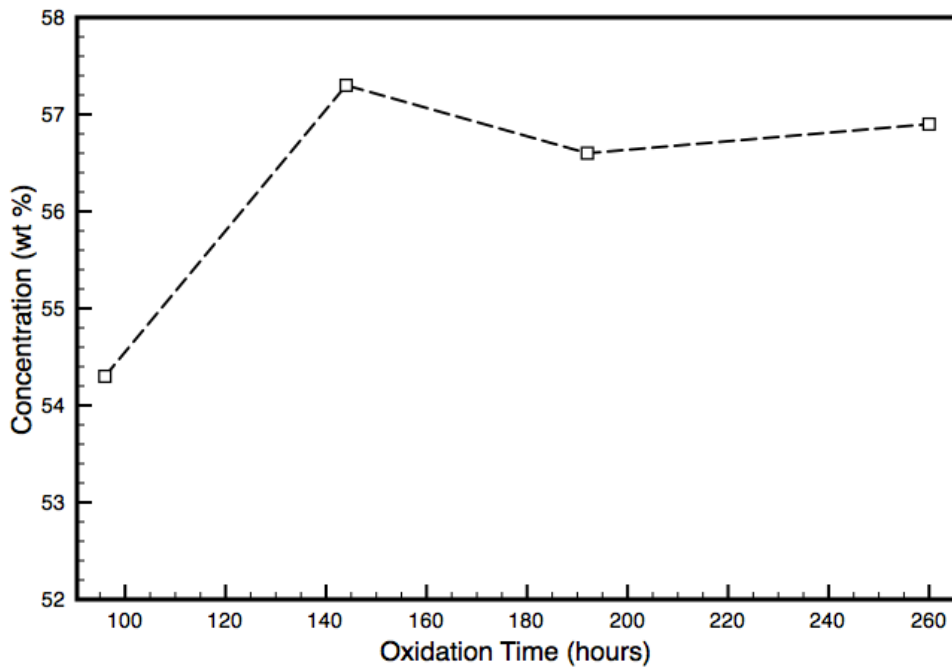
(b)

Figure 5.8: The concentration observed with respect to time 5 μm below the sample surface of: (a) the alloying elements and (b) nickel
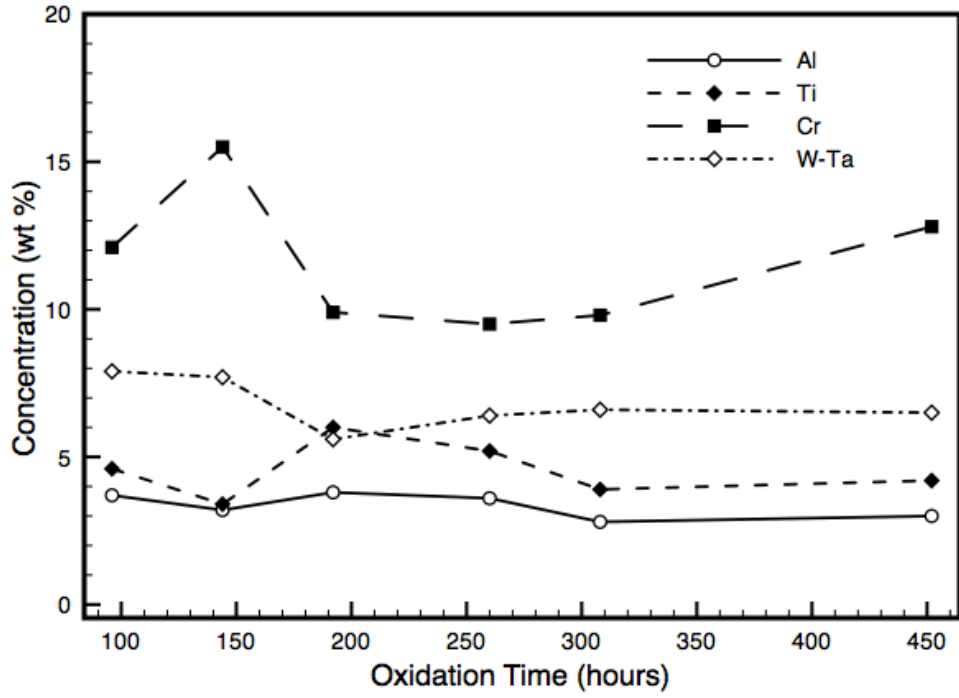
(a)
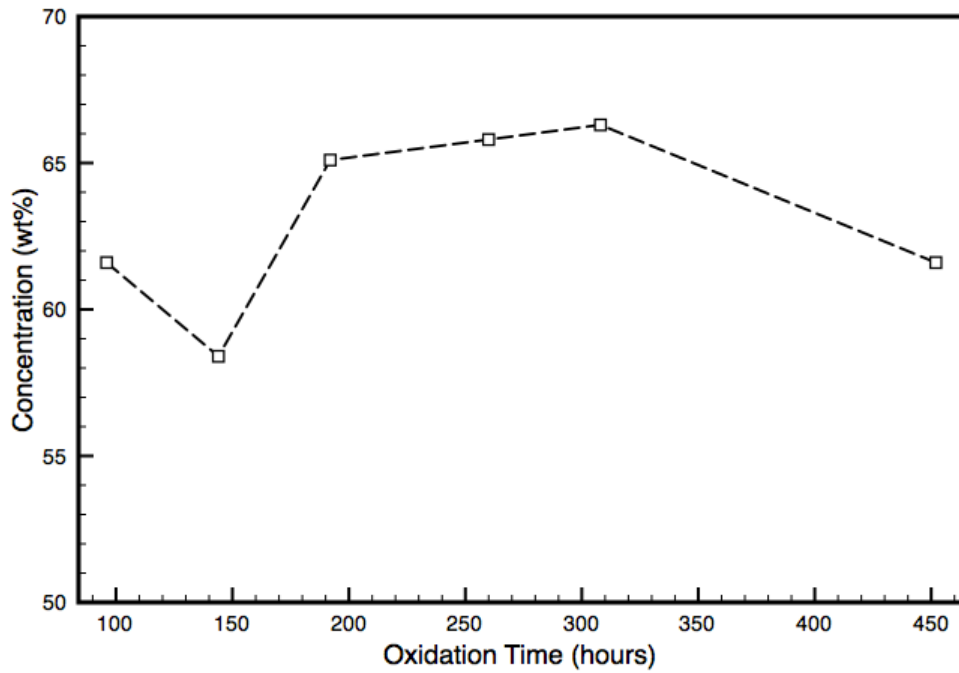
(b)

Figure 5.9: The concentration observed with respect to time 40 μm below the sample surface of: (a) the alloying elements and (b) nickel

The chemistry observed at a specific depth in a cleaned sample was found to be essentially the same at every oxidation time. For example, at the surface of a cleaned sample, the amount of each alloying element remained almost constant throughout the range of oxidation times, as Figure 5.8 showed that the chemistry at given depths of 5 and 40 μm varied only slightly with respect to time. From this it was assumed that the chemistry of a cleaned sample was only weakly dependent on the oxidation time, and that samples oxidized between 96 and 452 hours resulted in essentially the same chemistry after the FIC process had been performed. This was an important observation, as it seemed that a cleaning process would not need to be customized to address the differences in chemistry found after different oxidation times. However, although the average chemistry of cleaned samples remained relatively constant over the range of oxidation times, Figure 5.10 showed that the thickness of elemental and gamma prime phase depletion was found to vary with respect to time.

5.1.6 Depths of Phase and Elemental Depletions and their Dependence on Oxidation Time

Recall from Chapter 4 that the thickness of gamma prime depletion was measured and plotted with respect to time (see Figure 4.3), and from Section 5.1.1 that cleaned samples exhibited deeper gamma prime depletion than their oxidized counterparts (see Figure 5.1). Five measurements of the gamma prime depletion were made on each oxidized and each cleaned sample, and the results have been plotted in Figure 5.10 below. Cleaned samples exhibited more severe gamma prime depletion, which was to be expected, since the cleaning process was conducted at high temperature, which would further draw Al and Ti to the surface to react with the flowing HF gas. This "over-cleaning" effect can be controlled by the process parameters of the FIC process, and ensures that all oxidation is fully removed from the components, as well as reducing the possibility of future oxidation, since the main oxide-formers, Al and Ti, are removed from the surface and immediate subsurface. Both curves exhibited essentially no further gamma prime depletion past 308 hours, which was interesting, since this depletion was expected to increase with oxidation time. This result indicated that some equilibrium had been reached in which further depletion was not necessary or possible.
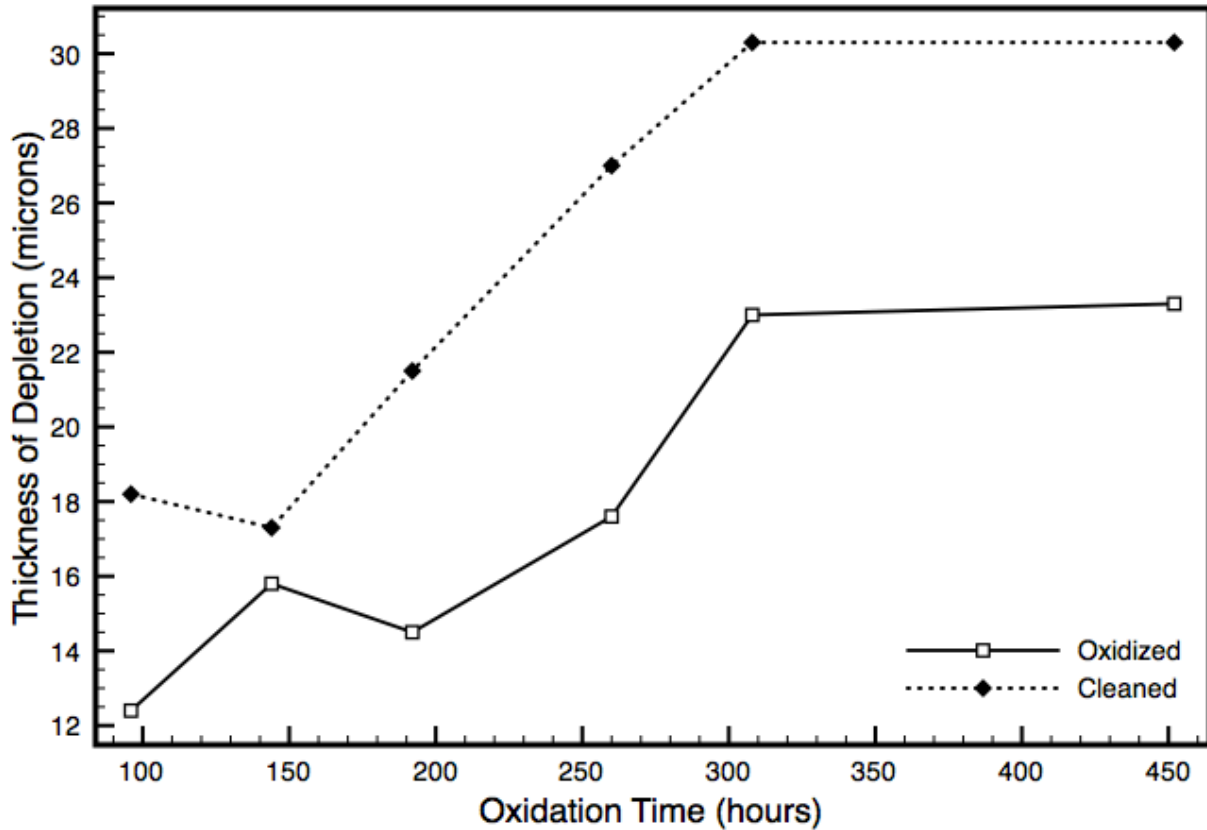
Figure 5.10: The observed depth of depletion of the gamma prime phase on oxidized and cleaned samples with respect to time.

5.2 Discussion

5.2.1 Effects and Effectiveness of the Standard Fluoride-Ion Cleaning Process

The BSE and element mapping images, as well as EDX analysis, presented in this chapter suggest that the standard cleaning process successfully removed the complex multilayer oxide scales from the surface of the GTD111 nickel-based superalloy. Observations supporting this include the relatively homogenous structure seen on the BSE images (see Figure 5.2) and by the complete absence of oxygen in the element mapping and EDX semi-quantitative analysis. Compared to the very complex chemistry of the oxidized samples shown in the previous chapter, samples cleaned via the standard FIC process at Ti Coating exhibited a much more homogenized structure, in terms of the visually and chemically distinct regions observed.

The chemical distribution on the cleaned samples, however, was not completely homogenous, which has also been observed in past studies [1,8,21,22]. Such previous publications observed depletions of aluminum and titanium near the surface of cleaned components, as a result of the movement of aluminum and titanium ions toward the surface of the component to react with the flowing HF gas, in much the same way that the oxides of these elements were formed. The ions of aluminum and titanium were converted to volatile fluorides and were swept from the component and purged from the chamber to maintain the strength of the cleaning process [1]. It is important to mention the inhomogeneities observed in the cleaned GTD111 samples of the current study, as they can potentially affect, in a positive or negative manner, the quality of a repair made by the diffusion brazing process.

Aluminum and titanium exhibited heavy depletion to a depth of 35.5 and 27.2 μm, respectively. This depletion was such that no Al or Ti was detected nearest the surface, indicating that Al and Ti reacted very strongly with the flowing HF gas. The absence of such strong oxide formers near the surface can aid in the prevention of oxidation in the time between cleaning and repairing via ADB, as well as increasing the wettability of the molten filler metal on the substrate surface [1]. It should be noted that the observed depletion was at the upper limit of 30 μm, as specified by the Ti Coating cleaning process [1].

Aluminum and titanium cause hardening in nickel-based superalloys by forming gamma prime precipitates within the matrix. The absence of Al and Ti from the matrix resulted in the absence of gamma prime precipitates to a maximum depth of 31 μm (see Figure 5.10), implying that the region nearest the surface of a cleaned component might be weaker than the bulk material. The question that arises is whether or not this depletion of the gamma prime phase can have an effect on the quality of a repair via ADB. This will be discussed in the next chapter.

A small degree of nickel depletion was observed to a depth of 34.7 μm. This depletion was much less intense than that of aluminum and titanium, and had not been indicated in previous works [1,8,21,22]. Furthermore, the Ti-Coating Technical Report [1] states that attack of the base metal (Ni) is undesirable, and its depletion may suggest that the process was too aggressive. Either the process was allowed to run longer than was necessary to remove the oxide products, or perhaps the HF concentration was too strong. In either case, the current process seemed to be slightly too strong for the oxide formed on nickel-based superalloy GTD111 in the range of 96 to 452 hours, but only in terms of the slight undesirable Ni depletion observed.

The final inhomogeneity observed was the increased level of chromium from the surface to a depth of 23.9 μm, and the subsequent depletion from this level to 38.1 μm. This characteristic of cleaned samples had also not been mentioned in previous studies or other literature concerning the FIC process [1,8,21,22]. The band of chromium depletion occurred in the location of the prior band of chromium oxide, which would suggest the movement of chromium oxide particles to the surface to react with the flowing HF gas, but unlike Al and Ti, the Cr was left within the material, as only the oxygen was reacted away.

The process parameters of the cleaning process can be modified to deplete oxide formers and other alloying elements to a desired depth, as was explained in Section 2.5.2 of the literature review. The HF concentration used in the Ti-Coating Inc. FIC process can range from 5 to 25% in pure hydrogen, and it is possible that the concentration used for this particular trial was not high enough to remove any Cr, and instead, the atoms diffused to the surface upon heating and were trapped within the subsurface of the components. Another possible explanation is that the temperature used for this process may have been too low to cause depletion of the Cr atoms, as only the temperature range of 900 to 1100°C was found in literature, due to the proprietary nature of the process [1].

The depletion of aluminum and titanium have been said to be beneficial as the absence of strong oxide formers helps to prevent future oxidation [1]. However, chromium is also a strong oxide former, and its presence in high amounts near the surface of a component may affect the ability of the diffusion brazing repair process by the formation of oxide compounds.

5.2.2 Thickness of Depleted and Oxidized Regions

Figure 5.10 showed the thickness of gamma prime depletion observed on oxidized and cleaned samples. Again, as expected, the cleaned samples consistently exhibited greater gamma prime depletion than their respective oxidized samples, indicating that the cleaning process caused further elemental depletion than was experienced during the formation of the oxide scales. This can be attributed to the fact that the surface and subsurface scales on oxidized samples, after longer oxidation times, acted as barriers to metal ion diffusion, and slowed the rate of elemental and phase depletion. On the other hand, the cleaning process removed the oxide scales, and the rate of elemental and therefore gamma prime phase depletion was again increased, resulting in "over-cleaning" by further depleting the strong oxide-formers of Al and Ti and therefore the gamma prime phase.

The thickness of gamma prime phase depletion on both oxidized and cleaned samples was found to increase, in general, with increased oxidation time, to a maximum of 23 and 31 μm, respectively. However, the gamma prime depletion curves in Figure 5.11 did not show an increase in thickness after 308 hours. The gamma prime depletion had not been analyzed in past oxidation or cleaning studies, but it is an important characteristic to study, as the depletion of this strengthening phase could have deleterious effects on the strength of a component if it is not restored during the repair process. It was explained in the above paragraph that the gamma prime depletion on oxidized samples is eventually halted due to the formation of protective oxide scales. However, on cleaned samples, the absence of oxide scales meant that this phase depletion happened much faster and possibly for a longer time. There must be a point in the cleaning process where the rates of elemental depletion within the sample and the removal of elements from the surface balance, therefore halting further depletion of the gamma prime phase.

5.2.3 Effect of Oxidation Time on the Chemistry and Elemental Depletion of Cleaned Samples

According to Figures 5.8 and 5.9, the concentrations of the main alloying elements and nickel with respect to time for depths of 5 and 40 μm showed only very small variations in composition. This implied that the resultant chemistry of samples cleaned by the FIC process was not dependent on the chemistry of the prior oxidized structure.

This observation suggests that any level of oxidation within the scope of this study – that is, from 96 to 452 hours – may have the same effect on the chemistry of a sample repaired by the diffusion brazing process, and that neither the cleaning nor the brazing process need be customized for the duration of oxide formation. Therefore, diffusion brazing parameters can be adjusted based on notch geometry, but may not need to be adjusted to deal with varying oxidation times.

5.3 Summary

The results presented in this chapter have shown that the FIC process was capable of removing the oxide compounds formed for up to 452 hours, and that the depletion of Al and Ti was observed. However, the slight depletion of Ni and a region high in Cr were also observed near the surface of cleaned samples. The prior oxidation time had little to no effect on the chemistry of cleaned samples, although the thickness of elemental and gamma prime depletion was observed to change with increasing oxidation time. The gamma prime depletion was observed to reach a limit after 308 hours.

The following chapter presents the results of performing activated diffusion brazing on 1 mm notches in GTD111 using different viscosities, mixing ratios, and amounts of pre-placement, to determine the resultant porosity of the braze-repaired region. Also, the braze-repaired region and surrounding base metal will be analyzed via SEM-EDX and element mapping to understand how the chemistry after brazing depends on the chemistry observed after the FIC process.

Chapter 6 Preliminary Brazing Trials

The Activated Diffusion Brazing (ADB) process is widely used as a means of restoring damaged nickel-based superalloy components to their original shape and functionality. The two previous chapters have shown the effects of the processes of high-temperature oxidation and fluoride-ion cleaning on the chemistry of the nickel-based superalloy GTD111. In this chapter, ADB has been performed on pre-notched samples of GTD111 to understand how the chemistry observed after the fluoride-ion cleaning process affects the chemical distribution within a component repaired via ADB, as well as the effects of mixing ratio and paste viscosity on the quality of the repaired region.

6.1 Experimental Procedure

Three preliminary brazing trials were performed on pre-notched samples of GTD111. The same heating schedule was used for all three samples, in which a holding time of 65 minutes was employed at the bonding temperature of 1220°C. Bond-stop was brushed on all samples prior to filling the notches with paste, and all samples were over-packed at the top to account for flow into the notch tip and shrinkage during solidification.

6.1.1 Brazing Trial 1

The first brazing trial was performed on a 1 mm-wide notch using a mixing ratio of 50% base metal powder to 50% filler metal powder (FMP), and the paste was made using approximately 11% binder by weight. This created a fairly thick mud-like paste, which was packed into the sample using a small spatula. This selection of process parameters was chosen to determine if a mixing ratio with more than 40% FMP could flow easily into the tip of the simulated notch, even with a high-viscosity paste.

6.1.2 Brazing Trial 2

The second brazing trial was performed on 1 mm- and 3 mm-wide notches using a mixing ratio of 60% base metal powder to 40% filler metal powder, and the paste was made using approximately 14% binder by weight. This created a much more fluid paste than was used for brazing trial 1, which was packed into the sample using a small spatula. This trial would rely more on the fluidity of the low-viscosity paste than on the fluidity of a paste with a higher amount of FMP.

6.1.3 Brazing Trial 3

The third brazing trial was performed on a 1 mm- wide notch using a mixing ratio of 60% base metal powder to 40% filler metal powder, and the paste was made using approximately 12% binder by weight. This created a paste with a viscosity between those used for brazing trials 1 and 2. In order to better simulate the repair process on a full component, a piece of GTD111 was placed on each end of the notch, and wire was used to secure the plates in place. This would prevent flow of the filler metal from the ends of the notch. In this trial, a mid-range viscosity was coupled with the best possible paste pre-placement.

6.2 Results

6.2.1 Photos Upon Removal from Furnace

6.2.1.1 Brazing Trial 1

The final product of the first brazing trial showed only a slight amount of flow onto the sides and top, suggesting that the bond-stop had performed its intended purpose of keeping the brazing alloy melt from running off of the sample. Photographs of the exterior and cross-sections of the first brazing trial sample are shown in Figure 6.1.

(a)   (b)
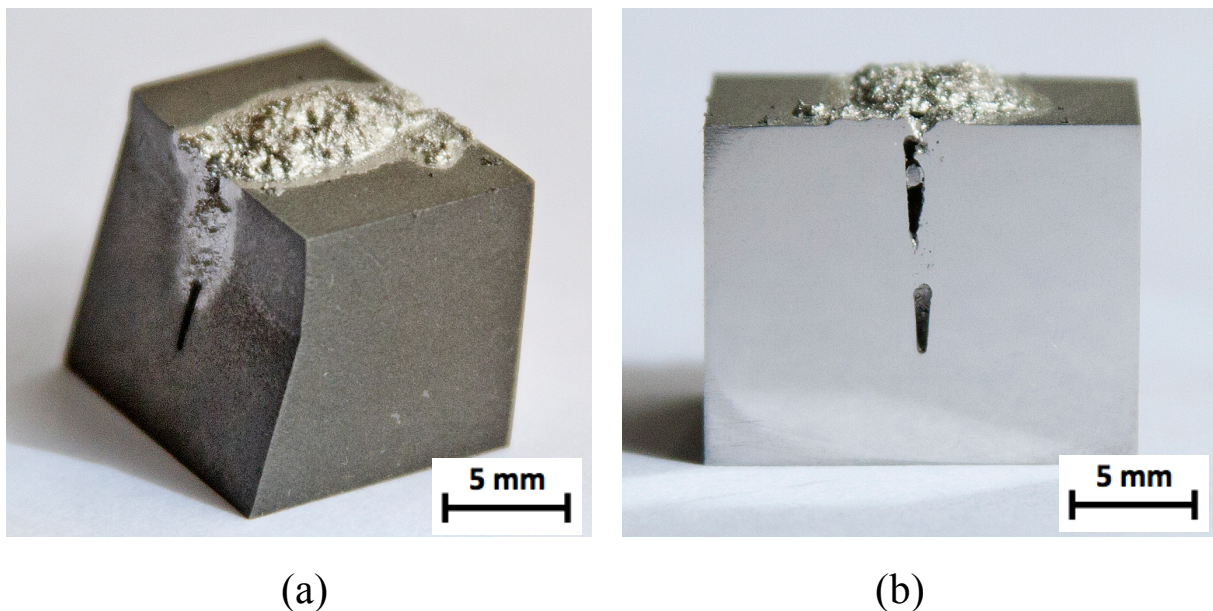
Figure 6.1: The first brazing trial sample: (a) after removal from the furnace and (b) a cross-section which showed incomplete filling.

The first brazing sample was not successfully repaired, since the damaged area was not completely filled. This incomplete filling could have been the result of incomplete paste pre-placement or an insufficient amount of binder, resulting in a paste too thick to achieve adequate flow into the notch tip.

The issue of incomplete packing can be overcome by continually pushing the paste into the notch tip, but complete pre-placement is difficult to ensure. Also, choosing the correct paste viscosity can make the workability and pre-placement of the paste much easier. The issue of viscosity can be more easily addressed, as the amount of binder used to create the paste can be easily changed. The first brazing trial sample showed that more binder should be used in order to create a more fluid paste.

6.2.1.2 Brazing Trial 2

The final products of the second brazing trial have been shown in Figure 6.2. On the left is the 3 mm notch, showing almost no filling, since most of the filler metal mixture had flowed from the notch during brazing, suggesting that the bond-stop could not control the flow of so much molten metal. Figure 6.2 (b) shows the 1mm sample brazed with a less viscous and more tightly-packed paste than was used for the first brazing trial, also showing a large amount of flow out of the tip of the notch.

(a)   (b)
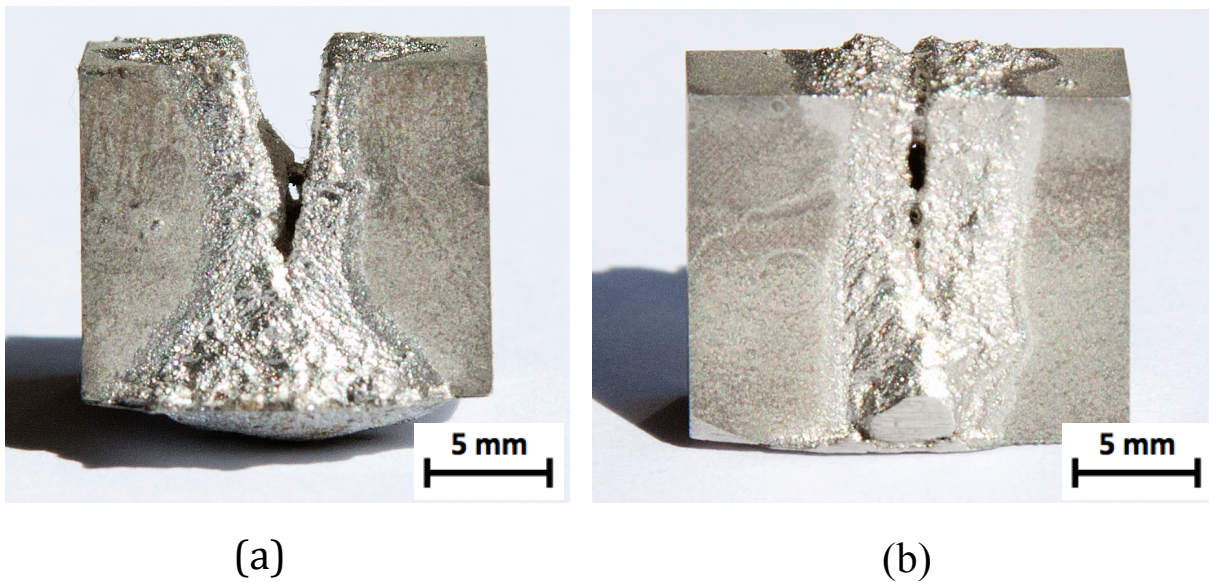
Figure 6.2: (a) 3 mm and (b) 1 mm samples from the second brazing trial.

More complete filling was achieved than in the first trial, although the top of the notch was still under-filled. There appeared to be a large amount of material that had flowed out of the notch tip on both samples. Although a difference of only 3% binder may have seemed like a small amount, it had a large effect on the resultant paste viscosity and pre-placement in the notch. In the first brazing trial, 11% binder created a paste that was much too thick to be easily applied to all areas of the notch, but the second brazing trial showed that 14% binder might have been too fluid, as some of the paste was seen to be leaking from the notch tip before the paste had dried.

Since the 3 mm sample was almost completely unfilled, it was not analyzed further, and only the 1 mm sample will be analyzed for the remainder of this section. Figure 6.3 below shows a photograph of a cross-section taken near the edge of the sample.
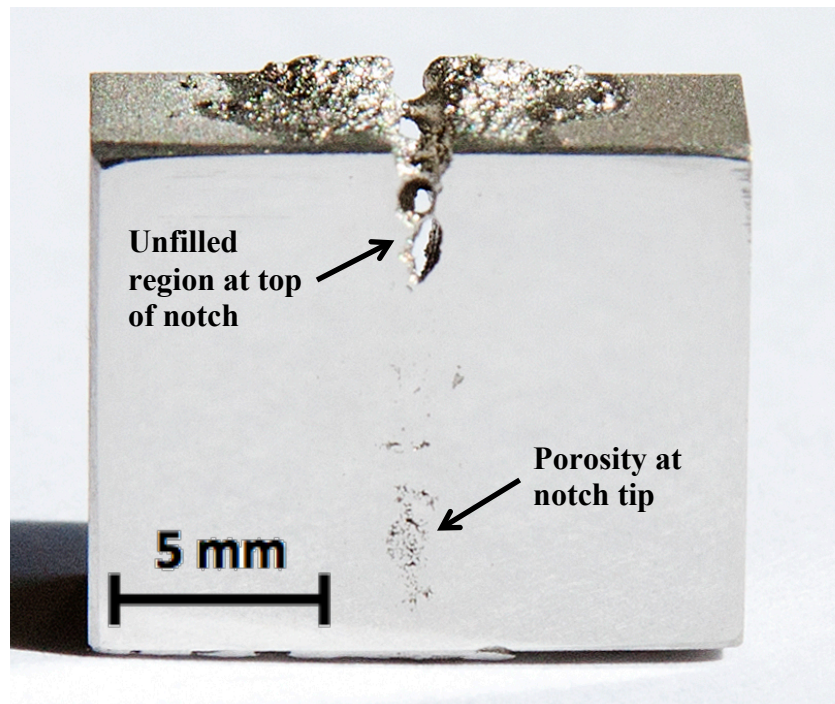
Figure 6.3: A cross-section of the 1 mm sample of the second brazing trial.

Almost complete filling was achieved in this region of the sample, with the exception of the top 2 mm, and the porosity observed near the tip of the notch, as shown in Figure 6.3. The increased filling achieved on the second brazing trial sample implied that a paste with lower viscosity was preferred to a paste containing more FMP, in terms of the ability to easily fill or flow into the tip of a simulated notch.

6.2.1.3 Brazing Trial 3

The third brazing trial was packed more tightly than the previous two trials, and pieces of oxidized GTD111 were placed at the ends of the notch to maintain as much filler material as possible within the notch. A photograph of the cross-section of the third brazing trial sample is shown in Figure 6.4.
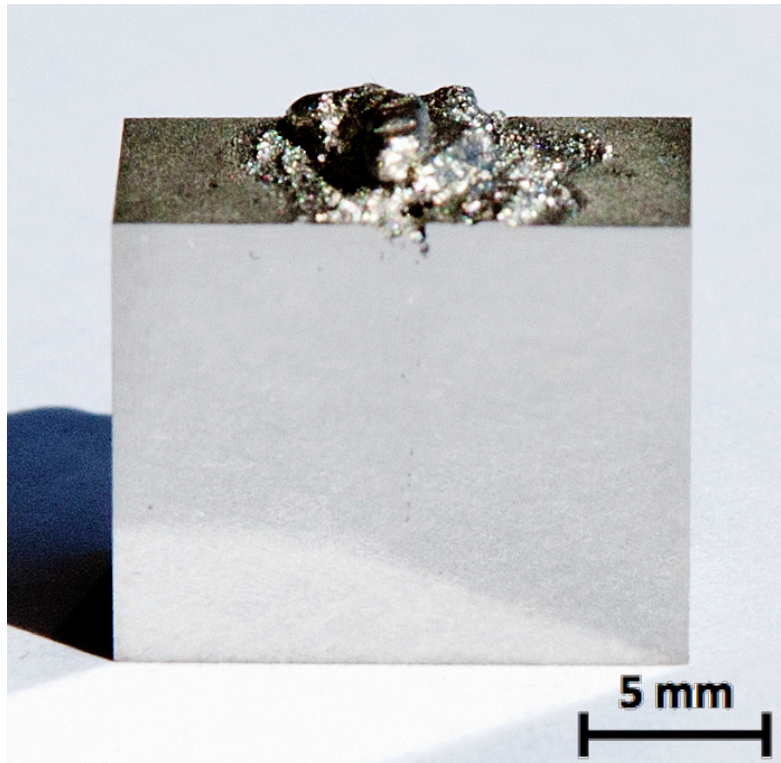
Figure 6.4: Cross-section of the third brazing trial sample.

The third brazing trial exhibited the best filling of any trial thus far, as complete filling of the notch occurred, and no porosity was observed in the cross-section.

6.2.2 Back-Scattered Electron Images of Braze-Repaired Regions

6.2.2.1 Brazing Trial 1

Back-scattered electron imaging showed that there was successful brazing in the filled region of the first brazing trial, even though the repair as a whole was unsuccessful due to incomplete filling. That is, there were only small traces of an interface separating the inside of the notch from the bulk material, and the microstructure looked very similar in the two regions, as seen in Figure 6.5.
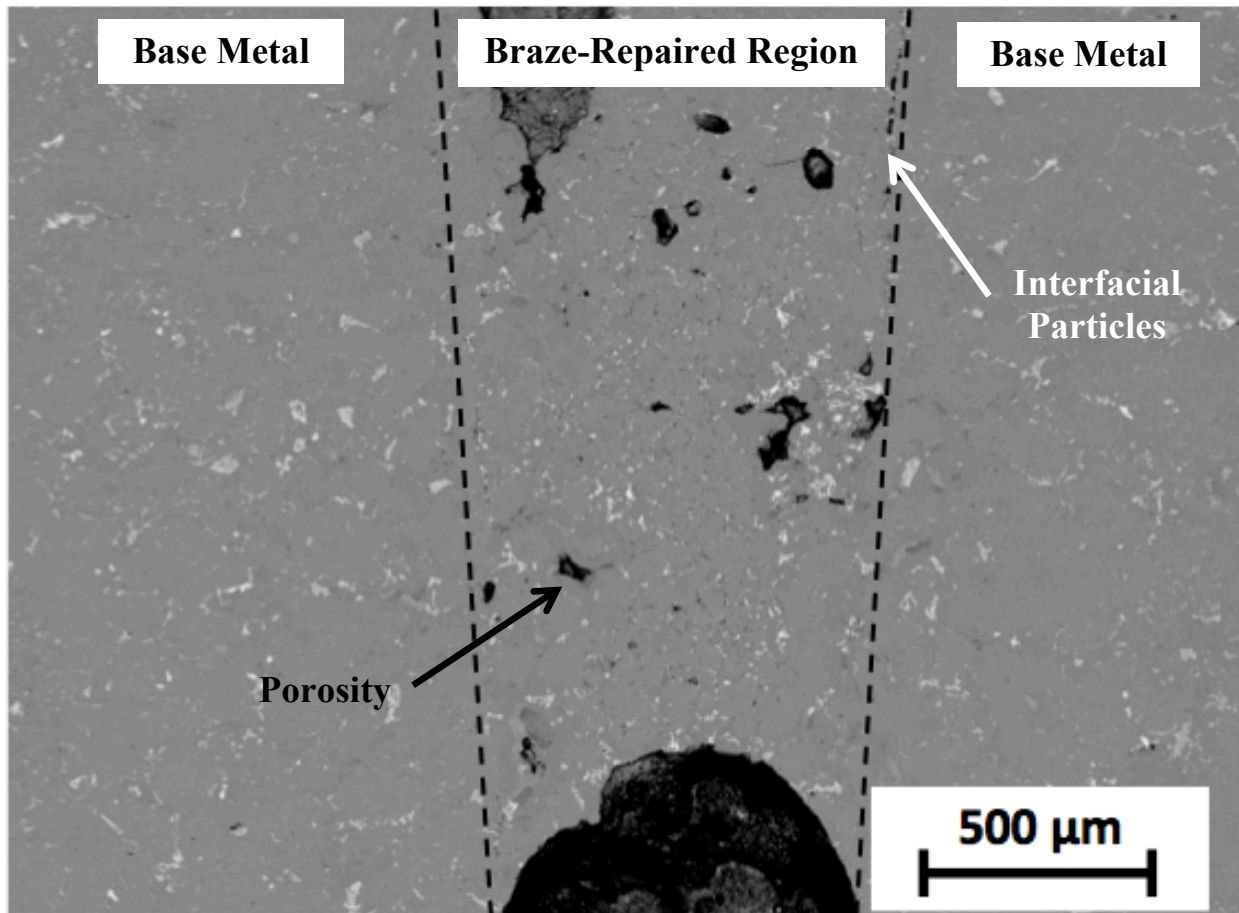
Figure 6.5: BSE image of the braze-repaired region of the first brazing trial sample.

Examination of Figure 6.5 showed that there were some defects within the braze-repaired region. There was a good deal of porosity within the filled region, as indicated by the black arrow in Figure 6.5. There were also small areas within this region that showed evidence of a prior interface. These regions appeared as groups of connected black particles on the inside of the interface lines drawn on in Figure 6.5, and are indicated by a white arrow. The interfacial region has been magnified in Figure 6.6 below. The concentrations of small dark particles at some locations along the prior interface suggested that a fully homogenous bond had not been produced.
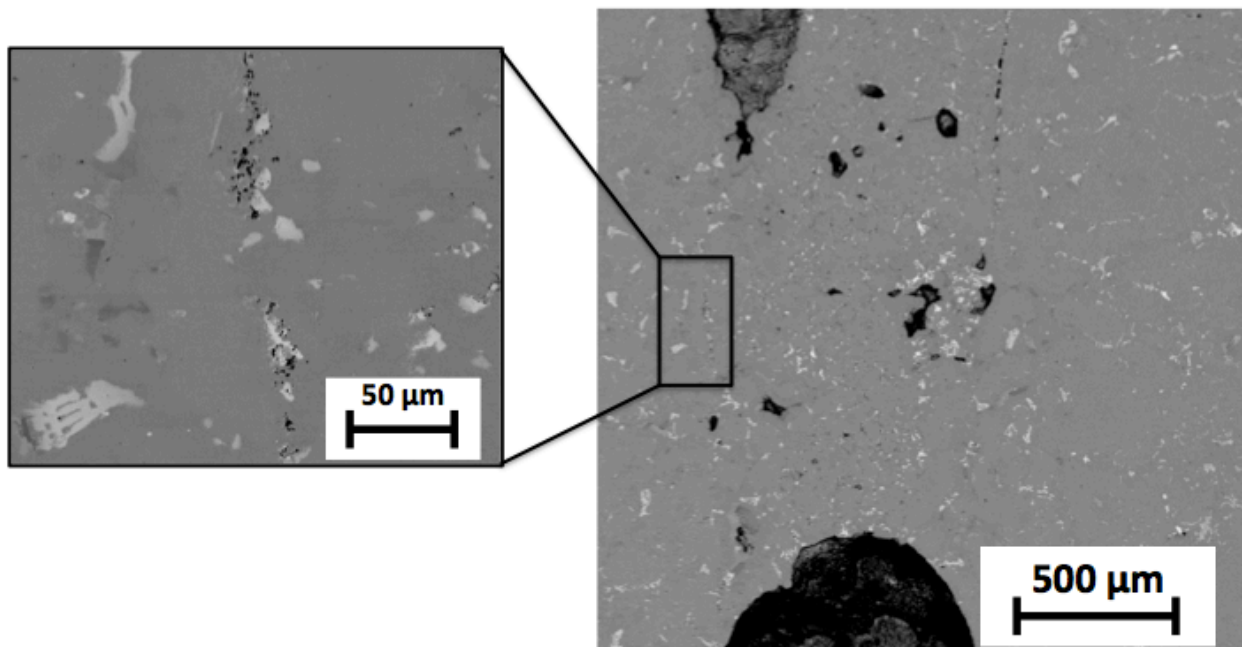
Figure 6.6: A magnified view of the interfacial particles observed in the third brazing trial sample.

The BSE image shown in Figure 6.6 could only show the presence of the interfacial particles, so it was necessary to perform chemical analysis to determine if the particles were intermetallics from the brazing process or oxides from the surface formed before or during the brazing process. Element mapping in Section 6.2.3.1 was used to determine the main elements present in the interfacial particles.

6.2.2.2 Brazing Trial 2

Back-Scattered Electron images were taken of the repaired notch and surrounding base metal on the second brazing trial. Figure 6.7 shows that the second brazing trial sample exhibited a clear difference between the filled notch and the adjacent metal – herein referred to as the diffusion-affected zone – which was affected by the diffusion of material from the braze-filled region into the base metal.
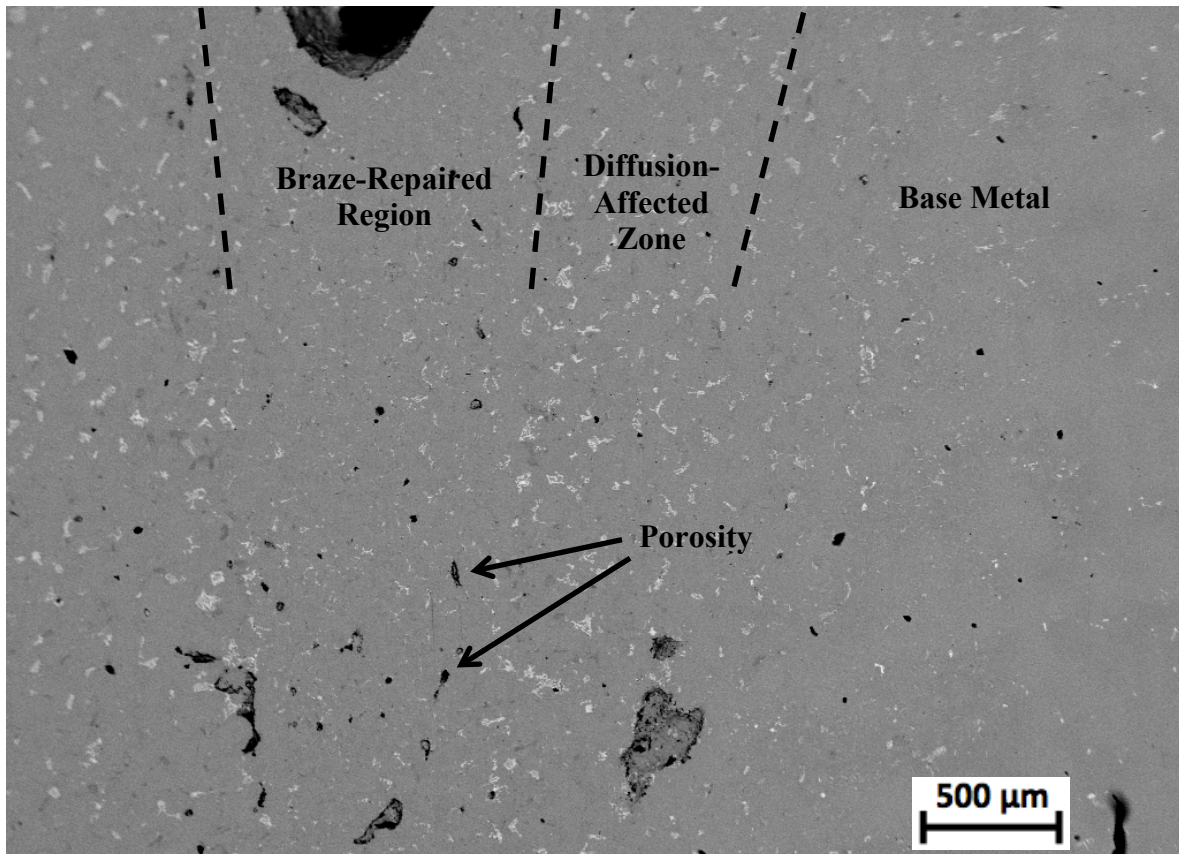
Figure 6.7: The top of the filled region of the second bonding trial sample.

Clear differences were observed between the structure of the braze-repaired region and the diffusion-affected zone. The braze-repaired region contained far fewer white secondary phases than the diffusion-affected zones on either side, which were found to be approximately 700 μm in width. Beyond this region was unaffected base metal, which the filled region of the notch very closely resembled. There was still some porosity observed within the braze-repaired region, although the size and quantity of pores was much less than those observed on the first brazing trial sample, suggesting the benefit of using a less viscous, more well-packed paste. No interface was observed on the second brazing trial sample. With the exception of the apparent inhomogeneity of phase distribution and the presence of some porosity, there was essentially no visible barrier between the filled notch and the substrate. Recall that there were small oxide particles present at the interface of the first brazing trial, but such phases were not observed on this sample. Figure 6.8 shows a magnified BSE image of the diffusion-affected zone, showing the different phases present.
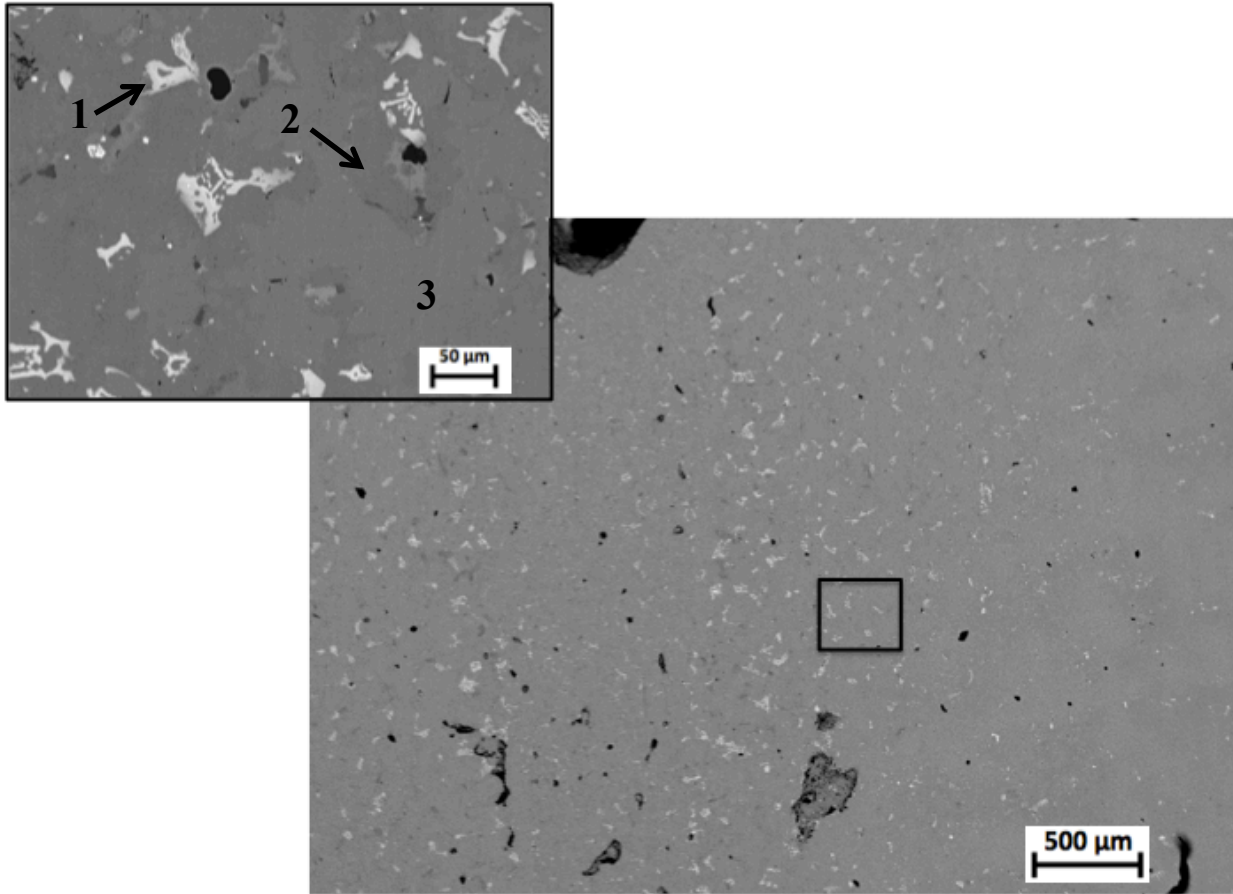
Figure 6.8: Magnification of the diffusion-affected region of the second brazing trial sample, containing many distinct phases.

Clearly, many different phases were present in this region, as indicated by the various shades seen in different regions. For example there were very bright islands (location 1) surrounded by a phase slightly darker (location 2) than the remainder of the material (location 3). Given that this is a BSE image, elements with lower atomic mass appeared brighter, and the darker phases corresponded to elements with higher atomic mass. However, chemical analysis is required to learn more about the different phases observed. Element mapping of this region is shown in Section 6.2.3.

6.2.2.3 Brazing Trial 3

Back Scattered Electron images of the top and bottom of the notch, exhibiting interfacial particles (black arrow) and slight porosity (white arrow) have been shown in Figure 6.9.
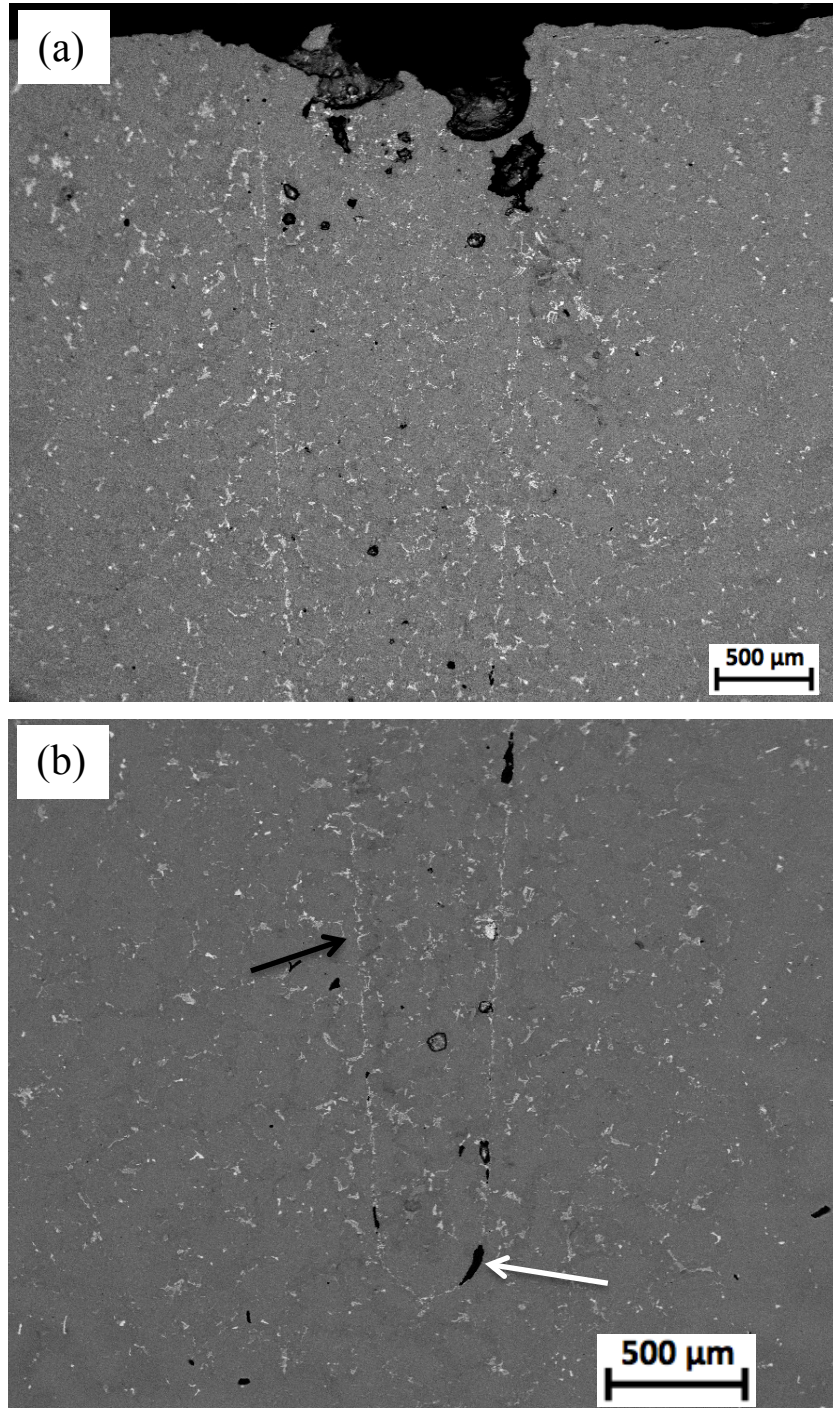
Figure 6.9: BSE images of: (a) the surface and (b) the tip of the notch repaired during the third brazing trial.

Of all the brazing trials, this sample exhibited the most obvious interface. However, unlike the first brazing trial, which showed small amounts of dark interfacial particles – suggesting the presence of elements with low atomic mass such as O or B – the third brazing sample showed large amounts of bright interfacial particles. The high atomic mass of this phase suggested the presence of heavy elements, and not that of harmful intermetallics. This sample also showed the least porosity and best filling of all brazed samples.

Recall that the second brazing trial sample exhibited a very distinct region high in heavy-element phases adjacent the prior substrate surface. The sample from the third brazing trial showed a slight increase in this phase near the interface, but it was not nearly as wide or distinct as in the previous sample. Also, as was the case for the two previous brazing trials, a very similar microstructure was observed in the notch and the base metal to the far right of Figure 6.9 a.

A magnified view of the interface further demonstrated the presence of heavy-element phases as the interfacial particles.
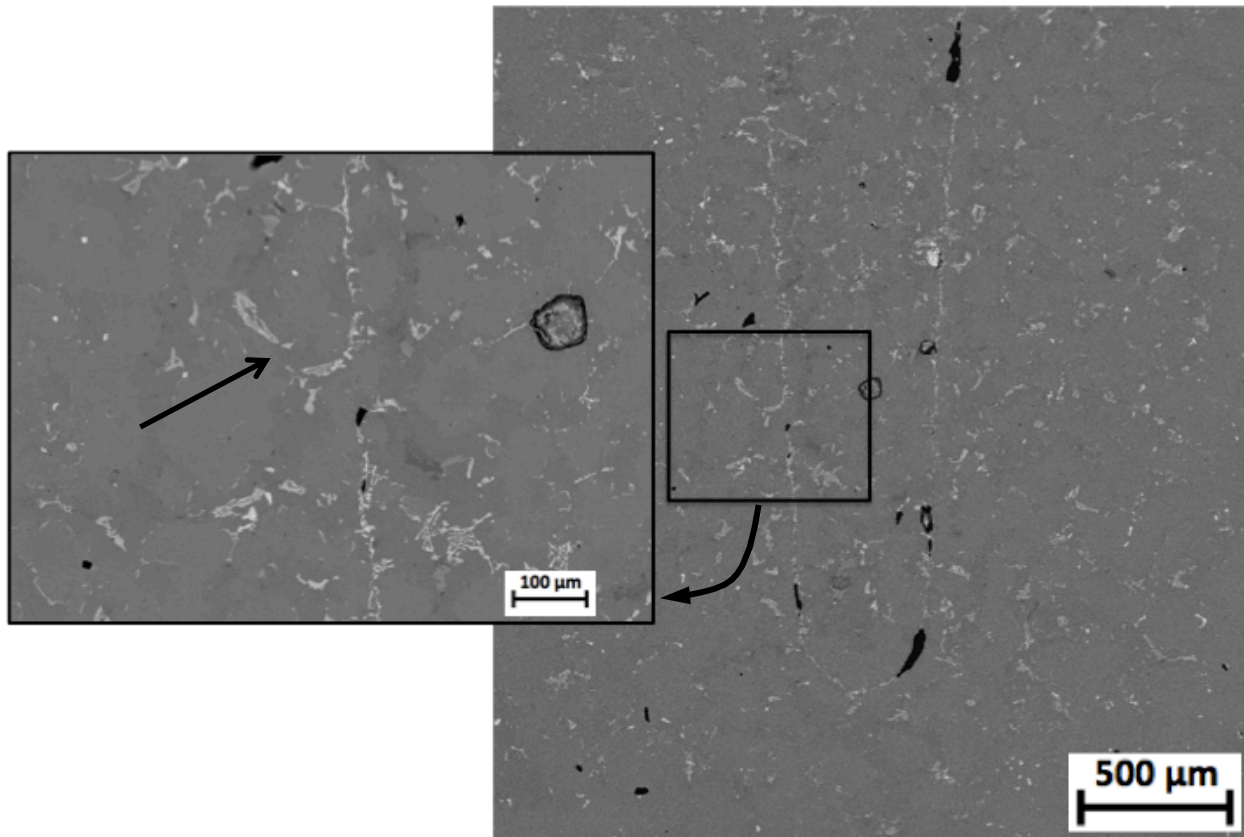
Figure 6.10: A magnified view of a portion of the interface observed on the third brazing trial sample.

There were some small areas where the particles at the interface had broken up, such as the hook-like region of particles observed in Figure 6.10, which seemed to be diffusing toward the base metal. This image has captured the motion of the interface during the homogenization stage of the diffusion brazing process, and sufficient holding times might have eliminated this interface altogether.

6.2.3 Elemental Distribution Within Braze-repaired Samples

6.2.3.1 Brazing Trial 1

Element mapping was performed at 50X magnification to determine if any obvious chemical differences stood out between the filled region and the base material. Figure 6.11 below shows a BSE image and element maps for chromium (green), tungsten-tantalum (purple), titanium (yellow), aluminum (blue), and nickel (red) in the braze-repaired region and adjacent base metal of the first brazing trial sample.
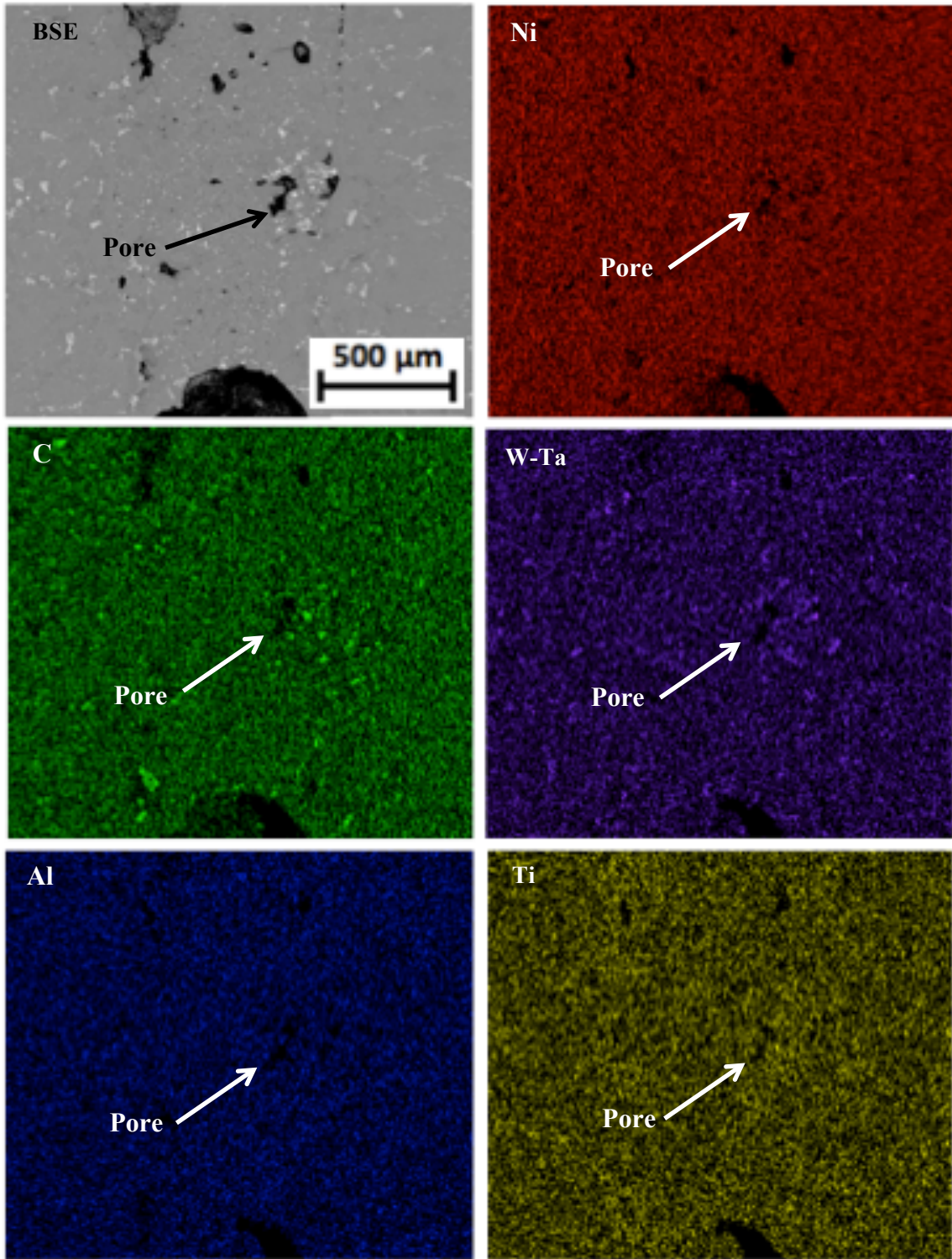
Figure 6.11: Element mapping performed at 50X magnification on the first brazing trial sample.

Element mapping at this level showed that there were essentially no obvious concentrations of any of the elements within the braze-repaired region. The only concentrations that really stood out were contained within the bright regions, which were high in the alloying elements of chromium, tungsten-tantalum, and to a much smaller degree, titanium. The only obvious difference between the filled region and the bulk material, from this magnification, was the porosity within the filled region. This porosity was seen as fairly large black regions in both the BSE image and in every element map in Figure 6.11. An important note is that the depletions of Al and Ti that resulted from the FIC process were not observed near the interface of this sample, suggesting the effective diffusion of these elements during the diffusion brazing process. Figure 6.12 below shows the results of element mapping performed at 500X magnification, along with a BSE image, to identify the dark interfacial particles.
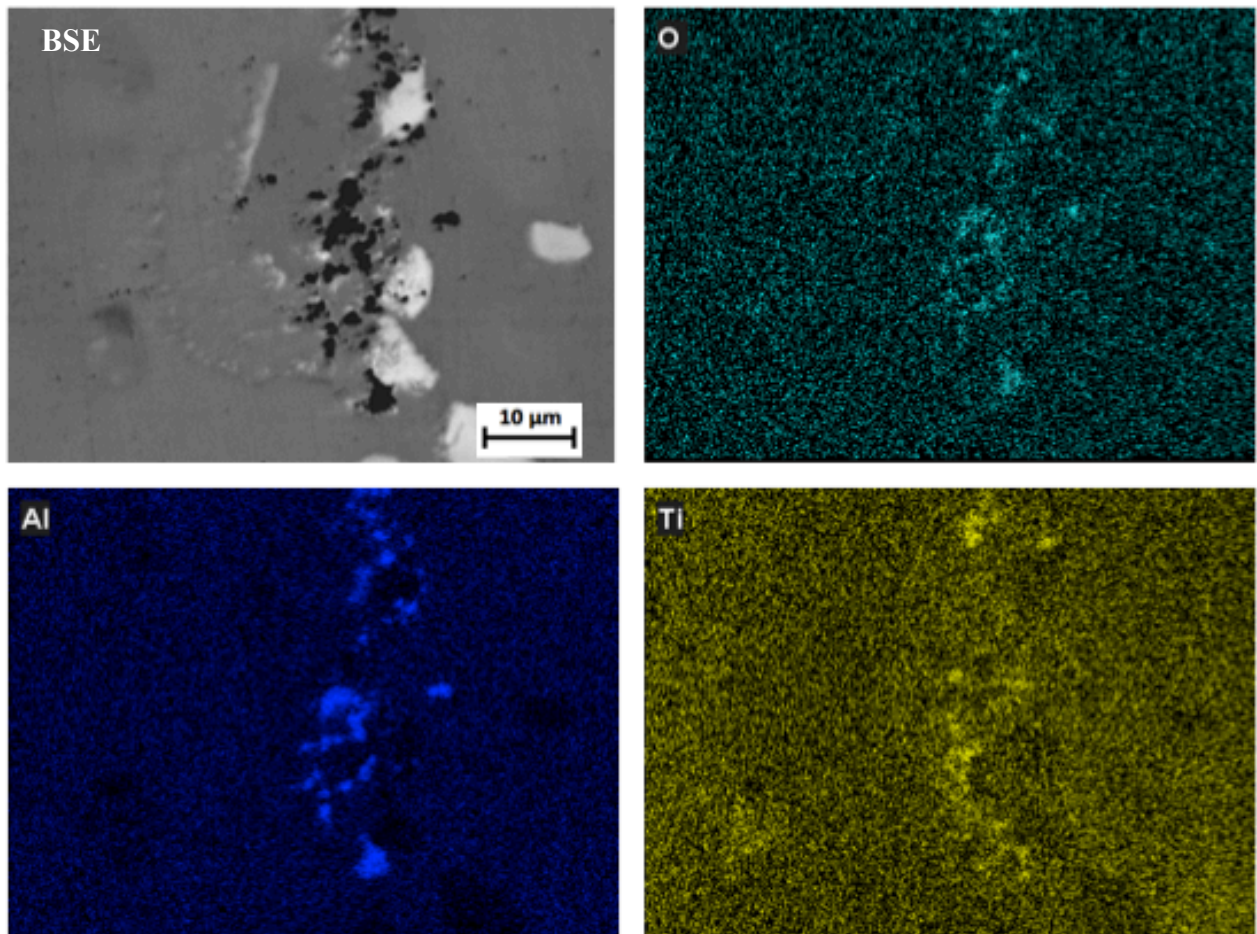
Figure 6.12: Element mapping on the interfacial particles of the first brazing trial sample.

The particles along the interface were shown via element mapping to contain aluminum, titanium, and oxygen, and so it was concluded that the interfacial particles were oxides which may have formed in the initial stages of brazing, as incomplete filling could have resulted in unprotected substrate surfaces that may have oxidized if the vacuum level was insufficient.

6.2.3.2 Brazing Trial 2

Similar to the first brazing trial, element mapping was performed at low magnification (25X) to show that no depletions or concentrations of elements occurred near the previous notch surface. Figure 6.13 below shows the low-magnification element maps for the second brazing trial.
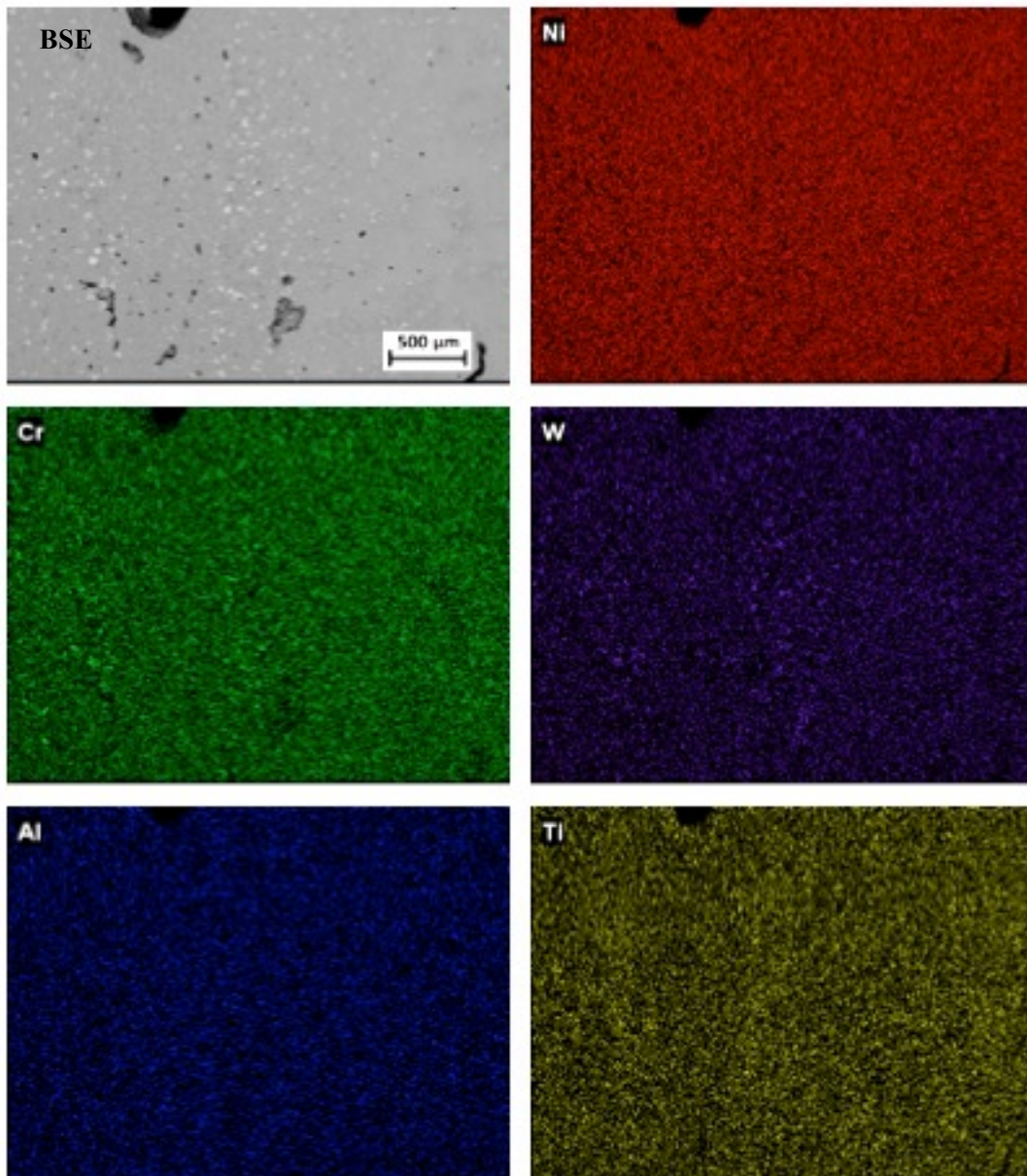
Figure 6.13: Element mapping performed at 25X magnification on the second brazing trial sample.

Recall that after oxidation and cleaning had taken place, a region depleted in Al and Ti was observed within the immediate subsurface of the samples. However, the above element mapping did not show any such depletion, as the levels of Al and Ti in Figures 6.11 to 6.13 were the same throughout the analyzed regions. Since the Al and Ti had returned to the interfacial region, it was decided to determine if depletion of the gamma prime phase was still present in this area. Optical microscopy was used on the second brazing trial sample etched with Marble's reagent to reveal any potential gamma prime depletion. Figure 6.14 below shows an optical micrograph of the second brazing trial sample, where the prior interface has been indicated by the red dashed lines. If depletion of the gamma prime phase were still present, the region surrounding the prior interface would appear bright, as those observed around the notches of the oxidized and cleaned samples in Section 5.1.1.
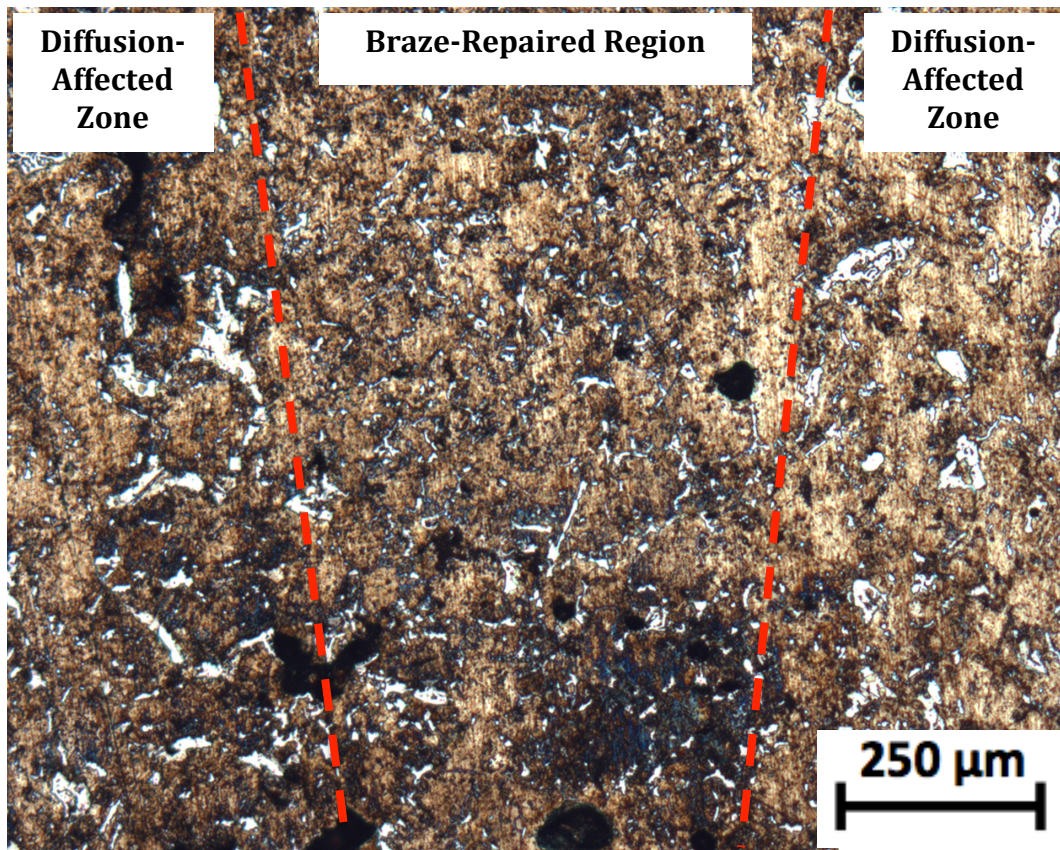
Figure 6.14: Optical micrograph showing the absence of gamma prime depletion between the brazed region and diffusion-affected zones of the second brazed sample.

Since no depletion of the gamma prime phase was observed through optical microscopy, it was concluded that the ADB process had successfully restored the strengthening phase to the interfacial regions of the braze-repaired samples. Figure 6.15 shows the element maps taken at 300X for Cr, W-Ta, Ti, Al, and Ni, in order to identify the elements that contributed to the various phases observed in the interfacial region.
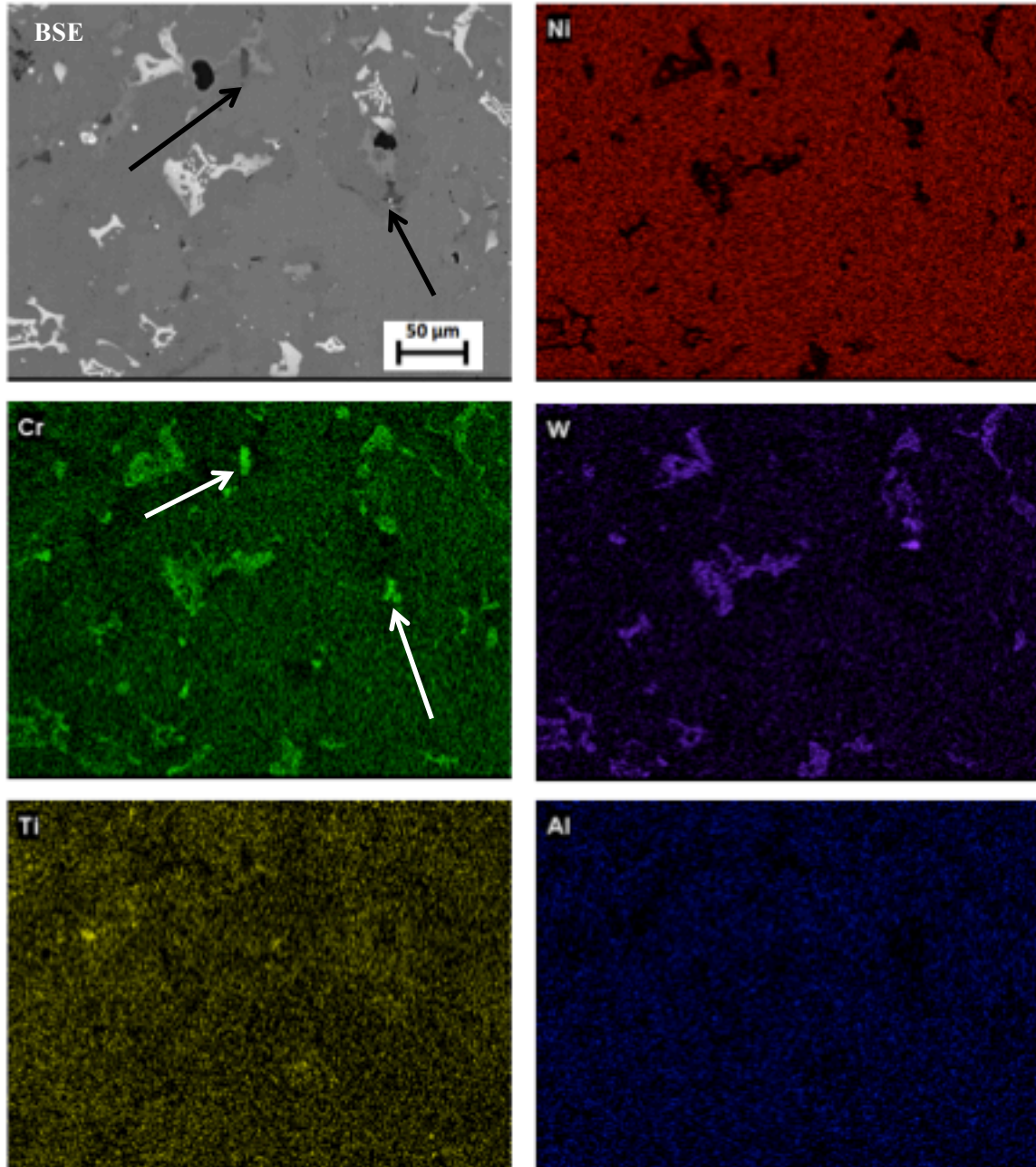
Figure 6.15: Element mapping at 300X on the diffusion-affected zone of the second brazing trial sample. The arrows in the Cr element map (a) and the BSE image (b) indicate the presence of an intermetallic compound such as a boride.

The white phases were found to contain heavier elements such as Cr and W-Ta. Although the element was not shown, Mo was also detected in higher concentrations in this phase. Although small concentrations of Ti were observed, they were found in the semi-dark regions surrounding the white heavy-element phases, and have been indicated by the arrows on the Ti element map in Figure 6.15. Aluminum and nickel did not seem to concentrate in any region of the sample. One important observation was the presence of the dark phases – but not the black phases – that were observed in small quantities, highlighted in the Cr element map and BSE image of Figure 6.15. These phases were very high in Cr and have been indicated on the Cr element map. As Cr is a heavier element, the darkness on the BSE image indicated that a very light element was also involved. This could perhaps have been the result of boron from the FMP forming an intermetallic compound with Cr, and which had diffused out of the prior notch as is desired in the diffusion brazing process. However B was not mapped because it is not easily detected by EDX analysis, and Auger spectrometry could be used to verify the chemistry of this region; however, it is outside the scope of this study.

6.2.3.3 Brazing Trial 3

Figure 6.16 below shows the results of element mapping performed on the third brazing trial. Again, no obvious chemical differences were observed within the repaired sample, as no depletions or concentrations were observed in any region of the braze-repaired sample, as indicated by the even distribution throughout all of the element maps.

The chemical homogeneity observed in the element maps of the three brazing trial samples (Figures 6.11, 6.13, and 6.16) suggested that the diffusion brazing process was able to restore the chemistry surrounding the previous notch surfaces to that observed in the base metal. That is, the depletions and concentrations of elements such as Al, Ti, Ni, and Cr were no longer observed on the braze-repaired samples. However, in order to ensure that chemical homogeneity had in fact been restored, it was necessary to perform EDX analysis in each of the three distinct regions observed; the braze-repaired region, the diffusion-affected zone, and the base metal.
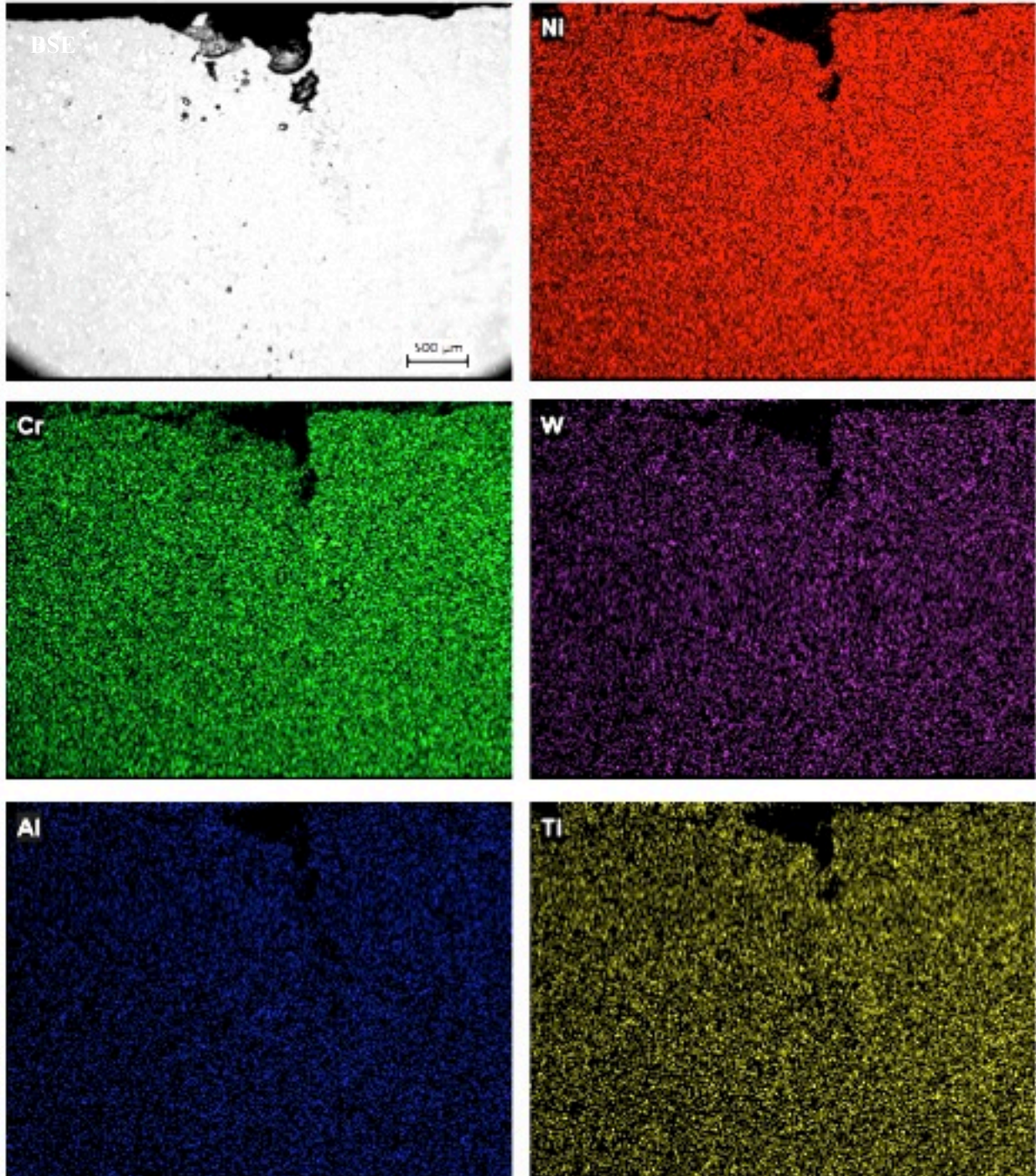
Figure 6.16: Element mapping performed at 25X magnification on the third brazing trial sample.

6.2.4 EDX Analysis

6.2.4.1 Brazing Trial 2

Considering the slight inhomogeneities and the apparent differences in structure observed between the braze-repaired region and the area adjacent the prior substrate surface, EDX analysis was performed on five small areas, according to Figure 6.17, to determine any compositional differences between the braze-repaired, diffusion-affected, and base metal regions. The results of EDX analysis are shown in Table 6.1.
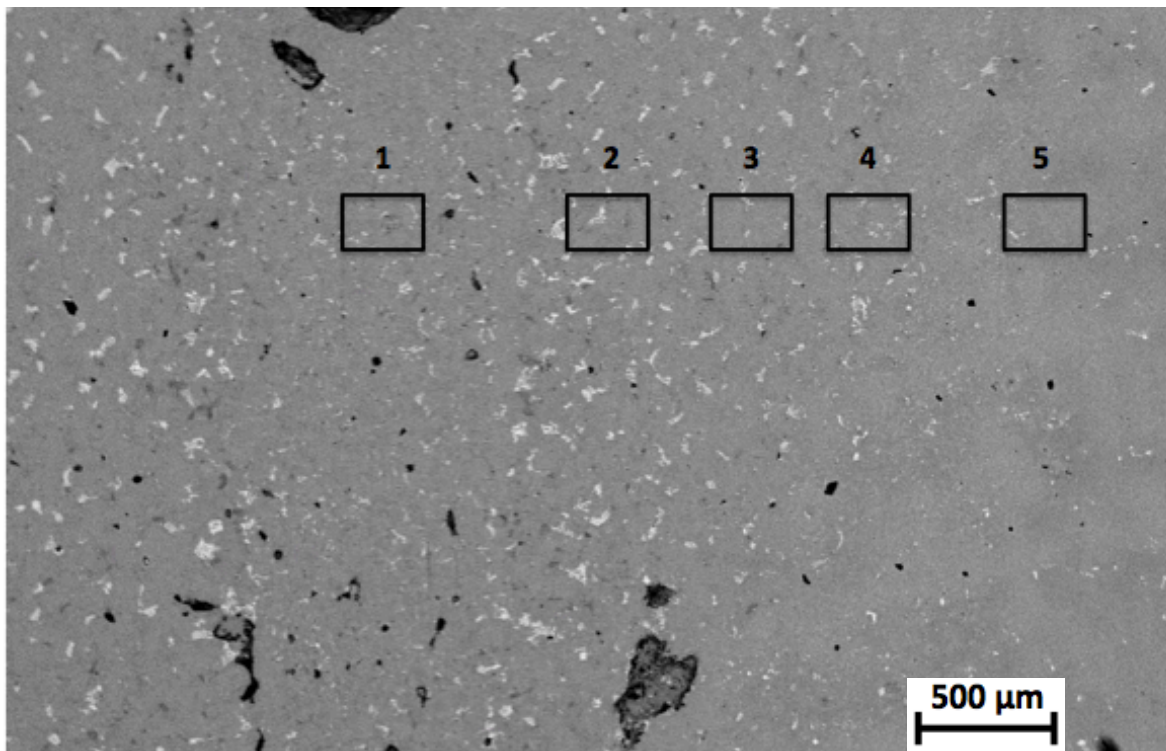
Figure 6.17: Locations of EDX analysis within the braze-repaired, diffusion-affected, and base metal regions of the second brazing trial sample.

Table 6.1: EDX results* for the second brazing trial sample compared to the nominal GTD111 composition [34].

Region	Al	Ti	Cr	Co	Ni	Mo	W	Ta
1	4.0	3.2	13.0	9.3	64.3	0.9	4.6	1.2
2	3.6	5.1	11.3	9.2	65.1	0.6	2.8	2.0
3	3.8	3.4	12.9	9.5	64.0	1.0	4.1	1.5
4	3.3	3.8	13.1	10.2	63.6	0.9	3.4	1.7
5	3.2	4.3	13.6	9.4	62.9	1.3	3.6	1.8
NOMINAL	3.1	4.9	14.0	9.5	61.0	1.5	3.8	2.8

* All values are given in weight %

Essentially no differences in chemistry were observed between the five analyzed areas. The composition of each area, regardless of the presence or absence of the white heavy-element phases, was essentially the same. Recall that prior to the diffusion brazing process, there were strong depletions of Al and Ti, as well as an obvious increase in Cr concentration, close to the surface of the cleaned samples. However, after the diffusion brazing repair process, the depletions and concentrations seemed to have been corrected through the homogenization of the chemistry, which was also observed in the element mapping of Section 6.2.3.

6.2.4.2 Brazing Trial 3

Figure 6.18 shows the nine areas of approximately 300 μm in width and 3 mm in length that were analyzed using EDX analysis, starting at the base metal to the left of the brazed notch, and Table 6.2 summarizes the average composition of each distinct region – base metal, diffusion-affected zone, and braze-filled region – of the sample.
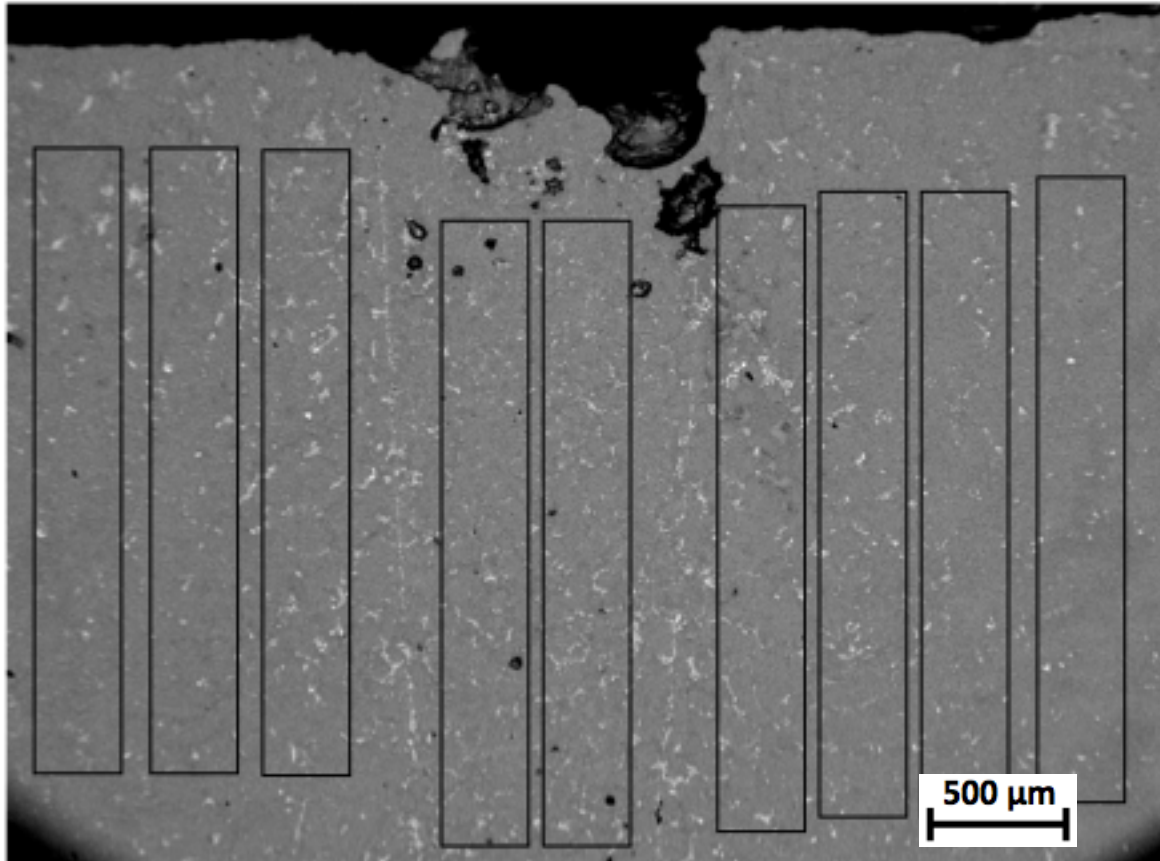
Figure 6.18: Locations of EDX analysis performed across the cross section of the third brazing trial sample.

Table 6.2: EDX results* for the third brazing trial.

Region	Al	Ti	Cr	Co	Ni	Mo	W	Ta
Base Metal	3.0	4.4	13.2	9.7	62.3	1.1	4.0	2.5
Diffusion-Affected	3.2	3.9	13.8	9.6	62.1	1.1	4.5	1.8
Braze-Repaired	3.5	4.0	12.7	9.6	63.0	0.9	4.1	2.3

* All values are given in weight %

As was the case with the second brazing trial, only very slight changes in chemistry were observed as the sample was analyzed from left to right. This suggests that the diffusion brazing process, even if it displayed an obvious interface, had the ability to create a microstructurally – and even more so chemically – homogenous repaired structure. The EDX results supported the element maps' suggestion that the chemistry near the surfaces of the substrate resulting from the prior cleaning process did not have an effect on the chemistry in this region after repair by activated diffusion brazing.

6.3 Discussion

6.3.1 Microstructurally-Distinct Regions

Back-Scattered Electron images showed the presence or absence of interfacial particles and microstructural inhomogeneities in the repaired samples. The second and third brazing trials, to different degrees, exhibited three distinct regions within their cross-sections; the braze-repaired region, the diffusion-affected zone, and the base metal. In every brazing trial, the braze-repaired region was almost identical in appearance to the base metal, and most of the difference between regions was observed in the diffusion-affected zone found between the braze-repaired and base metal regions. The diffusion-affected zone contained a higher concentration of bright, heavy-element phases than the other regions, suggesting the diffusion of such phases out of the braze-repaired region.

6.3.2 Interfacial Particles

While the appearance of the braze-repaired region very closely resembled that of the base metal, interfacial particles were observed on two of the three brazing samples. The first sample exhibited small oxide particles in a few spots along the interface, whereas the third sample showed heavy-element phases along the entire prior surface of the substrate.

The presence of oxide particles in such a small quantity on the first brazing trial sample suggested that the material oxidized slightly between the cleaning and brazing processes. The oxides could have formed during the heating stage of the repair process. If the notch was sufficiently packed prior to heating, oxidation could not occur at the surface of the substrate, as the filler metal paste would have acted as a protective barrier. However, the packing of paste into the notch of the first brazing trial sample was incomplete, and insufficient vacuum levels, especially due to outgassing at high temperatures, could have resulted in slight oxidation at the substrate surface and the presence of small interfacial oxide particles on the final repaired specimen.

The interface on the third brazing trial sample was interesting in that the interfacial particles were found to be the heavy-element phases that were observed in all three regions of the repaired samples. The interface on the third brazing trial sample was discontinuous, but followed the entire prior surface of the substrate. Some areas, however, showed the movement of the interface toward the base metal. Perhaps, upon longer holding times, this diffusion would have resulted in an interface-free repair.

6.3.3 Porosity

The back-scattered electron images showed evidence of porosity, varying in size and quantity, on all repaired samples, although the amount of porosity decreased as the pre-placement was improved from the first to the third brazing trial. The presence of porosity suggested that at least one of the diffusion brazing process parameters including the mixing ratio or the pre-placement of the paste – and therefore to some extent the viscosity – require modification.

First of all, the mixing ratio required for a repair process is very dependent on the geometry of the damage, as each repair might require different filler metal characteristics such as flowability, density, and strength. Kim *et al.* [6] have shown that the optimal filler metal powder mixing ratio occurred at 60% base metal powder to 40% filler metal powder, as it gave the best compromise between density and intermetallic formation. A mixture too rich in base metal powder resulted in excessive porosity, since there was insufficient filler metal powder to flow within and continually re-fill the spaces between base metal powder particles [6]. On the other hand, too much filler metal powder resulted in the formation of excessive harmful intermetallic particles, due to the increased concentration of MPD particles and the reduced homogenization rate resulting from less base metal powder.

It has been shown in this chapter that the amount of binder combined to a filler metal powder mixture had a large effect on the resultant paste viscosity. The viscosity of the paste played an important role in the workability and pre-placement of the paste in the notch and therefore the amount of filling that could be achieved. A notch fully packed with paste resulted in a higher density of the brazed region, as it was shown that the density of each successive brazing trial was improved as better pre-placement was achieved. Because the density was improved more so by paste pre-placement than by the mixing ratio, paste pre-placement was decided to be the most important parameter studied. With adequate paste pre-placement, and ensuring that the molten filler metal remains inside the notch, a high-density repair can be achieved.

The complete pre-placement of the paste within the notch is critical in wide-gap diffusion brazing because the large amounts of base metal powder used do not flow toward the notch tip by capillary action, as was observed on the first and second brazing trials, which exhibited incomplete filling due to incomplete pre-placement. Larger amounts of the melting and flowing FMP can be used, but this results in lower strengths and longer diffusion times [6]. Therefore, to ensure adequate filling during the diffusion brazing process, complete paste pre-placement is critical.

6.3.4 Chemical Homogenization

Energy-Dispersive X-Ray spectrometry performed on cross-sections of the second and third brazing trial samples showed a consistent chemistry throughout each sample. Recall that the processes of oxidation and cleaning caused large inhomogeneities in the chemistry of GTD111, such as depletions of Al, Ti, and Ni, and an increased concentration of Cr, near the surface of components to be repaired by the diffusion brazing process. However, after repair by diffusion brazing, the chemistry of each sample was consistent between the base metal, diffusion-affected, and braze-repaired regions. Therefore, the diffusion brazing process successfully restored chemical homogeneity to the sample, regardless of the inhomogeneities induced by the oxidation and cleaning processes, and resulted in every region of the repaired sample analyzed having the same chemistry as the base metal [38], as was shown in table 6.1.

The depletions and concentrations of alloying elements resulting from the cleaning process seemed to have no effect on the chemistry of the braze-repaired samples, since the diffusion brazing process re-homogenized the chemistry. However, a homogenized chemistry does not necessarily indicate a sufficiently strong repair. Ojo *et al.* [5] found that the diffusion of Al and Ti into the base metal during the brazing process was crucial in restoring the original component's strength via the replenishment of the strengthening gamma prime phases. The optical microscopy results of Section 6.2.3.2 (see Figure 6.14) showed that this replenishment in fact took place during the diffusion-brazing repair of GTD111.

6.4 Summary

The results of the preliminary brazing trials have shown that successful brazing can be performed on GTD111, although the optimization of process parameters to allow for better or longer diffusion of interfacial particles might be necessary. The porosity was reduced dramatically through more effective pre-placement of paste in the notch, which was dependent on the paste viscosity. The ADB process was able to restore the chemistry of the braze-repaired notch and interfacial regions to that of the base metal. Also, the process returned the gamma prime strengthening phase to the previously-depleted interfacial regions.

Chapter 7 Conclusions and Future Work

7.1 Conclusions

The conclusions of this study can be grouped into three categories, including those that add to existing knowledge by presenting new findings, those which support the findings of past studies, and those present results different from past studies. Conclusions one, two, and five add new knowledge to the oxidation and subsequent cleaning of GTD111. Conclusion and four supports the findings of past studies, and conclusion three presents findings not previously observed in literature concerning the FIC process.

1 – GTD111 exhibited multilayer oxide growth with distinct regions characterized by one or two main alloying elements. The inner layers of aluminum oxide, Ni-W-Ta oxide, and Cr oxide formed regardless of the oxidation time, and some oxidation times showed one or two outermost layers consisting of weak Ni-Ti- and Cr-Ti-rich oxide regions which spalled from the surface during cooling from high temperature and/or grinding. EDX analysis and optical microscopy also showed the presence of a region depleted of the main alloying elements of Al and Ti, as well as of the strengthening gamma prime phase below and surrounding the Al-rich oxide regions. The current study provided a more detailed analysis of the oxide structure than has been shown by past studies, and also adds the observation of the region depleted of the gamma prime phase, which reached a maximum depth of 24μm into the substrate.

2 – The standard FIC process performed at Ti Coating, Inc. successfully removed the oxidation formed on GTD111 for up to 452 hours at 900°C, and EDX analysis showed that the resultant chemistry had no dependence on the chemical differences induced by varying oxidation times, although the gamma prime depletion was found to increase with time (until 308 hours) to a maximum depth of 31 μm from the surface.

3 – Strong depletions and concentrations of alloying elements were observed near the surface of GTD111 after the FIC process. Al and Ti depletions near the surface of cleaned samples to depths of 35.5 and 27.2 μm, respectively, agree with those observed in previous studies. However, in the current study, slight Ni depletion was observed to a depth of 34.7 μm, and Cr exhibited an increased concentration to 23.9 μm within the surface and a 10μm thick band of depletion within the bulk of the samples.

4 – Repaired samples exhibited interfacial particles and porosity within the braze-repaired region, although porosity was reduced dramatically with better pre-placement of the filler metal paste into the notches.

5 – The diffusion brazing process was able to restore chemical homogeneity to repaired samples, regardless of the oxidation time or resultant chemistry after the FIC process, as EDX analysis showed a consistent chemical composition throughout the braze-repaired, diffusion-affected, and base metal regions of the repaired samples. Also, optical microscopy showed that the diffusion brazing process restored the gamma-prime strengthening phase, which had previously been depleted by the processes of oxidation and cleaning, to the prior substrate surface. Therefore, it was found in the current study that neither the fluoride-ion cleaning process nor the diffusion brazing repair process need to be modified based on the duration of oxide formation

7.2 Future Work

The future work recommended by this study can be placed into two categories. The first four recommendations have been made to suggest actions that must be taken in order to further test the feasibility of the activated diffusion brazing repair process on GTD111. The fifth and final recommendation concerns a study of scientific interest, and is not required for the continuation of the current study.

1 – Mount oxidized samples in epoxy to keep external oxides intact

Mounting samples in epoxy prior to grinding will eliminate the chances or removing the weak external oxide regions from the sample during grinding. By performing SEM-EDX and element mapping analysis on mounted samples, the spallation of the weak outermost oxides can be verified. If the presence of the Ni-Ti-rich oxide scale is still intermittent, then the spallation of this phase can be attributed to the difference in CTE between the various oxide regions, in which case the weak external oxide will have spalled from the surface during cooling from the oxidation temperature.

2 – Process parameter optimization

It has been stated that the quality of a repair made by the activated diffusion brazing process is heavily dependent on many process parameters such as mixing ratio, paste viscosity and placement, and bonding temperature and time [6,27,30]. The current study has performed preliminary bonding trials, it is therefore recommended that brazing be performed on many samples, modifying only one process parameter at a time, in order to determine the effects, on a microstructural and chemical level, of each parameter on the quality of the diffusion brazing repair process.

3 – Mechanical testing on larger-scale samples

Again, since the scope of this study did not include large-scale applications of the diffusion brazing process, only small laboratory samples have been repaired. In the future, notches of similar geometry can be made in larger bars, from which tensile- and fatigue-testing samples can be machined. Since turbine blades operate in high-temperature environments under cyclic loading, it is recommended that high-temperature tensile, creep-rupture, and fatigue testing be conducted on repaired samples. If this testing is successful, the process can be scaled up once more to include repairs on actual service-run components.

4 – Create samples via sink-EDM to more closely represent repair on a full component

One problem encountered during the bonding trials was the need to prevent flow of the molten filler metal from the ends of the notch, due to the geometry of notch selected. Bond stops were put to use to prevent excessive flow, but it is important in the future to rely less on such bonding aids. Also, it is necessary to continually make samples that more closely represent the state of repairs to be made on service-run components. For example, many damages seen on real components will have closed ends, and so future samples should have notches created by the sink-EDM process, in which an electrode in the shape of the desired repair is pushed into the sample to create a notch. This method of notch creation will much more closely represent a crack in a service-run component.

5 – Analyze the kinetics of the FIC process

The current study determined the effect of time on the structure and chemistry of the complex oxide formed on GTD111, as well as on the ability of the FIC process to remove said oxidation. An interesting study that could be performed is to oxidize multiple samples for the same amount of time, and subject them to an interrupted cleaning process, where each sample is cleaned for a different period of time. Analysis of such samples could show the order of oxide removal and the advancement of the depleted regions into the substrate. However, since the FIC equipment is complex, each sample would require its own cleaning process, which must be aborted at a specific time, in order to clean each sample for a different duration.

References

[1] Ti-Coating Technical Report on Fluoride-Ion Cleaning, Internal report from Ti-Coating, Inc. [41]

[2] Liu, C.T., Ma, J., and Sun, X.F. (2010). **Oxidation behavior of a single-crystal Ni-base superalloy between 900 and 1000°C in air**. Journal of Alloys and Compounds, 491, 522-526

[3] Wu, Y. and Narita, T. (2009). **The cyclic oxidation behavior of the single crystal TMS-82+ superalloy in humidified air**. Materials and Corrosion, 60(10), 781-787

[4] Shawkat, A and Xiao, P. (2000). **Characterisation of oxide scales formed on nickel superalloy using impedence spectroscopy**. Materials at High Tempeatures, 17(1), 7-12

[5] Ojo, O.A., Richards, N.L., and Chaturvedi, M.C. (2004). **Effect of gap size and process parameters on diffusion brazing of Inconel 738**. Science and Technology of Welding and Joining, 9(3), 209-219

[6] Kim, Y.H., Kim, I.O., and Kim, C.S. (2005). **Effect of Process Variables on Microstructure and Mechanical Properties of Wide-Gap Brazed IN738 Superalloy**. Key Engineering Materials, Volumes 297-300, pp 2876-2882

[7] Heikinheimo, Liisa (2001). **Repair brazing of gas turbine hot parts – methods and joint characterization.** Technical Research Centre of Finland. Baltica V Conference, Porvoo, Finland, June 2001.

[8] Stankowski, A. et al (2002). **Advanced Thermochemical Cleaning Procedures for Structural Braze Repair Techniques**. Proceedings of ASME TURBO EXPO June 2002, Amsterdam, The Netherlands. ALSTOM (Switzerland Ltd).

[9] Zheng, L., Zhang, M., and Dong, J. (2010). **Oxidation behavior and mechanism of powder metallurgy Rene95 nickel based superalloy between 800 and 1000°C**. Applied Surface Science, 256, 7510-7515

[10] Sato, A., Chiu, Y.L., and Reed, R.C. (2011). **Oxidation of nickel-based single-crystal superalloys for industrial gas turbine applications**. Acta Materialia, 59, 225-240

[11] De Guadenzi, G.P., Colombo, A., Rocchini, G., and Uberti, F. (1996). **The Resistance of Some Gas Turbine Hot Component Coatings to High Temperature Corrosion and Thermal Cycling Damage**. Elevated Temperature Coatings: Science and Technology II, 301-311

[12] Young, W.R. (1978). **Turbine Airfoil Repair**. General Electric Company, Cincinnati, OH. Material Synergisms Conference, Kiamesha Lake, N.Y., U.S.A., October 1978.

[13] Jones, D. (1996). **Principles and Prevention of Corrosion (2nd Edition)**. Prentice Hall, Upper Saddle River, N.J.

[14] Lang, E. (1988). **The Role of Active Elements in the Oxidation Behavior of High-Temperature Metals and Alloys**. Elsevier Applied Science, London, England.

[15] Hassel, A.W. (2004). **Surface Treatment of NiTi for Medical Applications**. Min Invas Ther & Allied Technol,13(4), 240-247

[15] Hassel, A.W. (2004). **Surface Treatment of NiTi for Medical Applications**. Min Invas Ther & Allied Technol,13(4), 240-247

[16] Liu, L., Li, Y., and Wang, F. (2008). **The effect of micro-structure on the oxidation behavior of a Ni-based superalloy in water vapor plus oxygen**. Materials Letters, 62, 4081-4084

[17] Nychka, J.A., Clarke, D. R., and Meier, G.H. (2008). **Spallation and transient oxide growth on PWA 1484 superalloy**. Materials Science and Engineering A (490), 359-368

[18] Kofstad, P. and Lillerud, K.P. (1982). **Reoxidation of Chromium With Densified Cr_2O_3 Scales.** Oxidation of Metals, 17

[19] Trexler, M.D., Preet, M.S., and Sanders, T.H., Jr. (2008). **High Temperature Corrosion Behavior of DS GTD-111 in Oxidizing and Sulfidizing Environments**. Superalloys 2008, 699-708

[20] **Brazing Handbook**: fourth edition (1991). Miami, Florida: American Welding Society

[21] Miglietti, W. and Blum, F. (1998). **Advantages of Fluoride Ion Cleaning at Sub-Atmospheric Pressure**. Engineering Failure Analysis, 5(2), 149-169

[22] Keller, D.L., Resor, D.L. (1978). United States Patent 4,098,450 **"Superalloy Article Cleaning and Repair Method."** General Electric, Cincinnati, OH

[23] Schoonbaert, S. and Huang, X. (2007). **Brazing and Wide-Gap Repair of X-40 Using Ni-Base Alloys**. Proceedings of ASME TURBO EXPO, Montreal, Canada

[24] Chaturvedi, M.C., Ojo, O.A., and Richards, N.L. (2004). **Diffusion Brazing of cast Inconel 738 Superalloy**. Adv. In Tech. of Mat. And Mat. Proc. J. (ATM), 6(2), 206-213

[25] Malie, A.H.L., Grosbras, M., Beaufort, M.-F., Jacquot, F., and Huchin, J.-P. (2000). United States Patent 6,109,505 **"Method of Diffusion Brazing Superalloy Parts."** SNECMA Services, Paris, France

[26] Ch. Lecomte-Mertens (1989). **Metallurgical Study of Superalloy Brazing Alloys**

[27] Kim, Y.H., Kim, K.T., and Kim, I.H. (2006). **Effect of Mixing Ratio on mechanical Properties of Wide-gap Brazed Ni-Based Superalloy with Ni-Si-B Alloy Powder**. Key Engineering Materials, volumes 306-308, pp 935-940

[28] Personal communications with Mark Whitney, University of Waterloo, Ontario, Canada 2010

[29] Zhou, Y., Gale, W.F., North, T.H. (1995). **Modelling of transient liquid phase bonding**. International Materials Reviews, 40(5), 181-196

[30] Personal communications with Dientje Fortuna, Sulzer Metco (US) Inc., Troy, Michigan, U.S.A. 2009

[31] M.L. Kuntz, Y. Zhou, S. Corbin (2006). **A Study of Transient Liquid-Phase Bonding of Ag-Cu Using Differential Scanning Calorimetry**. Metallurgical and Materials Transactions, 37A, 2493-2504, 2006

[32] Fortuna, D. (2002). Sulzer Metco White Paper **"Wide-Gap Brazing: A Practical Approach to a Difficult Process."**

[33] He, L., Xu, Z., Li, J., Mu, R., He, S., and Huang, G. (2009). **Substrate Effects on the High-Temperature Oxidation Behavior of Thermal Barrier Coatings**. Journal of Materials Science and Technology, 25(6), 799-802

[34] Daleo, J.A. and Wilson, J.R. (1998). **GTD111 Alloy Material Study**. Journal of Engineering for Gas Turbines and Power, 120, 375-382

[35] **AMDRY wide-gap braze and filler powder material product data sheet** from Sulzer Metco

[36] Personal communications with Bill Potts, Vac Aero, Oakville, Ontario, Canada 2009

[37] Patnaik, P.C. (1985). **High Temperature Oxidation and Hot Corrosion of Nickel and Cobalt Based Superalloys**. National Research Council Publications Department, Ottawa, ON

[38] Sajjadi, S.A., Nategh, S., and Isac, M. (2003). **High Temperature Tensile Behaviour of the Ni-Base Superalloy GTD-111**. Canadian Metallurgical Quarterly, 42(4), 489-494

[40] Choi, W., Kim, S., Lee, C., and Jang, J. (2004). **Effect of Heating Rate on Transient Liquid Phase Diffusion Bonding of Ni-based Superalloy GTD-111**. Materials Science Forum, Volumes 449-452, pp 133-136

[41] Personal communications with Trish Drndarski, Ti-Coating, Inc., Utica, Michigan, U.S.A. 2010

[42] Alan Seim, Excel Wire EDM Inc., Kitchener, Ontario, Canada